Tropical Cyclone Climate Projections by 20-km Mesh MRI/JMA Atmospheric General Circulation Model

November 2010

Hiroyuki MURAKAMI

Tropical Cyclone Climate Projections by 20-km Mesh MRI/JMA Atmospheric General Circulation Model

A Dissertation Submitted to
the Graduate School of Life and Environmental Sciences,
the University of Tsukuba
in Partial Fulfillment of the Requirements
for the Degree of Doctor of Philosophy in Science

Hiroyuki MURAKAMI

Abstract

This study evaluates both medium-range predictions and climate projections regarding tropical cyclones (TCs) performed with the Meteorological Research Institute (MRI)/Japan Meteorological Agency (JMA) 20-km mesh super high-resolution Atmospheric General Circulation Model (MRI/JMA-AGCM). The 20-km mesh AGCM showed marked superiority compared with coarser resolution models, indicating (i) significant improvements in TC intensity, intensifying and decaying tendencies, and inner-core structure when verified with observations; and (ii) accurate realizations of climatological TC frequency of occurrence (TCF) and temporal interannual and seasonal variations in TC genesis number.

On the basis of these encouraging results, two suits of 25-year climate projections were conducted using the 20-km mesh AGCM for both the present-day (1979–2003) and future (2075–2099) climate under the IPCC SRES A1B emission scenario to investigate possible future changes in TC activities, especially TCF and TC tracks in the North Atlantic (NA) and western North Pacific (WNP) ocean basins.

The future projection indicates statistically significant reduction in global TC genesis number and increase in frequency of intense TCs; however, projected future changes in TCF showed somewhat inhomogeneous within a specific ocean basin. In the NA, TCF will decrease in the tropical western NA (WNA) and increase in the tropical eastern NA (ENA) and northwestern NA (NWNA), suggesting a reduced probability of TC landfall over the southeastern United States, and an increased influence of TCs on the northeastern United States. The track changes are not due to changes in large-scale steering flows; instead, they are due to changes in TC genesis locations. The increase in TC genesis in the ENA arises from increasing background ascending motion and convective available potential energy. In contrast, the reduced TC genesis in the WNA is attributed to decreases in midtropospheric relative humidity and ascending motion caused by remotely forced anomalous descent. This finding indicates that the impact of remote dynamical forcing is

greater than that of local thermodynamical forcing in the WNA. The increased frequency of TC occurrence in the NWNA is attributed to reduced vertical wind shear and the pronounced local warming of the ocean surface.

In the WNP, the future projection indicates (i) a significant reduction (by about 23%) in both TC genesis number and frequency of occurrence, which occurs primarily during the late part of the year (September–December); (ii) an eastward shift in the positions of the two prevailing northward recurving TC tracks during the peak TC season (July–October); and (iii) a significant reduction (by 44%) in TC frequency approaching coastal regions of Vietnam. The changes in occurrence frequency are due in part to changes in large-scale steering flows which hinder westward TC motion at lower latitudes, but due mainly to changes in the location of TC genesis: fewer TCs will form in the western portion of the WNP (west of 145 °E), whereas more storms will form in the southeastern quadrant of the WNP (10–20 °N, 145–160 °E). Analysis of the Genesis Potential Index reveals that the reduced TC genesis in the western WNP is due mainly to *in situ* weakening of large scale ascent and decreasing mid-tropospheric relative humidity, which are associated with the enhanced descent of the tropical overturning circulation, especially the Walker circulation. The analysis also indicates that enhanced TC genesis in the southeastern WNP is due to increased low-level cyclonic vorticity and reduced vertical wind shear. These favorable dynamical conditions are associated with the reinforced northward cross-equatorial flows in the western Pacific that are induced by differential warming rates in the two hemispheres (the Northern Hemisphere warms faster than the Southern Hemisphere). These changes appear to be critically dependent on the spatial pattern of future sea-surface temperature.

Key Words: tropical cyclone, global warming, climate projection, weather prediction, high resolution atmospheric general circulation model, track change

Contents

Abstract **i**

List of tables **vi**

List of figures **viii**

List of Acronyms **xii**

1 Introduction **1**

1.1 Overview of numerical studies on tropical cyclone climate changes 1

1.2 Review of studies on tropical cyclone track changes 3

1.3 Purpose and motivation of this study 6

2 Verification of typhoon predictions **9**

2.1 Model Descriptions 9

2.2 Initial condition 14

2.3 Simulated typhoons 16

2.4 Best-track data 17

2.5 Method to detect the position of a typhoon 18

2.6 Results and discussions 19

2.6.1 Position errors 19

2.6.2 Intensity verification 24

2.6.3 Typhoon structure 27

2.7 Summary 29

3 Effect of model resolution on tropical cyclone climate projections **57**

3.1 Methodology 57

3.1.1 Model descriptions 57

3.1.2 Observations 59

3.1.3 Prescribed external boundary forcings 60
3.1.4 TC detection method and definition of TGF 61
3.2 Results and discussion 63
3.2.1 Effect of model resolution on projected TC intensity 63
3.2.2 Effect of resolution on projected TC genesis number 64
3.2.3 Effect of resolution on the projected spatial distributions of TC genesis frequency 65
3.3 Summary 66

4 Projected future change in North Atlantic tropical cyclone tracks 79
4.1 Analysis methods for projected output 79
4.1.1 Detection method for tropical cyclones 79
4.1.2 Genesis Potential Index (GPI) 81
4.2 Evaluation of the present-day simulation 84
4.2.1 TC tracks and frequency of occurrence 84
4.2.2 Inter-annual and seasonal variability in TC genesis 84
4.2.3 Change in TC activity induced by ENSO 85
4.3 Projected future change in TC tracks, frequency, and inter-annual variation 87
4.4 Reasons for future change 88
4.4.1 Reason for future change in TC tracks 88
4.4.2 Reasons for future change in genesis locations 89
4.5 Summary 93

5 Projected future change in western North Pacific tropical cyclone tracks 111
5.1 Detection method for tropical cyclones 112
5.2 Statistical significance tests 113
5.3 Evaluation of the present-day simulation 114
5.3.1 TC tracks and frequency of occurrence 114
5.3.2 Interannual and seasonal variability in TC genesis 114

5.3.3 Variations in TC genesis influenced by ENSO 115
5.4 Projected future changes 116
5.4.1 Tropical cyclone genesis number 116
5.4.2 Frequency and tracks 117
5.4.3 TCs approaching land 117
5.5 Reasons for future change in TC frequency 119
5.5.1 Changes in large-scale flows and TC genesis frequency 119
5.5.2 TCF changes projected by a trajectory model 120
5.6 Mechanisms of the future changes in TC genesis 121
5.7 Summary 125

6 Conclusions **142**

Acknowledgements **146**

References **148**

List of Tables

2.1 Specifications of the models used in this study. 32

2.2 List of the recent major revisions in the physical processes for the 20-km mesh AGCM. 33

2.3 List of all simulated typhoons. 33

3.1 Main features of the model considered for analyses for resolution difference 68

3.2 CMIP3 models used for future prescribed lower boundary conditions 69

3.3 Model biases in annual mean TC genesis number for each basin 70

3.4 Correlation coefficients for the inter-annual TC genesis number for each basin compared with observations 70

3.5 Correlation coefficients for the seasonal TC genesis number for each basin compared with observations 70

3.6 Future changes in annual TC genesis number for each basin 70

3.7 Inter-resolution correlation coefficients for biases of tropical cyclone genesis frequency 71

3.8 Inter-resolution correlation coefficients for future change of tropical cyclone genesis frequency 71

5.1 Accumulated tropical cyclone storm days in nine coastal regions during the July-October season 128

5.2 Averaged instantaneous maximum wind velocity in nine regions during the July–October season 128

5.3 Mean TC numbers in nine regions when TCs exist over land-surface grids . 129

List of Figures

2.1 Scalability performance of the 20-km mesh AGCM on the Earth Simulator. 34

2.2 Typhoon bogus inserted into GANAL. 35

2.3 Configuration of the typhoon experiment. 36

2.4 Best-track data provided by the RSMC-Tokyo Typhoon Center 37

2.5 Land effect on detecting radii 50 and 30 knots 38

2.6 Simulated typhoon tracks 39

2.7 Composite large-scale field for the T0207 which is averaged before the typhoon recurves 41

2.8 Composite large-scale field for the T0421 which is averaged before the typhoon recurves 42

2.9 Simulated position error 43

2.10 An example of position error in the DR stage of T0514 case. 44

2.11 Simulated central typhoon position along/across the moving direction relative to the storm position of analysis 45

2.12 Simulated central typhoon position along/across the moving direction relative to the storm position of analysis for TCs in AR stage for each forecast hour 46

2.13 Composite large-scale field for typhoons after the typhoon recurves. 47

2.14 Systematic bias of the mean position and sea level pressure 48

2.15 Simulated typhoon central pressure by each model 49

2.16 Simulated maximum sustained wind by each model 50

2.17 Tendency of the central pressure 51

2.18 Tendency of the maximum wind velocity 52

2.19 Comparison of infrared images 53

2.20 Mean errors of radii of 30 knot and 50 knot 54

2.21 Mean wind profile for each forecast time 55

2.22 Mean wind profile of storms whose wind velocity is more than 50knot after 60 forecast hours 56

3.1 Schematic diagram of prescribed lower boundary conditions for the future simulation. 68

3.2 Prescribed SSTs and the future change 72

3.3 Accumulated number of detected tropical cyclones using different values of criterion ζ_{850} 73

3.4 Tropical cyclone genesis frequency (TGF) by best-track data and JRA-25 . 74

3.5 Projected relationship between maximum wind velocity and sea level pressure 75

3.6 Probability density of life-cycle maximum surface wind speed and its future change 76

3.7 Azimuthal mean profiles of projected precipitation and maximum surface wind 77

3.8 Biases and future changes in tropical cyclone genesis frequency 78

4.1 Modified Genesis Potential Index 96

4.2 Total tropical cyclone tracks and frequency of occurrence projected by present-day simulation in the NA 97

4.3 Projected interannual and seasonal variations in tropical cyclone genesis number in NA 98

4.4 Locations of projected TC genesis and GPI anomalies for each phase of ENSO in NA 99

4.5 Projected future changes in total tropical cyclone tracks and frequency of occurrence in NA 100

4.6 Simulated large-scale steering flows in North Atlantic 101

4.7 Simulated mean tropical cyclone translation vectors in North Atlantic . . . 102

4.8 Simulated frequency of tropical cyclone genesis and genesis potential index 103

4.9 Future change in the Genesis Potential Index and contribution of each elements to the future change in NA 104

4.10 Area mean of future change in the Genesis Potential Index and contribution of each elements to the future change in NA 105

4.11 Projected future change in 850–200 hPa vertical wind shear 106

4.12 Projected future changes in vertical velocity at 500 hPa and relative humidity at 600 hPa 107

4.13 Projected future changes in precipitation 108

4.14 Future change in seasonal mean of prescribed SST 109

4.15 Seasonal mean of SST fractional change predicted by each CMIP3 model . 110

5.1 Total tropical cyclone tracks and frequency of occurrence projected by present-day simulation in the WNP 130

5.2 Projected interannual and seasonal variations in tropical cyclone genesis number in WNP 131

5.3 Mean differences in TC genesis frequency and GPI between El Niño and La Niña years 132

5.4 Projected future changes in total tropical cyclone tracks and frequency of occurrence in WNP 133

5.5 Observed TCs in the nine coastal regions during July–October 134

5.6 Projected mean TC translation vectors 135

5.7 Simulated future changes in mass-weighted flows in WNP 136

5.8 Projected future changes in the averaged tropical cyclone genesis frequency and GPI 137

5.9 Future changes in total tropical cyclone tracks and frequency of occurrence in WNP projected by a trajectory model 138

5.10 Future change in the Genesis Potential Index and contribution of each elements to the future change in WNP 139

5.11 Future changes in omega at 500 hPa and streamline at the 850 hPa 140

5.12 Future change in seasonal mean prescribed SST and projected precipitation 141

List of Acronyms

3DVAR	Three-Dimensional VARiational data assimilation	59
AESTO	Advanced Earth Science and Technology Organization	6
AGCM	Atmospheric General Circulation Model	6
AR	After Recurvature	21
AR4	Fourth Assessment Report	2
BR	Before Recurvature	21
CCSM2	NCAR Community Climate System Model version 2	5
CMIP3	World Climate Research Programme's Coupled Model Inter-comparison Project phase 3	5
DR	During Recurvature	21
ENP	Eastern North Pacific	63
ENSO	El Niño-Southern Oscillation	4
ES	Earth Simulator	6
GANAL	JMA Global Analyses	14
GCM	Global Circulation Model	2
GFDL	Geophysical Fluid Dynamics Laboratory	4
GL	Global	63
GPI	Genesis Potential Index	81
GSM	Global Spectral Model	9
GW	Global Warming (projection)	87
IPCC	Intergovernmental Panel on Climate Change	2
ITCZ	Inter-Tropical Convergence Zone	61
JASO	July, August, September, and October	86
JMA	Japan Meteorological Agency	6
JRA-25	Japanese 25-year Re-Analysis	59

JTWC	Joint Typhoon Warning Center	59
MJO	Madden-Julian Oscillation	3
MPI	Maximum Potential Intensity	82
MRI	Meteorological Research Institute	6
MSLP	Mean Sea Level Pressure	18
NA	North Atlantic	1
NCAR	National Center for Atmospheric Research	5
NH	Northern Hemisphere	63
NHC	National Hurricane Center	59
NIO	North Indian Ocean	63
PCMDI	Program for Climate Model Diagnosis and Inter-comparison	5
PD	Present-day (projection)	84
PDO	Pacific Decadal Oscillation	3
QBO	Quasi-Biennial Oscillation	3
QuikSCAT	Quick Scatterometer	20
R30	Radius of 30-knot	18
R50	Radius of 50-knot	18
RCM	Regional Climate Model	2
RSMC-Tokyo	Regional Specialized Meteorological Center of Tokyo	17
SH	Southern Hemisphere	63
SIC	Sea Ice Concentration	60
SIO	South Indian Ocean	63
SPO	South Pacific Ocean	63
SRES	Special Report on Emission Scenarios	4
SST	Sea Surface Temperature	2
STS	Severe Tropical Storm	17

TC	Tropical Cyclone	1
TCR	Tropical Cyclone Retrieved	59
TFLOPS	Tera FLoating point number Operations Per Second	6
TGF	Tropical Cyclone Genesis Frequency	62
TS	Tropical Storm	17
TY	Typhoon	17
UTC	Universal Time Coordinated	16
WNP	Western North Pacific	2

Chapter 1

Introduction

1.1 Overview of numerical studies on tropical cyclone climate changes

Tropical cyclones (TCs) are among the most harmful weather phenomena: The most costly natural disaster to affect the United States of America over the period 1960–2005 was caused by TCs (Peterson et al., 2008). In recent years, Hurricane Katrina (2005) was the most damaging storm (Schmidlin, 2006), Hurricane Wilma (2005) was the most intense storm (central pressure of 882 hPa) on record in the North Atlantic (NA), and Hurricane Rita (2005) was the most intense (central pressure of 895 hPa) tropical cyclone ever observed in the Gulf of Mexico. Hurricane activity in the NA showed an increase over the past 30 years (Goldenberg et al., 2001; Webster et al., 2005; Bell and Chelliah, 2006). In Japan, 10 typhoons caused disastrous damage in 2004 (Levinson, 2005). The increased severity of TCs has aroused public interest regarding the impact of global warming on TC activity. Previous studies have proposed that these recent changes are largely due to global warming (Emanuel, 2005; Anthes et al., 2006; Hoyos et al., 2006; Mann and Emanuel, 2006; Trenberth and Shea, 2006; Holland and Webster, 2007; Mann et al., 2007a; Mann et al., 2007b). However, this view has been challenged by the following points: 1) recent increases in the frequency of Atlantic TCs are within the range of observed multi-decadal variability (e.g., Goldenberg et al., 2001; Pielke et al., 2005; Bell and Chelliah, 2006) and 2) the observational data used to attribute the trend to global warming are insufficient (Landsea et al., 2006; Landsea, 2007).

Many studies have sought to project the future climate associated with warmer sea

surface temperature (SST) using increased-CO_2 scenarios and general circulation models (GCMs) (Broccoli and Manabe, 1990; Haarsma et al., 1993; Bengtsson et al., 1996; Krishnamurti et al., 1998; Royer et al., 1998; Sugi et al., 2002; Tsutsui, 2002; McDonald et al., 2005; Chauvin et al., 2006; Oouchi et al., 2006; Yoshimura et al., 2006; Bengtsson et al., 2007; Gualdi et al., 2008; Zhao et al., 2009), and regional climate models (RCMs) (Knutson et al., 1998; Knutson and Tuleya, 1999; Nguyen and Walsh, 2001; Knutson and Tuleya, 2004; Walsh et al., 2004; Stowasser et al., 2007; Knutson et al., 2008; Bender et al., 2010). Most of these studies projected a future increase of TC intensity. Most models have also projected a reduced frequency of TCs globally, with a wide range of predictions among models. Consequently, the Intergovernmental Panel on Climate Change (IPCC) Fourth Assessment Report (AR4)(IPCC, 2007) concluded in its summary chapter for policymakers that there is "less confidence" in projections of a global decrease in the frequency of TCs than in projections of increased maximum intensities. The inconsistency in the TC frequency changes becomes more pronounced when specific tropical ocean basin is considered. For example, among 14 (12) previous numerical studies of future TCs over NA (western North Pacific (WNP)), 5 (5) explicitly indicated an increasing frequency, whereas 9 (7) reported a decreasing frequency. Although many studies using the state-of-the-art model appear to agree with reduction in global TC number and increase in frequency of intense TCs in the future, consensus is yet to be reached regarding future changes in TC frequency in a specific ocean basin. This is mainly due to different experimental designs (e.g., different warming rates, Gualdi et al., 2008; Zhao et al., 2009), different model resolutions and physics (e.g., Bengtsson et al., 2007), model biases (e.g., Murakami and Sugi, 2010), and different TC detection criteria (Walsh et al., 2007). General horizontal scale of TC is ranging from 100 km to 1,000 km in nature; therefore, high resolution model is necessary in order to address future change in TC climatology.

Although fine-resolution RCMs may lead to realistic TC structures and reliable future projections in terms of TC intensity, they seem to be limited to discuss future changes

in TC genesis and TC tracks because the RCMs are subject to the lateral boundary conditions and the modeled domain. The mechanisms of TC genesis are not closed in an ocean basin as will be discussed in Section 1.2. Because the domain of TC tracks ranges from tropics to mid-latitudes, it is preferable to cover wide range of domain, which requires large computational resouces for RCMs. For the above reasons, high-resolution global models is better to be used for investigating future changes in TC genesis and TC tracks than RCMs. However, since high-resolution global model runs also remain very expensive, most climate simulations have been done with coarser resolution (100–200-km mesh; Knutson et al., 2010); thus, projecting future changes in TC activities is still a challenging task. In contrast, a reliable future projection is highly demanded in order to estimate and reduce future damages caused by climatological TC changes induced by anthropogenic global warming.

1.2 Review of studies on tropical cyclone track changes

Although many modeling studies have explored future change in TC intensity or genesis frequency (see Section 1.1), few have considered present-day variation and future change in TC tracks. Based on observational studies, the TC activity in the WNP shows prominent natural variations at various time scales. For example, the Madden-Julian Oscillation (MJO; Madden and Julian, 1972, 1994) has a strong influence on TC genesis and occurrence at intraseasonal time scales (Camargo et al., 2009). TC activity also shows interannual to interdecadal variations (Chan, 1985; Chan, 2000; Yumoto and Matsuura, 2001; Ho et al., 2004; Wu and Wang, 2004), which are strongly affected by various factors associated with low-frequency anomalous climate patterns, such as El Niño-Southern Oscillation (ENSO) (Lander, 1994; Chen et al., 1998; Wang and Chan, 2002; Wu et al., 2004; Camargo and Sobel, 2005), the stratospheric quasi-biennial oscillation (QBO; Chan, 1995; Ho et al., 2009), and the Pacific Decadal Oscillation (PDO) (Wang et al., 2010).

Ho et al. (2004) first reported that the frequency of TC occurrence showed a significant decrease in the Philippine Sea in the periods 1980–2001 compared with 1951–1979. Wu et al. (2005) compared TC frequency between 1965–1983 and 1984–2003 using observed best-track data, revealing that the two prevailing TC tracks in the WNP had shifted significantly westward; hence, the frequency of TC occurrence has increased over subtropical East Asia and strongly decreased over the South China Sea. Changes in TC tracks during the past decade have been attributed to westward extension of the subtropical high (Zhou et al., 2009). Note that the observed TC-track data are insufficient to evaluate the long-term trend because of the low quality of these data collected before the satellite era (Landsea et al., 2006).

Also, in the NA, TC activities are largely subject to variations within interannual, e.g., ENSO (Gray, 1984; Camargo et al., 2007a) and QBO (Gray, 1984; Elsner et al., 1999) and interdecadal time scales (Landsea et al., 1992; Landsea et al., 1999). Vecchi and Knutson (2008) reconstructed an observational TC dataset since the late 1800s, and showed a decrease in TC activity in the western part of the NA, and an increase in the eastern part over the past 100 years.

On the other hand, few modeling studies have discussed future changes in TC tracks. Given the deficiencies of low-resolution global models in faithfully resolving TCs, Wu and Wang (2004) attempted an indirect method for assessing the possible influence of global climate change on TC tacks. The authors demonstrated that the main characteristics of the current climatology of TC tracks can be derived using a trajectory model and the mean TC motion velocity field, which comprises a large-scale steering flow and beta drift (Wang et al., 1998). Based on this trajectory model and the changes in large-scale steering flows projected by Geophysical Fluid Dynamics Laboratory (GFDL) global warming experiments (Special Report on Emission Scenarios (SRES) A2 and B2 scenarios), the authors predicted that more TCs will take northward recurving tracks during the period

2030–2059. However, their trajectory model did not take into account future changes in TC genesis locations and possible changes in the magnitude of beta drift.

Previous modeling studies that directly evaluated future changes in WNP TC tracks have yielded diverse results. For example, Bengtsson et al. (2007) used the ECHAM5 global climate models with T213 (about 60-km grid size) and T63 (about 200-km grid size) resolutions forced by the projected future SST of the SRES A1B scenario and reported that TC track density will decrease in the overall region of the WNP except for the eastern WNP. In contrast, using a regional model (horizontal resolution of 0.5°) driven by lateral boundary conditions produced by outputs of the National Center for Atmospheric Research (NCAR) Community Climate System Model version 2 (CCSM2) under an extremely strong ($6 \times CO_2$) forcing, Stowasser et al. (2007) projected that warming leads to significantly more TCs in the South China Sea, but little change in TC occurrence in other areas compared with the present-day experiment. Yokoi and Takayabu (2009) investigated future changes in TC genesis frequency (TGF, see Section 3.1.4 for the definition) over the WNP using five CMIP3 (World Climate Research Programme's Coupled Model Inter-comparison Project phase 3) models with medium resolution (T63–T106). Similar to the results obtained by McDonald et al. (2005), the authors reported that the prevailing genesis region in the WNP shows significant southeastward shift, similar to the observed during El Niño years. However, the CMIP3 output by the Program for Climate Model Diagnosis and Inter-comparison (PCMDI) database (http://www-pcmdi.llnl.gov/) has only daily averages, making it difficult to detect TC tracks, especially in mid-latitude regions, which are characterized by rapid TC movement.

As to numerical studies regarding future TC tracks changes in the NA, Bengtsson et al. (2007) showed TCF change using the T63 and T213 atmospheric global models. Although the spatial pattern of future change in TCF is similar globally between two resolutions, the pattern shows inconsistency in the NA as well as eastern Pacific. The

authors attributed this inconsistency to inadequate TC genesis in the T63 model. Chauvin et al. (2006) also used higher resolution of 0.5° stretched global model in order to see change in TC activity over the NA. The authors showed north-eastward shift of TC activity in the future experiments. However, it is unknown what factor affected TC activity changes, though the authors just showed similar change of detected TC activity changes and Genesis Potential Index (GPI, explained later in Section 4.1.2).

Above all, reliability of the future change in TC tracks is now open to question because of low resolution models, inconsistent results by model resolution, biases of TC genesis and track, and sensitivity in prescribed SST anomaly spatial pattern. It is important to investigate whether anthropogenic warming influences TC density over the NA and WNP, since future changes in TC landfall frequency directly affects human life and socioeconomy.

1.3 Purpose and motivation of this study

Although the current generation of models lacks the horizontal resolution necessary to resolve realistic TCs, recent advances in computational resources, such as the Earth Simulator (ES), which is a parallel-vector supercomputer consisting of 5,120 processors [1](Habata et al., 2004) and had been recognized as the fastest computer in the world for the period 2002 to 2004, enable us to project future climate with a high-resolution Atmospheric General Circulation Model (AGCM). Using the ES, the Advanced Earth Science and Technology Organization (AESTO), the Meteorological Research Institute (MRI), and the Numerical Prediction Division of the Japan Meteorological Agency (JMA) have developed a super high-resolution (TL959L60; triangular truncation 959 with the linear Gaussian grid which is equivalent to 20-km mesh horizontally and 60 layers vertically)

[1]After the first replacement at March 2009, the number of processors decreased to 1,280 from 5,120, while peak performance increased to 131 Tera FLoating point number Operations Per Second (TFLOPS) from 40 TFLOPS.

AGCM (Mizuta et al., 2006; hereafter referred to as MRI/JMA-AGCM) to investigate the effect of global warming on TCs (Oouchi et al., 2006), Baiu (Kusunoki et al., 2006), and extreme indices (Kamiguchi et al., 2006; Uchiyama et al., 2006) in order to contribute to IPCC AR4.

In particular, Oouchi et al. (2006) showed that the number of tropical cyclones is globally reduced and the number of strong tropical cyclones is increased in the warm-climate environment more than in the present-day climate. The authors carefully evaluated the reliability of their projection by comparing their present-day 10-year experiment with observations with respect to geographical distribution, frequency, and intensity. Although the authors insist that their 20-km mesh AGCM is more excellent than other coarse model in the intensity projections, there is no remark of evaluations that compare with other resolutions and observations.

Even in the medium-range forecast, there is no research that statistically shows the superiority of such a high-resolution global model from the viewpoint of the TC prediction. Some studies have shown that the tropical storm structure was well simulated with high-resolution AGCMs. For example, Ohfuchi et al. (2004) simulated tropical cyclones as an initial value problem with a 10-km mesh AGCM, which was the highest-resolution AGCM in the world when this study was launched. However, because their simulations were not validated, it is uncertain whether or not their simulated tropical storms were realistic. Shen et al. (2006) also simulated Hurricane Katrina with a 0.125° grid mesoscale-resolving finite-volume AGCM. Although the authors showed that a high-resolution model provides better intensity forecasts than low-resolution one, only one initial case was shown, and other initial cases are unknown. Another issue that has yet to be clearly addressed is the effect of model resolution on the climatological features of projected TCs. This lack of information reflects the fact that high-resolution global model projections remain extremely expensive; consequently, most climate runs are performed with a relatively coarse

resolution (e.g., 100–200-km mesh). Therefore, it is important to evaluate predictions and climate projections of TCs to determine superiority using such a high-resolution AGCM.

The present study investigates resolution-related differences at first. Particularly, this study addresses a question "What is improved using a high-resolution model such as 20-km mesh AGCM compared with other coarser resolution models in terms of TC prediction and climate projections?" After the evaluation, this study investigates future changes in TC tracks over NA and WNP projected by the 20-km mesh high-resolution AGCM. The projections performed in this study are expected to be more reliable than those reported by Oouchi et al. (2006) because this study employs more realistic features in the experimental design (see Section 3.1.3 for details).

The remainder of the dissertation is organized as follows. Chapter 2 presents verifications of the performance of the 20-km mesh AGCM in simulating real targeted typhoons with real initial conditions and compared the results with those obtained using a coarser-resolution version of the model. Chapter 3 provides effect of model resolution on TC climate projections using four resolutions, addressing some speriorities in TC climatology with the 20-km mesh AGCM. Chapter 4 and 5 give future changes in TC tracks over the NA and WNP, respectively. Chapter 6 summarizes the main conclusions.

Chapter 2

Verification of typhoon predictions

This chapter aims to statistically evaluate the predictability of tropical cyclone by the 20-km mesh AGCM in terms of tracks, intensity, intensifying and decaying tendencies, and inner-core structure of wind profile through medium-range forecasts. Twelve real TCs over the WNP, namely, typhoons, were simulated with the 20-km mesh AGCM. They were compared with the simulations produced by the 60-km mesh JMA former operational global spectral model (hereafter referred to as "GSM"). Following sections describe the forecast models (Section 2.1), initial conditions (Section 2.2), simulated typhoons (Section 2.3), best-track data (Section 2.4), method used to detect the typhoon position (Section 2.5), and main results (Section 2.6). A summary and concluding remarks follow in Section 2.7. Detailed contents are also available in Murakami et al. (2008).

2.1 Model Descriptions

The 20-km mesh AGCM has been developed by the JMA and the MRI for both weather forecasting (JMA, 2007; Murakami and Matsumura, 2007) and climate research (Mizuta et al., 2006; Kusunoki et al., 2006; Oouchi et al., 2006). Table 2.1 summarizes specifications of all models used in this study. Although the forecast models (Table 2.1a, as used in this Chapter) are different from the climate models (Table 2.1b, as used in Chapters 3, 4, and 5) in the radiation and land-surface processes, they share most dynamical and physical schemes.

The resolution of the 20-km mesh AGCM is TL959L60[1], namely, horizontal 20-km mesh and 60 vertical layers. The model employs a sigma-pressure hybrid coordinate as the vertical coordinate (Simmons and Burridge, 1981). The model top is placed at approximately 0.1 hPa pressure level, whereas the lowest level is placed at 998.5 hPa pressure level when the surface pressure is 1000 hPa. There are 13 vertical layers below the 800 hPa pressure level and 29 layers over the 200 hPa pressure level.

The 20-km mesh AGCM adopts a semi-Lagrangian scheme (Yoshimura and Matsumura, 2003) which enables integration with a longer time step without being constrained by the Courant-Fredrichs-Lewy (CFL) condition. In the semi-Lagrangian advection scheme, computation of the advection terms is split into the horizontal and vertical directions and the both terms are computed separately. The flux in the vertical direction is evaluated with a one-dimensional conservative semi-Lagrangian scheme, while the horizontal advection is calculated with a conventional non-conservative 2-dimensional semi-Lagrangian scheme.

As a cumulus convection scheme, which is important for typhoon formation, a prognostic Arakawa-Shubert scheme (Arakawa and Schubert, 1974; Randall and Pan, 1993) is implemented. For an economical computation, two simplifications are introduced. First, the vertical profile of the upward mass flux η is assumed to be a linear function of height z, as proposed by Moorthi and Suarez (1992), in the following way; $\eta = 1 + \lambda(z - z_b)$, where λ denotes the entrainment rate and z_b is the cloud base height. Secondly, the mass flux at the cloud base is determined by solving a prognostic equation (Randall and Pan, 1993) rather than by applying the quasi-equilibrium assumption. The cloud base level is fixed near 900 hPa in the model. The moist static energy and other thermodynamic properties of the upward mass flux at the cloud base are given by the grid-scale values at the maximum moist static energy level below the cloud base.

[1]Here TL refers to the linear conversion scheme between Gauss and spherical harmonics, T to the quadratic one.

Clouds are also prognostically determined in a similar fashion to that of Smith (1990), in which the cloud amount and the cloud water content are estimated by a simple statistical approach proposed by Sommeria and Deardorff (1977). In each grid box, the total moisture (water vapor and cloud water) and the liquid water temperature are assumed to vary within the grid box due to unresolved atmospheric fluctuations with a uniform probability distribution.

In the radiation process, the radiative heating rate is computed as the convergence of the net radiation fluxes F;

$$\left(\frac{\partial T}{\partial t}\right)_{rad} = \frac{g}{C_p}\frac{\partial F}{\partial p}, \tag{2.1}$$

where g is the acceleration of gravity. The solution of the radiative transfer equation is computationally very expensive. In order to cut down on the computational costs, the full radiation computations for long wave and short wave are only done every three hours and hourly, respectively. In the GSM, the basic framework of the long-wave fluxes and cooling rates computations follows Sugi et al. (1990). In the forecast model in the 20-km mesh AGCM, a more accurate scheme is installed: Long-wave spectrum is divided into 9 bands and the radiation flux is calculated in each band separately. Considering a tradeoff between accuracy and efficiency, gaseous transmittance is computed using three different approaches, depending on the absorber and the spectral band. In order to take into account the Doppler absorption effect accurately, a table look-up method is used for spectral band contributing cooling in the stratosphere. Short-wave scattering and absorption are modeled by a two-stream formulation using the delta-Eddington approximation (Joseph et al., 1976; Coakley et al., 1983). The spectrum is divided into 22 bands based on Freidenreich and Ramaswamy (1999), except that water vapor in a near-infrared region is based on Briegleb (1992). On the other hand, the climate models use a different radiation scheme from the forecast models. The climate models adopt a multi-parameter random model for terrestrial radiation (Shibata and Aoki, 1989); a delta-two-stream approximation scheme for solar radiation (Shibata and Uchiyama, 1992).

The surface turbulent fluxes are formulated as the bulk formulae following the Monin-Obukhov similarity theory. The level 2 turbulence closure scheme of Mellor and Yamada (1974) is used to represent the vertical diffusion of the momentum, heat, and moisture. Based on the local-K theory, the turbulent transports are expressed as

$$\overline{w'\mathbf{v}'} = -K_m \frac{\partial \mathbf{v}}{\partial z}, \tag{2.2}$$

$$\overline{w's'_L} = -K_h \frac{\partial s_L}{\partial z}, \tag{2.3}$$

$$\overline{w'q'_w} = -K_h \frac{\partial q_w}{\partial z}, \tag{2.4}$$

where $s_L(\equiv C_pT + gz - Lq_c)$ is the liquid water static energy and $q_w(\equiv q + q_c)$ the total water content. Following the mixing-length theory, the diffusion coefficients can be written as

$$K_m = l^2 \left| \frac{\partial \mathbf{v}}{\partial z} \right| f_m(R_i), \tag{2.5}$$

$$K_h = l^2 \left| \frac{\partial \mathbf{v}}{\partial z} \right| f_h(R_i), \tag{2.6}$$

where the mixing length l is given according to Blackadar (1962),

$$l = \frac{kz}{1 + kz/l_0}. \tag{2.7}$$

The asymptotic mixing length l_0 is determined from the sub-grid scale orographic variances and the planetary boundary layer depth. The gradient Richardson number R_i is defined after the method of Smith (1990),

$$R_i = g\left\{ \tilde{\beta}_s \frac{\partial s_L}{\partial z} + \tilde{\beta}_Q \frac{\partial q_w}{\partial z} \right\} \Big/ \left| \frac{\partial \mathbf{v}}{\partial z} \right|^2, \tag{2.8}$$

where $\tilde{\beta}_s$ and $\tilde{\beta}_Q$ are the buoyancy parameters in terms of the cloud-conserved quantities s_L and q_w, respectively. The stability functions f_m and f_h are given by Mellor and Yamada (1982).

The parameterization for the orographic gravity wave drag consists of two components; one for long waves (wavelength > 100 km) and the other for short waves (wavelength ≈

10 km). The long waves are assumed to propagate upward until reaching wave-breaking levels mainly in the stratosphere and exert drag there (type A scheme), while short waves are always regarded as trapped and dissipated within the troposphere (type B scheme). Therefore the fundamental difference between the two schemes appears in the vertical distribution of the momentum deposit. The type A scheme is based on Palmer et al. (1986) with some modifications. Details are explained in Iwasaki et al. (1989).

A Simple Biosphere scheme (SiB) for a land surface model (Sellers et al., 1986; Sato et al., 1989) is also implemented. The SiB model estimates temporal changes in various land-surface properties such as vegetation, surface skin, snow, and soil. The SiB model also calculates heat, water, and momentum exchange between different land-surface compositions and the lowest layer of the atmospheric model. Land-surface processes are roughly divided into three groups that are individually related to canopy, snow, and soil. For the climate models, an upgraded version of SiB model (Hirai et al., 2007) is installed. The new version has improved treatment of soil and snow processes compared with the conventional version.

The model is optimized for a vector machine such as ES (Katayama et al., 2003; Katayama et al., 2004). Figure 2.1 shows a scalable performance of the 20-km mesh AGCM on the ES[2]. The parallel efficiency is very good from 12 nodes to 60 nodes. The computing efficiency with 60 nodes of the ES is about 35% of the peak performance. The execution time of the 24-hours forecast is about 6 minutes using 60 nodes of the ES.

Typhoon simulations of the 20-km mesh AGCM are compared with those of the JMA former operational GSM. Details on GSM are also available in JMA (2002). The dynamics of GSM is an Eulerian form. The resolution of GSM is T213L40, namely, triangular truncation 213 which is equivalent to about 60-km mesh horizontal grids and vertical 40 layers. Some physical processes in the forecast model of the 20-km mesh AGCM are

[2]This scalability test was implemented using former Earth Simulator computing system (i.e., ES1)

slightly different from those of the GSM as shown above. In addition to the differences, the 20-km mesh AGCM has also adopted recent revisions in some physical processes shown in Table 2.2. For the GSM simulations, outputs by the JMA operational routine are used. Hence, the GSM only adopts the revisions in Table 2.2 at the time the typhoon was predicted (e.g., the GSM does not adopt all the revisions for the 2002 typhoon simulation cases, whereas the 20-km mesh AGCM adopts them all). However, as Mizuta et al. (2006) pointed out, most of the settings in the physical parameterizations were tuned at the original resolutions of 60-km mesh. Some parameters in some physical processes were adjusted in their climate simulation for convenience, although they were not well verified. It is also uncertain that these adjustments yield good results for a simulation in a forecast mode. Therefore, these adjustments were not applied to the forecast simulations using 20-km mesh AGCM in this verification study[3].

2.2 Initial condition

A medium-range forecast experiment is an initial condition problem. Therefore, using appropriate initial data is necessary for medium-range forecasts to avoid a spin-up problem. Although it would appear to be better to use a data assimilation system for the above reason, the high resolution of the 20-km mesh makes it difficult to construct a data assimilation system because of lack of computer resources when this study was launched. Hence, the initial condition was obtained by interpolation from the 60-km mesh JMA Global Analyses (GANAL; JMA, 2002) to the 20-km mesh grids.

The typhoon structure in the original GANAL is changed into a somewhat blunt structure compared with the realistic typhoon structure so that the 60-km mesh GSM can resolve it. Therefore, a typhoon bogus insertion within the initial field (Iwasaki et al.,

[3]However, the adjustments were applied to climate projections in this study (see Section 3.1.1 for details.

1987; Ueno, 1995; JMA, 2002) was implemented to reproduce the suitable strength of tropical cyclone-like vortices so that the 20-km mesh AGCM can resolve at the high resolution. Figure 2.2 shows an example of the typhoon bogus implantation. Figure 2.2a displays the initial typhoon structure of an original GANAL. The central pressure is 992.19 hPa, which is much higher than the 960 hPa of the best-track data (the best-track data used in this study will be described in Section 2.4). On the other hand, Figure 2.2b shows the initial field with the typhoon bogus for a 20-km mesh model. The central pressure of the typhoon is 973.77 hPa, which is closer to the best-track data than the original GANAL. Although the typhoon bogus creates typhoon vortex quite realistically, the vortex does not seem to be exactly adjusted for the 20-km mesh AGCM. Kurihara et al. (1993) and Bender et al. (1993) pointed out that an insufficient initial typhoon vortex leads to a false spin-up for the first one or two days to adjust the initial typhoon structure by a finer resolution model; similarly, forecast experiments with the typhoon bogus in this study also showed a false spin-up in the early forecast stage, which was remarkably observed with intensity.

However, some preliminary experiments confirmed that typhoon forecasts with the bogus are superior to those without it in terms of intensity and position error. Hence, the typhoon bogus was applied in this study. To avoid such a spin-up, Kurihara et al. (1993) introduced an optimum initialization system to generate a vortex which is compatible with the physics and the high-resolution model. However, improving the typhoon vortex in the initial condition is beyond the scope of this study and will be a challenging task for the future.

Nevertheless, noise in an initial field, which is mainly caused by interpolation errors, cannot be negligible (see figure 14 in Murakami and Matsumura (2007)). In order to remove the noise, the preliminary study (Murakami and Matsumura, 2007) succeeded in developing an effective non-linear normal-mode initialization method for a high-resolution

AGCM; thus, a medium-range forecast with the AGCM becomes feasible. Figure 2.3 shows the overall experimental configuration for the typhoon forecasts for the 20-km mesh AGCM. The initial time of the forecast is 4 times a day (00, 06, 12, and 18 Universal Time Coordinated (UTC). The initial data is obtained by interpolation from the 60-km mesh GANAL, as mentioned above (see broken line in Figure 2.3). The time integration for each forecast is carried out for 96 hours. A deterministic 6-hour forecast during the 96-hour forecast was used for the incremental normal-mode initialization (Ballish et al., 1992; Murakami and Matsumura, 2007) at the next initial time (see box marked as "Guess" in Figure 2.3).

The output of simulations by the GSM is available by 90 hours. Basically, the output of the JMA operational routine is available only for forecasts started on 00 UTC and 12 UTC. However, in order to gain further statistical confidence, forecasts started on 06 and 18 UTC under the same setting of a routine GSM are implemented. For a homogeneous comparison with the 20-km mesh AGCM, simulations within 90 hours are evaluated.

2.3 Simulated typhoons

Twelve typhoons were selected for verification using the following subjective criteria while considering the limitation of the computational resources given by the ES;

- Hazardous typhoons which come close to or land on Japan,
- Typhoons that recurve (or never recurve),
- Recent typhoons from 2002 to 2005,
- Typhoons whose track was well (or badly) predicted by the GSM.

The list of selected typhoons and their experiment periods of initial time are summarized in Table 2.3. Those forecast dates almost overlap with the period of tropical storms analyzed (TS, when the maximum sustained wind is between 34 knots to 47 knots); severe tropical storm (STS, between 48 knots to 63 knots); and typhoon (TY, over 64 knots) as classified by WMO (2005). The characteristics of each typhoon are well described in JMA (2001-2005).

2.4 Best-track data

The simulated track position and intensity are verified with the post-analyzed best-track data distributed by the Regional Specialized Meteorological Center of Tokyo (RSMC-Tokyo), which is managed by the JMA. The data set provides the central position, central pressure, estimated 10 minute-averaged maximum sustained wind speed, and size (e.g., the radius of 30 knots and 50 knots). They are estimated from observations, namely, aircraft, satellite, surface, and upper air observations (Kamahori et al., 2006). In this study, the central position, the central pressure, the maximum 10 minutes-averaged sustained wind speed, and the radii of 30-knot and 50-knot winds in the data set are used as an observation. The radius is analyzed from a center of typhoon in four directions, namely, north, west, south, and east. When all directions of the radius are not missing, the average value is used to compare with the results of simulations.

The best-track data of the simulated typhoons are shown in Figure 2.4. In general, except for T0412 and T0513, most typhoons were generated on the south east of the Pacific Ocean approximately between 5 °N and 15 °N where the SST is high. Then, they moved northwestward while decreasing in central pressure and intensifying the maximum wind. At the time of or just before the recurvature, they reached their peak intensity. After recurvature, they changed their moving direction to northeastward with fast moving

velocity and proceeded to disappear.

2.5 Method to detect the position of a typhoon

The method for detecting the typhoon central position by simulations is the same as the method proposed by Sakai and Yamaguchi (2005) except for the mean sea level pressure (MSLP), for which outputs of 6-hour intervals are used. The method is as follows. At an initial time, the nearest position of the minimum MSLP points from the best-track position is defined as the central point of a typhoon. At 6 forecast hours, the minimum MSLP point within 500 km from the central point at the initial time is defined as the central point. After 12 forecast hours, the minimum MSLP point within 500 km from the point of the linearly extrapolated point by the last 2 forecast positions is defined as the central point. In the case of missing the minimum MSLP point, the tracking is terminated.

Radii of 50-knot and 30-knot wind velocity (hereafter referred to as R50 and R30, respectively) are also derived using 10-m wind components of the model output. The radii are firstly sought for all four directions (i.e., north, east, south, and west) from the center of a storm. When a grid value of 30-knot or 50-knot wind is detected for the first time, it is considered as an inner-core side and ignored because radii of outer-core side are focused here. When the radii are detected for the second time for all directions, they are averaged and compared with the best-track data. If any one radius is not detected, it must become a missing value. Here, in general, the wind speed is weaker on land than on the ocean. This is true for both the observation and simulated results. However, when a storm is close to land, the best-track data consider the land effect. Figure 2.5 shows an example. The northern positions of the radii are different from each other. When the above detecting algorithm is applied, the radius becomes small because the wind velocity

on land is very weak. On the other hand, the radius obtained by the best-track data is from farther to the north. If these differences are not taken into account, a small bias will always be present. To prevent this error, a third point of radius should be considered. However, in this study, the radius points on land were converted to missing data and not used for the analysis; in other words, only radius points on the ocean are evaluated.

2.6 Results and discussions

2.6.1 Position errors

Figure 2.6 presents all the results of the simulated tracks for the whole of experimental periods. When these results are viewed as a whole, most tracks by the 20-km mesh AGCM are very similar to those by GSM. The westward movement in the early developing stage of T0207, T0310, and T0421 was difficult to predict. The tracks by the 20-km mesh AGCM also show a noticeable northward bias in the developing stage. Although the bias of the 20-km mesh AGCM is slightly smaller than that of the GSM, it does not seem to be significantly improved by the resolution increase. One of the possible reasons for the northward bias is that the cumulus parameterization scheme in the GSM produces a cold bias at the lower troposphere over the middle and low latitudes (Nakagawa, 2003). This leads to a systematic negative error in geopotential height over the western portion of the North Pacific high. It is indicated that the induced weak subtropical high causes a northward bias. Figure 2.7 shows composite large-scale field for the T0207 cases which is only averaged before the typhoon recurves (BR stage as explained later). It seems that the center of subtropical high shifts westward in the analysis, whereas those by models locate east of the analysis. The notable northward flow bias locates the edge of the subtropical high. It is also fairly obvious that westerly wind bias is seen between 15 ℕ and 20 ℕ latitude for both models. The strong westerly wind bias penetrates far east so that it

interrupts westward moving of typhoon. They are caused by the wrong position or the weakness of the subtropical high. There also exists cooling bias around the subtropical high. The degree of the cold bias of the 20-km mesh AGCM is less than that of the GSM, which results in smaller northward bias of the storm positions. Nakagawa (2003) pointed out that the cooling bias was alleviated by introducing an improved cumulus parameterization scheme (Table 2.2). The improved cumulus parameterization scheme is not included in the GSM for the simulation of T0207, but it is in the 20-km mesh AGCM. However, the northward bias was not dramatically improved by the 20-km mesh AGCM.

The other possible reason for the northward bias is the inappropriate initial data, mainly due to the lack of observations in the tropical area. Tokuno and Ohhashi (2003) conducted a forecast test with an assimilation using the QuikSCAT (Quick Scatterometer) wind data for the T0207 typhoon case. The authors showed that the northward bias is about 100 km reduced with the data. Although detail reasons for the improvement are not clear, the authors stated that root mean square error of temperature and geopotential height at 850 hPa level and temperature at 500 hPa level are decreased by the forecast with the QuikSCAT. It is inferred that correcting the errors of the large-scale field is mostly a key for improving northward bias. The GANAL, in which the current study was originally used, was not created using the QuikSCAT data.

Although the wrong timing of the recurvature (T0418, T0421, T0423, and T0514) is notable, the westward bias before the recurvature (T0421) is also remarkable in both models, and the tracks by each model do not seem to be significantly different. Figure 2.8 is the same as Figure 2.7 but for the T0421 case. In this T0421 case, the GANAL shows that the typhoon moves along the edge of subtropical high. Although the models simulate the subtropical high comparatively well in the early forecast hours, they can not simulate the westward propagation of the high-pressure system in the later forecast hours. As a consequence, northwesterly wind goes into the edge so that it interrupts northward

moving of typhoon. It is indicated together with the T0207 result that the error of the large scale field as subtropical high leads either northward or southward position error of typhoon systematically.

As for the cases of T0412 and T0513, which never experience recurvature, the track error of the 20-km mesh AGCM is almost the same as the GSM or slightly decreased. Because the large-scale field is not so different among models, it is indicated that if the large scale field is almost the same, the position difference between the 20-km mesh model and the 60-km mesh model is not so significant.

Figure 2.9 shows the statistics of the position error for all typhoon cases in which various typhoon stages are classified. Here, (a) displays the position error of all typhoon cases. All cases are classified according to the storm recurvature as (b) before recurvature (BR); (c) during recurvature (DR); and (d) after recurvature (AR). These recurvature stages are defined by the direction of typhoon motion. The BR is defined as the moving direction of 180–320 degree of the clockwise angle from the north; DR, as 320–10 degrees; and AR, as 10–180 degrees. All cases are also classified according to the storm intensity, namely, (e) TS, (f) STS, and (g) TY. In general, model differences regarding position error at each forecast hour are not statistically significant because of large variance and lack of sampling cases. The two-sided Student's t-test shows at most 40 percent significance for each hour between models. In spite of the small statistical significance of the model difference, some features can be seen in the figure.

In the early forecast hours, the two models show almost the same track errors for all stages. Approximately after 36 hours, the model difference becomes larger. When typhoons are in the stage of BR and AR, the position error of the 20-km mesh AGCM is less than that of the GSM. On the other hand, during the DR stages, the position error of the 20-km mesh AGCM is larger than that of the GSM in the later forecast hours.

Because the sampling number is small, it is insufficient to argue that the 20-km mesh AGCM causes larger bias at the DR stage. However, a few cases of the systematic larger error were seen in the T0514 simulations. Figure 2.10 shows an example. Both the 20-km mesh AGCM and the GSM could not predict the recurvature. After 24 forecast-hour, the bias of the 20-km mesh AGCM becomes larger. Because the large-scale field was not so different between the models (data not shown), it is indicated that some structure errors of the typhoon generate such bias. As seen in the Figure 2.10 case, the 20-km mesh AGCM strengthens the typhoon too strong while the analysis does not strengthen. Although the degree of the error by the GSM is less than that of the 20-km mesh AGCM, the difference between models and best-track data is large comparatively. The GSM also shows false intense tendency while the best-track data shows steady or slightly decay tendency. It is natural to assume that if typhoon becomes strong, its moving direction becomes difficult to be influenced by the large-scale flow. The reason of this false tendency during the DR stage is uncertain at the moment. One of the possible reasons is that convection in the models is too strong at the early forecast hours to adjust unstable initial field. Then the latent heat release promotes updraft at the center. Once the updraft becomes predominant, much more water vapor at lower levels may be collected at the center and promotes latent heat release. If such a feedback is truly happens in the models, the initial field structure is very critical for correct intensifying tendency. Although it is still uncertain, the key for the precise position prediction of the DR stage might be to correct intensity tendency or typhoon structure.

Evaluating the model difference of the position error by the intensity stages (Figure 2.9e–g) is difficult because most samples are in the TY stage and the sampling numbers for TS and STS are very small. In the TY stage, however, there are small differences of position error between models. Although the statistical significance is low, the 20-km mesh AGCM simulates the typhoon positions as realistically as the GSM.

Figure 2.11 shows a scatter diagram of the position error at 72 forecast hours decomposed into the along/across moving direction relative to the best-track storm position. The ordinate represents the error along the direction the storm is moving, whereas the abscissa represents the error across the direction the storm is moving. Here, three stages are classified as Figure 2.9b–d, namely, (a)–(b) BR, (c)–(d) DR, and (e)–(f) AR. During the BR stage, the positive errors of the across moving direction (i.e., northward bias) are distinct. Although the positive errors would appear to be mainly due to the T0207 typhoon, as seen in Figure 2.6b, they are seen in almost every typhoon case. Note that this northward bias in the BR stage is also seen in most operational global models in the world (Wu et al., 2000; Sakai and Yamaguchi, 2005). Except for the positive errors, the negative bias is also large in the both models. This bias was remarkable in the case with T0421 as seen in Figure 2.6h. Overall, the forecasted central position is broadly distributed around the analysis position and not so different among models. As for the DR stage, there are fewer differences among models. When it comes to the AR stage, negative errors along the storm moving direction (i.e., slow bias) are remarkable for both models. Figure 2.12 shows the scatter diagram as same as the Figure 2.11 but for AR stage for each forecast hour. The large slow bias after the recurvature is mainly notable at the later forecast hours so that it is due to the model error rather than the initial condition error. Figure 2.13 is the same as Figure 2.7 but for the all typhoon cases in the AR stage. It is interested that the cold bias by the both models is seen around the subtropical high and the strength is weaker than the analysis. There also exists warm bias at the north flank of the jet stream around Japan. It is considered that decreasing meridional temperature gradient results in weakening the jet stream by the thermal wind relation. Although there is room for more work to clarify the reason for the warm bias, the slow bias seems to be caused by the error of the weak jet stream.

Figure 2.14 also shows the distribution of the systematic bias of the mean position (vector) and sea level pressure (contour) verified on two-degree grids for the 24 and 72

forecast hours, in which all typhoon cases are averaged. When the biases of position are viewed as a whole (the bias of the sea level pressure will be discussed in Section 2.6.2), the bias in the 24 forecast hours is clearly less than that in 72 forecast hours. Furthermore, both models show quite similar patterns of erroneous direction and magnitude at 24 forecast hours. There exists a general northward bias in the region south of 20 °N and between 125 °E and 155 °E at both of 24 and 72 forecast hours in both models. This indicates that a typhoon tends to go northward before recurvature, as is already pointed out in Figure 2.11. There also exists a large southward or southwestward bias in the region north of 25 °N. This indicates that the typhoon tends to move slowly after recurvature, as is also pointed out in Figure 2.11.

Overall, both models simulate storm tracks quite similarly. Furthermore, they share systematic northward and southward biases before recurvature and slow bias after recurvature. The fact that the difference of the simulated track between the 20-km mesh AGCM and the GSM is small indicates that a refining resolution is not the only key to reduce track errors.

2.6.2 Intensity verification

The typhoon intensity, namely, the central pressure and maximum sustained wind, is compared between models.

Figure 2.15 and Figure 2.16 show the simulated central pressure and maximum sustained wind, respectively. When viewed as a whole, the GSM predicts both the central pressure and maximum wind too weakly, while the 20-km mesh AGCM predicts them as strongly as, or stronger than, the best-track data. In particular, the variance of the 20-km mesh AGCM seems to be larger than that of the GSM. It is also notable that, even in the decay stage of a typhoon, the 20-km mesh AGCM tends to increase the max-

imum wind and decrease the central pressure in the early forecast time and then decrease the maximum wind and increase the central pressure (see (d) T0314, (e) T0406, and (g) T0421). This insufficient tendency is mainly due to the spin-up, as described in Section 2.2. However, except for the spin-up, the 20-km mesh AGCM seems to show quite a good decaying tendency. The geographical error of central sea level pressure can be seen in Figure 2.14. As a whole, the GSM shows a systematic positive bias both at (a) 24 and (c) 72 forecast hours, which is mainly due to the coarse resolution. However, the absolute error value of the 20-km mesh AGCM (b and d) is relatively smaller than that of the GSM. It is also noted that there is negative error by the 20-km mesh AGCM in the area, in which the position error is relatively large around the typhoon genesis area (between 140 °E and 160 °E in longitude and between 0 and 15 °N in latitude) and the typhoon decaying area (northern 30 °N). Although this error is likely to be mainly due to the large position error, the 20-km mesh AGCM yields an extremely low prediction of the central sea level pressure.

Figure 2.17 shows the tendencies of central pressure. The tendencies are evaluated by distinguishing three stages. One is the intense stage, in which the observed typhoon records a 10 hPa decrease between 24 and 72 forecast hours. Another is the steady stage, in which the observed typhoon records a decrease of between –10 hPa and 10 hPa. The other is the decay stage, in which the analyzed typhoon records a 10 hPa increase. In the intense stage, the GSM cannot simulate the typhoon deepening tendency. Most of the simulated central pressure records more than 960 hPa. This is due to the coarse resolution. The 20-km mesh AGCM, however, can simulate the deepening tendency better than the GSM. Some simulations by the 20-km mesh AGCM also reach 920 hPa, which is close to the analysis. (whether this close value is good or not for the 20-km mesh model will be discussed later). However, it must be noted that there are some bad cases in the 20-km mesh AGCM in which the central pressure does not decrease as much as in the analysis. Although the reason for the discrepancy is uncertain, Oouchi et al. (2006) and

Knutson and Tuleya (2004) suggest that it may originate in the insufficient performance of the physical scheme, including the cumulus parameterization. It may also be caused by insufficient initial condition because most of the central pressure for these cases at the 24 forecast hours (i.e., "A" in Figure 2.17a) is higher than that by the observation. This insufficient typhoon structure may prevent a typhoon from intensifying. Also, in the steady stage, the 20-km mesh AGCM shows decreasing sea level pressure too much more than the observation. When this tendency is evaluated between 72 and 90 forecast hours (data not shown), the erroneous tendency was not so strong as it is seen between 24 and 72 hours. Therefore, the insufficient typhoon structure in the initial field seems to cause such a false tendency. Although further analysis is required, it is natural to assume that the 20-km mesh AGCM has better potential than the GSM to simulate intense tendency.

For the cases of the decay stage, the 20-km mesh AGCM represents the declining tendency better than the GSM. However, some simulations show lower central pressure than the analysis at the 24 forecast hours. Those cases, in which the central pressure records less than 910 hPa by the 20-km mesh AGCM, are due to spin-up. All of the cases decrease the central pressure from the initial condition to 24 hours and then increase it from 24 hours. Except for these cases, the 20-km mesh AGCM represents the decaying tendency more adequately than the GSM. Figure 2.18 also shows the tendencies in the maximum wind velocity. The basic features are almost the same as the result of central pressure. It must be noted that the GSM cannot simulate an intensifying tendency that exceeds 50 knot by analysis. The 20-km mesh AGCM, however, represents the tendency more accurately than the GSM.

Overall, the 20-km mesh AGCM has better possibility than the GSM to simulates the strength tendency.

2.6.3 Typhoon structure

A comparison between the infrared image by a satellite and the expected image by simulated outputs helps to visually grasp the structure of a storm. Figure 2.19 is a comparison of satellite infrared image by the GOES (Geostationary Operational Environment Satellite)-9 and that by model simulations. The infrared image by the model simulations is derived using a radiative transfer model based on a method in the GSM (Oowada, 2006). In this case, it is conspicuous that the typhoon structure by the GSM is very vague (e.g., the eye is not resolved). On the other hand, the typhoon structure by the 20-km mesh AGCM is much finer than that by the GSM. For example, it is noted that the typhoon eye is well resolved by the 20-km mesh AGCM. The central pressure was 955.0 hPa, 951.0 hPa, and 966.2 hPa for the observation, the 20-km mesh AGCM, and the GSM, respectively. The eye wall is also more realistic than that by the GSM. It is also remarkable that the cloud bands of the typhoon that run from northeast to southwest are much clearer than those by the GSM. It is reasonable to suppose that the high resolution enables it to represent the typhoon structure more realistically. However, when it is compared with observation carefully, the central structure, including eye walls, by the 20-km mesh AGCM seems to be too compact. The possible reason will be discussed later with a radial profile verification.

The simulated mean R30 and R50 are compared with those of the best-track data. Figure 2.20 shows the mean errors of R30 and R50. Generally, the differences between models are small. The error of R50 is, notably, almost zero or small negative bias. However, the negative bias of R30 is distinct. The negative bias means that strong winds are simulated too close to the eye of the storm. Although the error difference between the recurvature stages is small, the BR (c) stage shows relatively larger error than other stages. It is also noted that the bias in the initial condition (forecast zero hour in the Figure 2.20) is relatively large compared with other forecast hours. This indicates

that there is considerable room to improve the initial condition for better experiments. However, as the error of R30 is increased by the forecast hour, there are some deficiencies in the model's physical processes. As Mizuta et al. (2006) described, these errors can be alleviated by some adjustments to the physical processes.

Figure 2.21 shows mean wind profile for each forecast time. It is noted that the maximum wind by the 20-km mesh AGCM is located around less than 100 km from the center of storms. However, it is located between 100 km and 200 km by the GSM. Because the grid interval of GSM is 60 km, it seems to be unable to resolve such a sharp structure of wind variation around the center of a storm. It is inferred from the R30, the R50, and the maximum wind velocity by the best-track that the position of maximum wind velocity is located less than 100 km from the center, which is close to the 20-km mesh AGCM profile. It is also notable that wind structures are changed by forecast hour by the 20-km mesh AGCM, whereas those by GSM are not changed. Although it is due to spin-up by the insufficient initial structure, the degree of spin-up is approximately alleviated after 60 forecast hours.

In order to remove the spin-up deterioration, Figure 2.22 shows the same as Figure 2.21, but for averaged typhoons whose maximum velocity is more than 50 knot after 60 forecast hours. It is interested that the outer-core structure, which is more than 200 km from the center, is almost the same between models. The difference is distinct in the inner-core structure. This gives us justification for the assumption that high resolution is required in order to evaluate typhoon strength, because high resolution makes it possible to capture the inner-core structure realistically.

Although it appears that the 20-km mesh AGCM simulates exact structure as same as the observation as it is seen in Figure 2.22, it is necessary to discuss how much resolution is enough to resolve the inner-core structure. In other words, what is the best-fitted

structure as its resolution? For example, one might think that the structure of the 20-km mesh AGCM is too deep as its resolution. In fact, the R30 and R50 verifications show that the structure of 20-km mesh AGCM is too more compact than GSM at later forecast hours. The author supposes that 20-km mesh is not still enough to resolve the inner-core structure so that wind profile should be underestimated when it is compared with the observation. Therefore it is important to evaluate the best-fitted structure as the 20-km mesh resolution. One of the hints to determine the best-fitted structure is the simulation tests with different initial typhoon bogus structures. If a spin-up is occurred as seen in 20-km mesh AGCM case of Figure 2.21, the initial structure is not considered to be the best fitted as the resolution. The initial structure of the GSM might be the best fitted as 60-km mesh because spin-up is not seen. One of the possible reasons of the too compact structure might be due to the insufficient cumulus parameterization scheme (from personal communication with a JMA model developer). Both the 20-km mesh AGCM and GSM overestimate weak precipitation which is less than 15 mm/day around tropics (Kamiguchi et al., 2006). It is indicated that shallow cumulus convection is easy to occur in the models. When this is applied to typhoon, it is inferred that deep convection does not occur easily at the outer-core side of the typhoon. As a result, shallower convection and water vapor are collected in the vicinity of the typhoon center so that deep convection is too strong around the center. For future work in order to clarify the structure error, the convection distribution conducted by a cloud resolving model may be beneficial information.

2.7 Summary

Tropical storms over the western North Pacific (WNP) were simulated by the 20-km mesh MRI/JMA-AGCM. The simulations were compared with the 60-km mesh GSM as a coarse global model in order to evaluate differences in resolution. The verification was conducted for twelve typhoon cases from 2002 to 2005.

The difference in the position errors of typhoons between the 20-km mesh AGCM and the GSM is very small, although the position error of the 20-km mesh AGCM seems slightly small. The performance of the track forecast seems to depend mainly on the large-scale flow, initial condition, and the physical process in the models rather than on the resolution difference. The statistics of the position errors are also classified into the different stages of a typhoon, namely, recurvature and intensity. The overall result is that position errors are almost identical between models. The 20-km mesh AGCM simulates the typhoon positions as realistically as the GSM. According to the analyses of the northward bias in the T0207 cases and the southward bias in the T0421 cases, schematic errors in the large-scale field, which is associated with the erroneous strength of the sub-tropical high, were found. Also, the position errors of the 20-km mesh AGCM are slightly larger than those of the GSM during the recurvature stage. This mainly comes from the erroneous intensifying tendency because of initial spin-up problem rather than from the model bias itself. The position errors are also analyzed by along/across moving direction relative to the best-track position. As a result, both models show a northward bias before the recurvature stage and a slow bias after the recurvature stage. Because there are almost the same systematic errors of large-scale field for both models, they are mainly caused by error of the physical process. As a whole, these results indicate that refining the resolution is not the only key to reduce position errors.

However, there are significant differences in intensity (maximum sustained wind and central pressure) predictions, mainly due to the resolution difference. As a whole, the GSM simulates both the central pressure and maximum wind too week, whereas the 20-km mesh AGCM simulates them quite realistically but somewhat too strong. It is also remarkable that the 20-km mesh AGCM can simulate the intense or decay tendency much more realistically than the GSM. These results indicate that the 20-km mesh AGCM has better predictability on the intensity of tropical cyclones than the GSM.

The typhoon structure was also compared from the view point of the radius of 30-knot and 50-knot winds. Although both models show a similar bias, there was a negative bias in 30-knot radius, namely, the typhoon structure of the wind was too compact. However, when the composite structure of the wind profile was compared, that of inner core by the 20-km mesh AGCM shows comparatively realistic structure, which has the sharp increasing of wind velocity within 100 km in the radius. This drastic transformation of structure seems to be unable to be resolved by the GSM.

On the basis of these results, it can be concluded that the 20-km mesh AGCM simulates typhoons more realistically than the GSM in terms of intensity and inner structure. However, as the statistical significance remains low because of limited computer resources, further cases should be implemented for a future study. It is also necessary to verify other tropical cyclones over other oceans. The systematic errors, which are common in both models, namely, north bias, slow bias, and a structure of strong wind that is too compact, seem to be due to a physical process or initial conditions. It is also important to evaluate the suitable typhoon structure as the model resolution. In other words, it is insufficient to modify the typhoon structure of the model just close to that of observation; otherwise the model shows false intensity tendency and deteriorate typhoon position forecast. Further investigations and improvements with regard to these issues will be necessary for producing further reliable climate simulations and medium-range forecasts.

Table 2.1: Specifications of the models used in this study.

	(a) Forecast Models		(b) Climate Models		
Name	GSM	20 km-mesh AGCM	60 km-mesh AGCM	120 km-mesh AGCM	180 km-mesh AGCM
Truncation Wave Number	T213	TL959	TL319	TL159	TL95
Horizontal Grids Number	640 × 320	1920 × 960	640 × 320	320 × 160	192 × 96
Grid Spacing in Degree	0.5625	0.1875	0.5625	1.1250	1.875
Vertical Layers	40	60			
Model Top	0.4 hPa	0.1 hPa			
Advection Scheme	Eulerian Form	Semi-Lagrangian Scheme (Yoshimura and Matsumura, 2003)			
Cumulus Convection	Prognostic Arakawa-Schubert (Randall and Pan, 1993)				
Cloud Process	Prognostic Cloud Water Content (Smith, 1990)				
Radiation Process	NPD/JMA (JMA, 2002)	NPD/JMA (JMA, 2007)	Shibata and Aoki (1989), Shibata and Uchiyama (1992)		
Boundary Layer Scheme	Mellor-Yamada Level 2 (Mellor and Yamada, 1974)				
Gravity Wave Drag	Iwasaki et al. (1989)				
Land Surface Model	Simple Biosphere Model (SiB version L1; Sato et al., 1989)		Upgraded Simple Biosphere Model (SiB version 0109; Hirai et al., 2007)		
Chapter in Use	2		3, 4, and 5	3	

Table 2.2: List of the recent major revisions in the physical processes for the 20-km mesh AGCM.

Date	Upgrade	Reference
28 May 2003	Improved cumulus convection scheme including the entrainment and detrainment effects between the cloud top and the cloud base in convective downdraft.	Nakagawa (2003)
29 Jul 2004	A simple parameterization scheme for marine stratocumulus.	Kawai and Inoue (2006)
29 Jul 2004	Improved cloud water/ice scheme.	Kawai (2003)
02 Dec 2004	A new long-wave radiation scheme.	Murai and Yabu (2005)

Table 2.3: List of all simulated typhoons.

Typhoon Name	Typhoon Number	Number of Cases	Dates of Forecast
Chataan	T0206	48	Jun 29, 2002 – Jul 11, 2002
Halong	T0207	38	Jul 07, 2002 – Jul 16, 2002
Etau	T0310	25	Aug 03, 2003 – Aug 09, 2003
Maemi	T0314	32	Sep 06, 2003 – Sep 13, 2003
Dianmu	T0406	34	Jun 13, 2004 – Jun 21, 2004
Meranti	T0412	20	Aug 04, 2004 – Aug 09, 2004
Songda	T0418	45	Aug 27, 2004 – Sep 07, 2004
Meari	T0421	37	Sep 20, 2004 – Sep 29, 2004
Ma-on	T0422	23	Oct 04, 2004 – Oct 09, 2004
Tokage	T0423	33	Oct 12, 2004 – Oct 20, 2004
Talim	T0513	17	Aug 29, 2005 – Sep 02, 2005
Nabi	T0514	41	Aug 29, 2005 – Sep 08, 2005

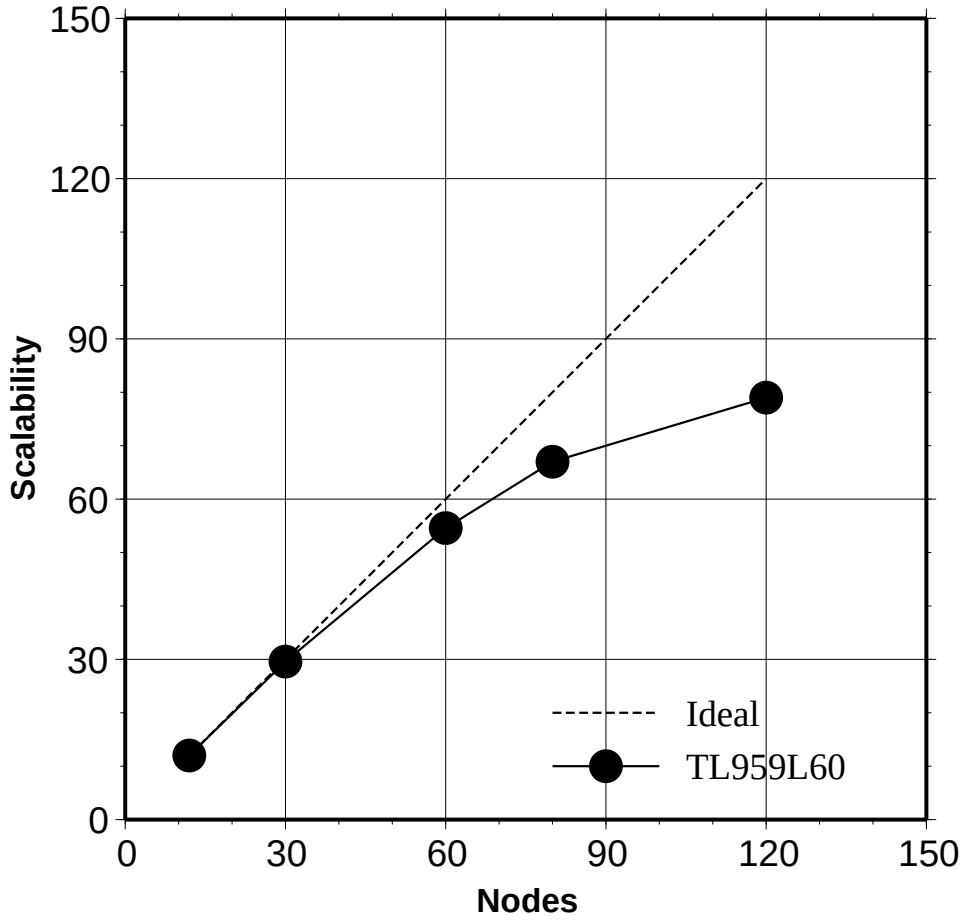

Figure 2.1: Scalability performance of the 20-km mesh AGCM on the Earth Simulator. The model resolution is TL959L60.

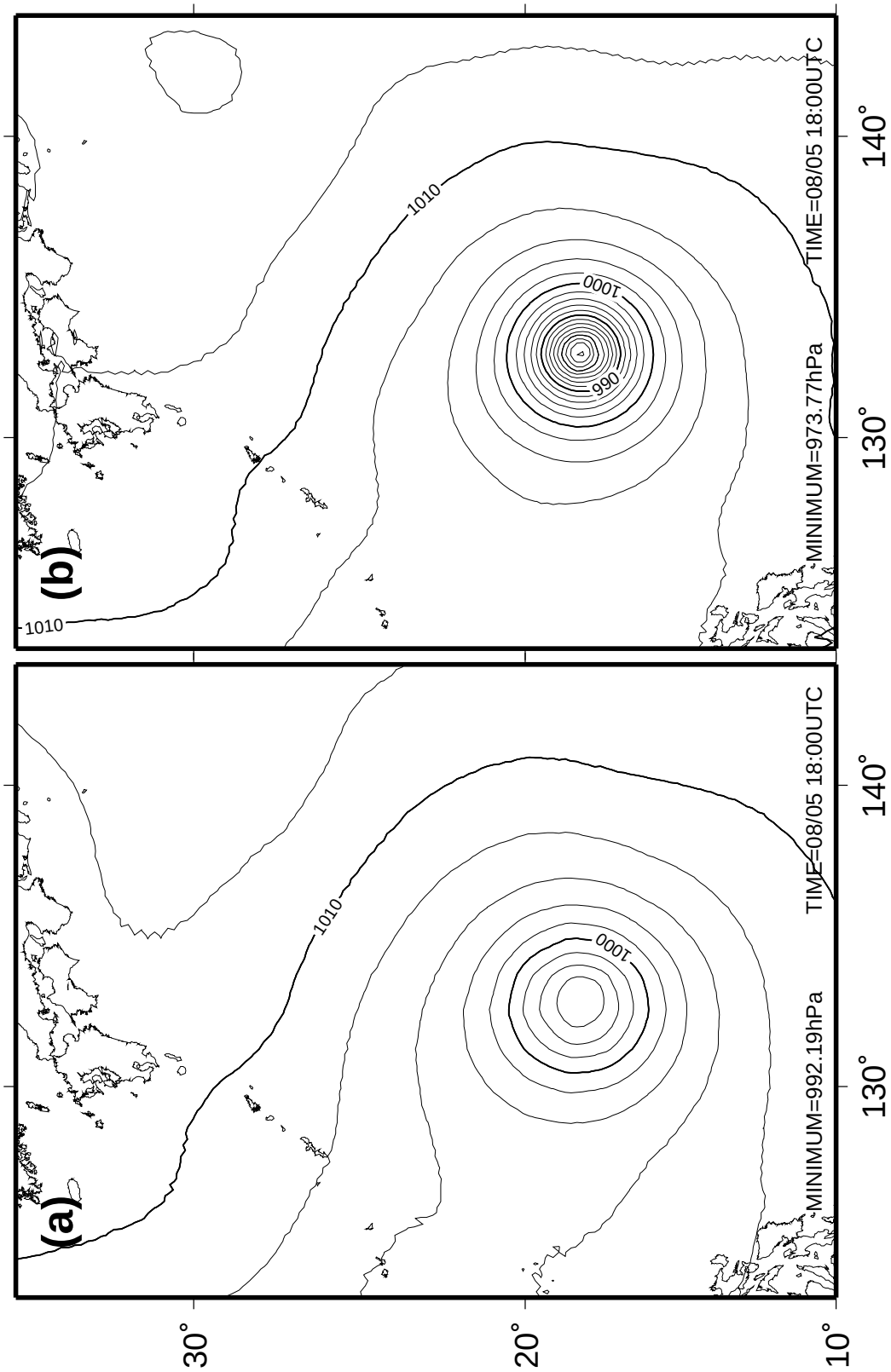

Figure 2.2: (a) The original GANAL. (b) The 20-km mesh initial field with the typhoon bogus. The central sea level pressure of the original GANAL is 992.19 hPa, whereas that of the 20km-mesh initial field is 973.77 hPa. The best-track data shows 960 hPa at the same time of 18UTC on August 5 of 2003.

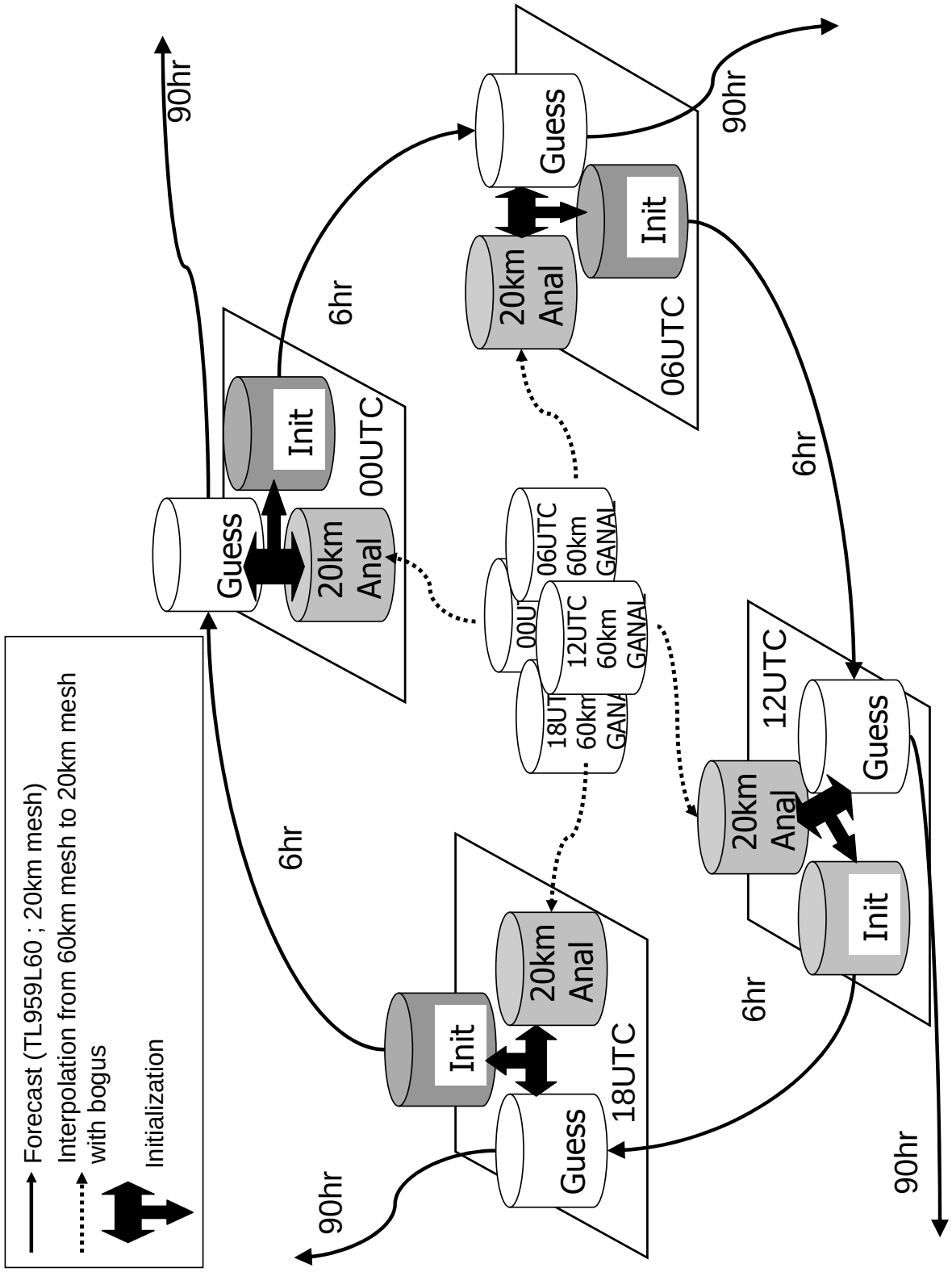

Figure 2.3: The boxes "60km GANAL", "20km Anal", "Guess", and "Init" correspond to the original 60-km mesh analysis, interpolated analysis, first-guess, and initialized data, respectively. The broken line is the interpolation and the typhoon bogus. The thin arrows are deterministic forecasts, and the thick three-pronged arrows are the new initialization scheme.

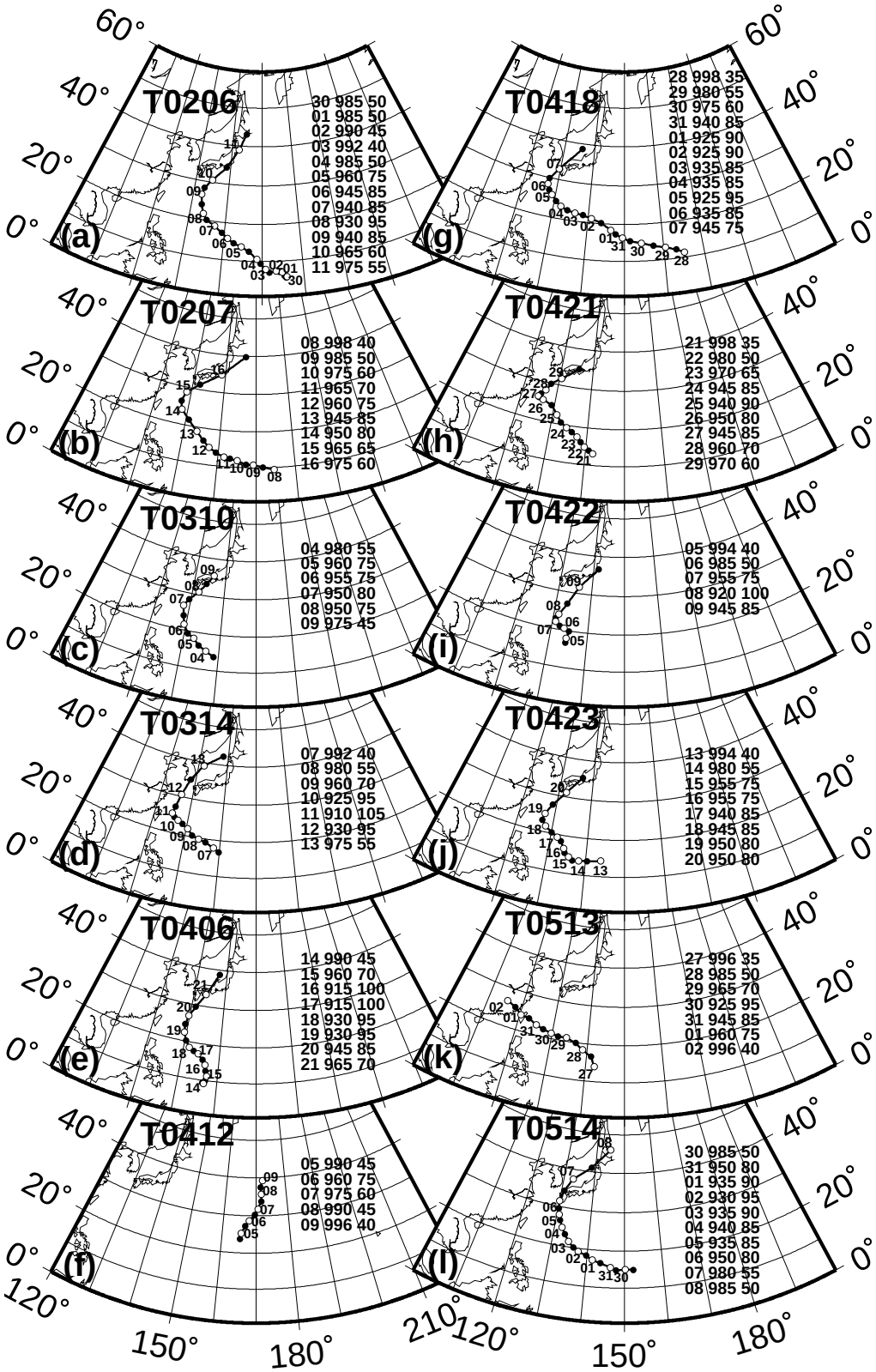

Figure 2.4: Best-track data by the RSMC-Tokyo Typhoon Center for (a)T0206, (b)T0207, (c)T0310, (d)T0314, (e)T0406, (f)T0412, (g)T0418, (h)T0421, (i)T0422, (j)T0423, (k)T0513, and (l)T0514. An open circle and a closed circle are the positions at 00 UTC and 12 UTC, respectively. The numbers along the tracks show the date at 00 UTC. The numbers of the right side of each panel describe the date, central sea level pressure (hPa), and maximum sustained wind (knot) from left, respectively.

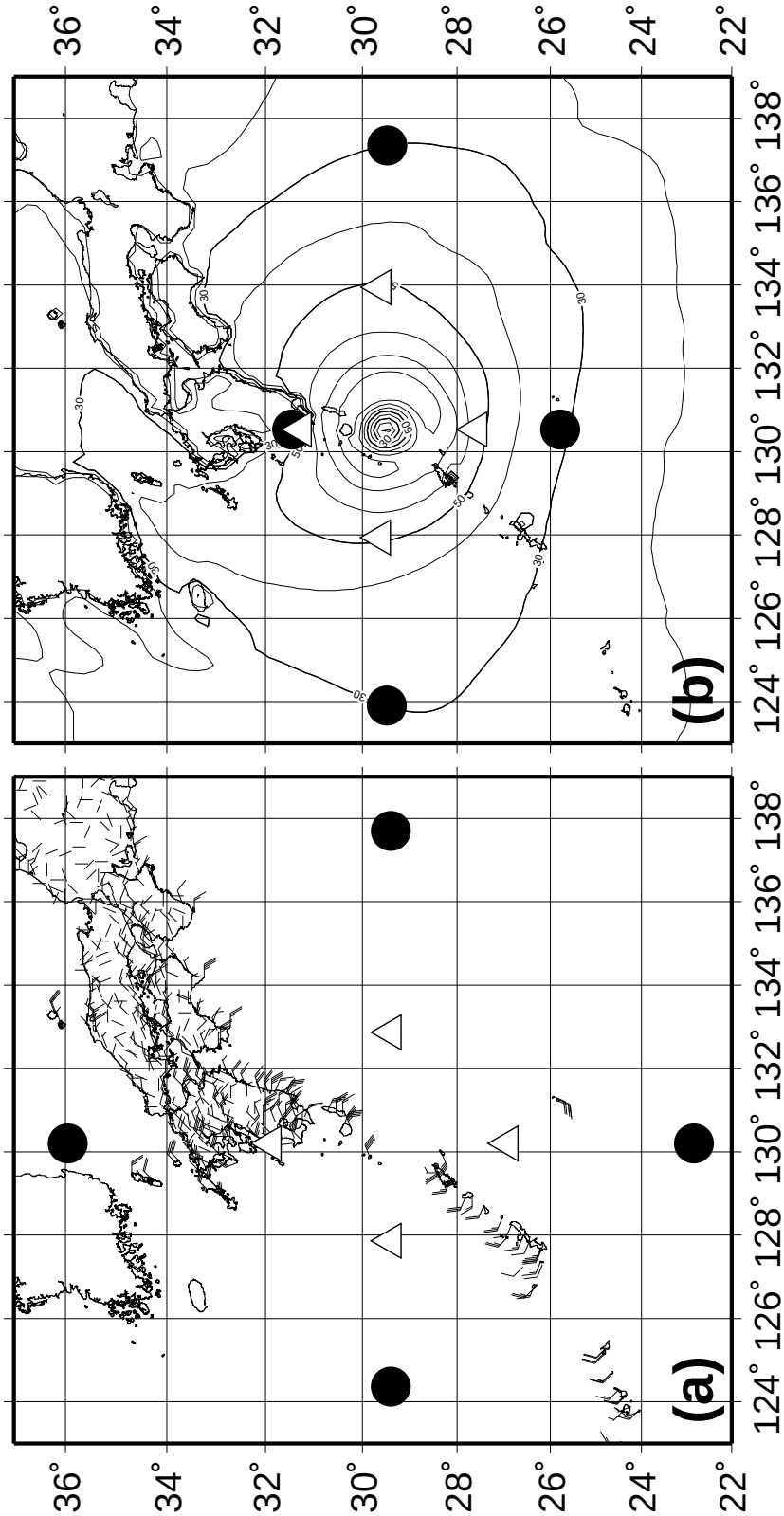

Figure 2.5: Land effect on detecting radius of 50 knot (R50) and 30 knot (R30). Position of R50 and R30 (a) by the best-track data and (b) by the 20-km mesh AGCM. The winds arrows in (a) are by the Automated Meteorological Data Acquisition System (AMeDAS; one wing is equal to 10 knots). The black circles show the positions of R30, whereas the white triangles show the positions of R50.

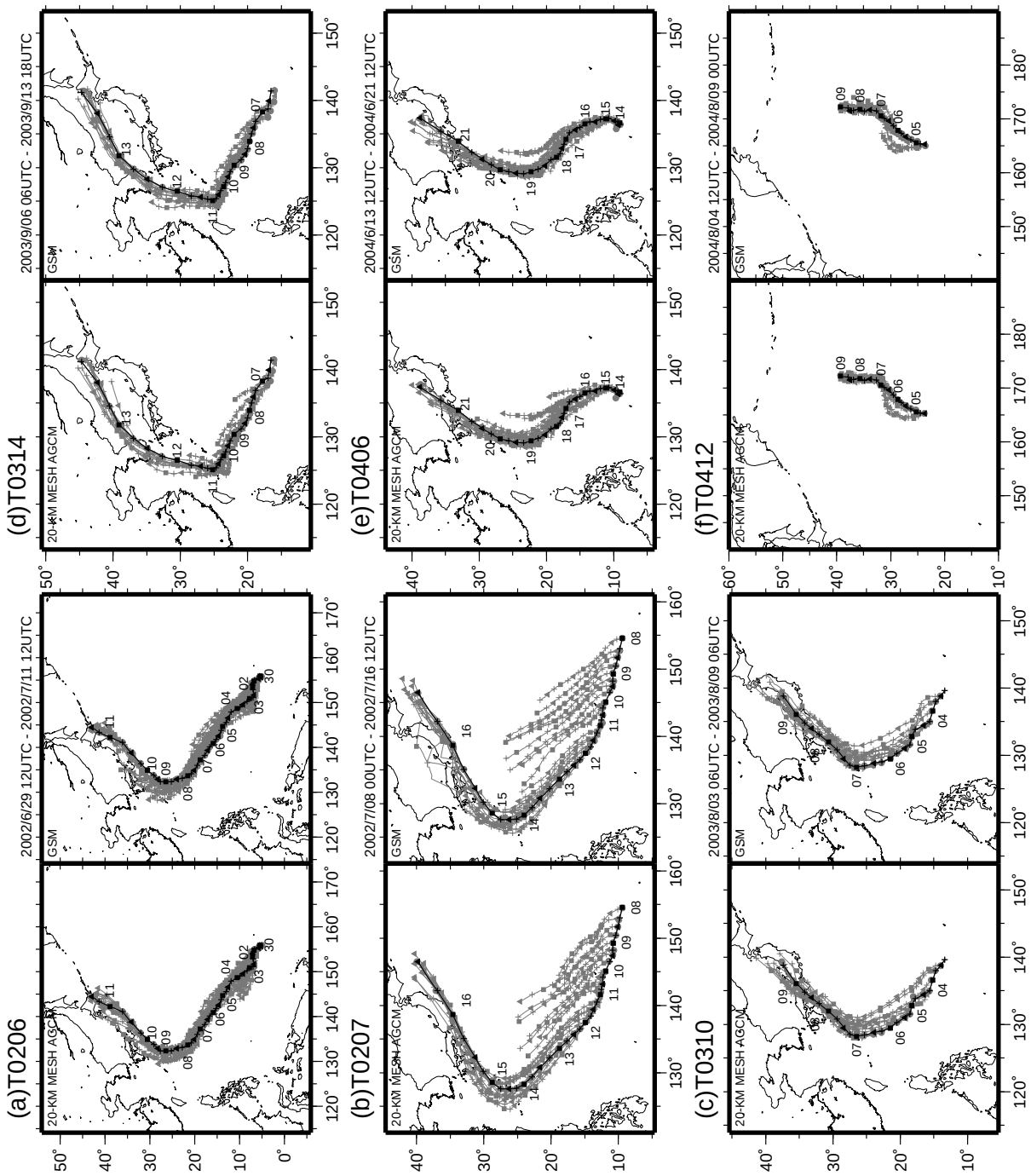

Figure 2.6: Simulated typhoon tracks. The left and right panels of each typhoon show the results according to the 20-km mesh AGCM and the GSM, respectively. The gray lines are according to the models. The black lines are according to the best-track data. The numerical annotations denote dates.

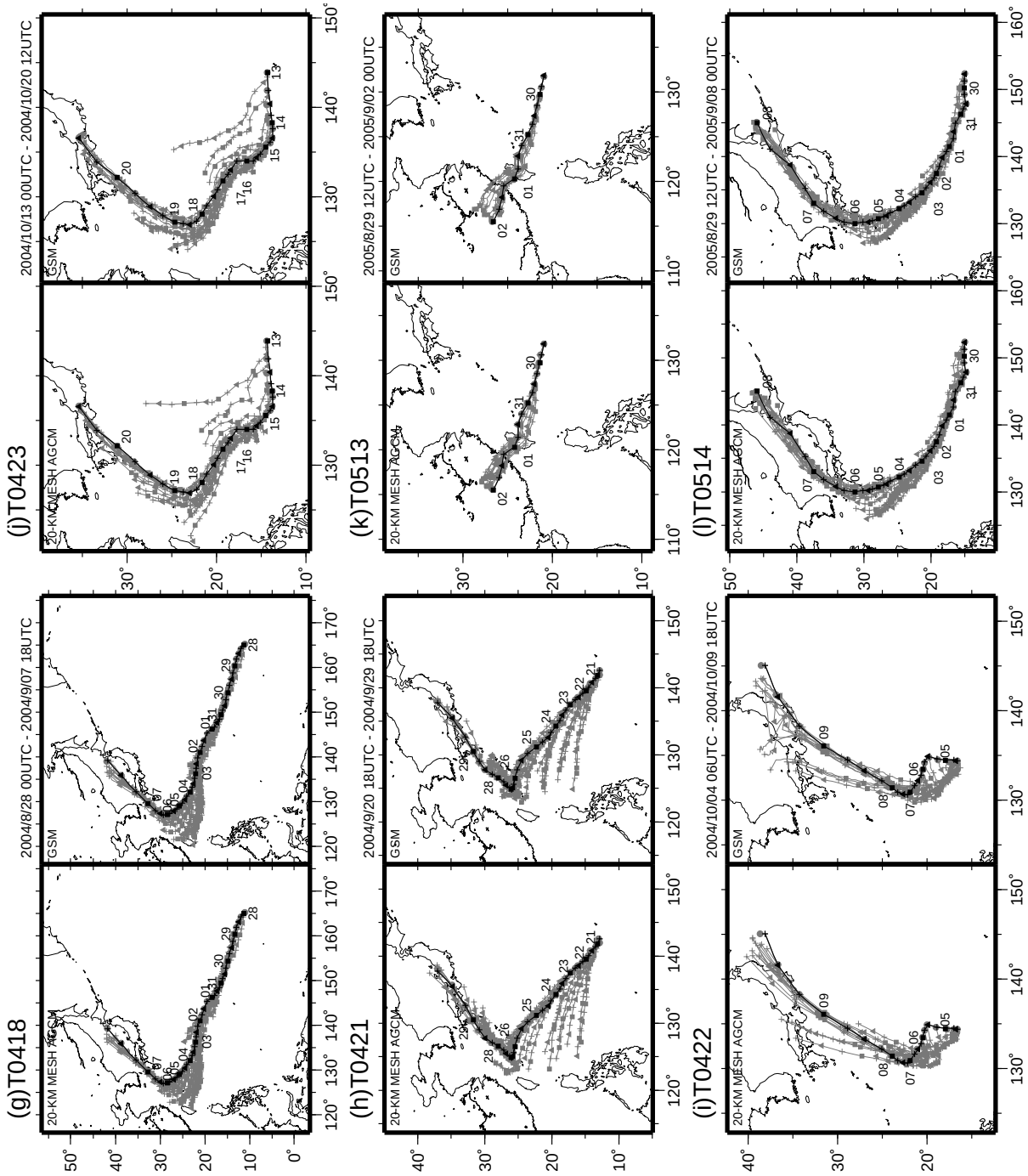

Figure 2.6: (continued)

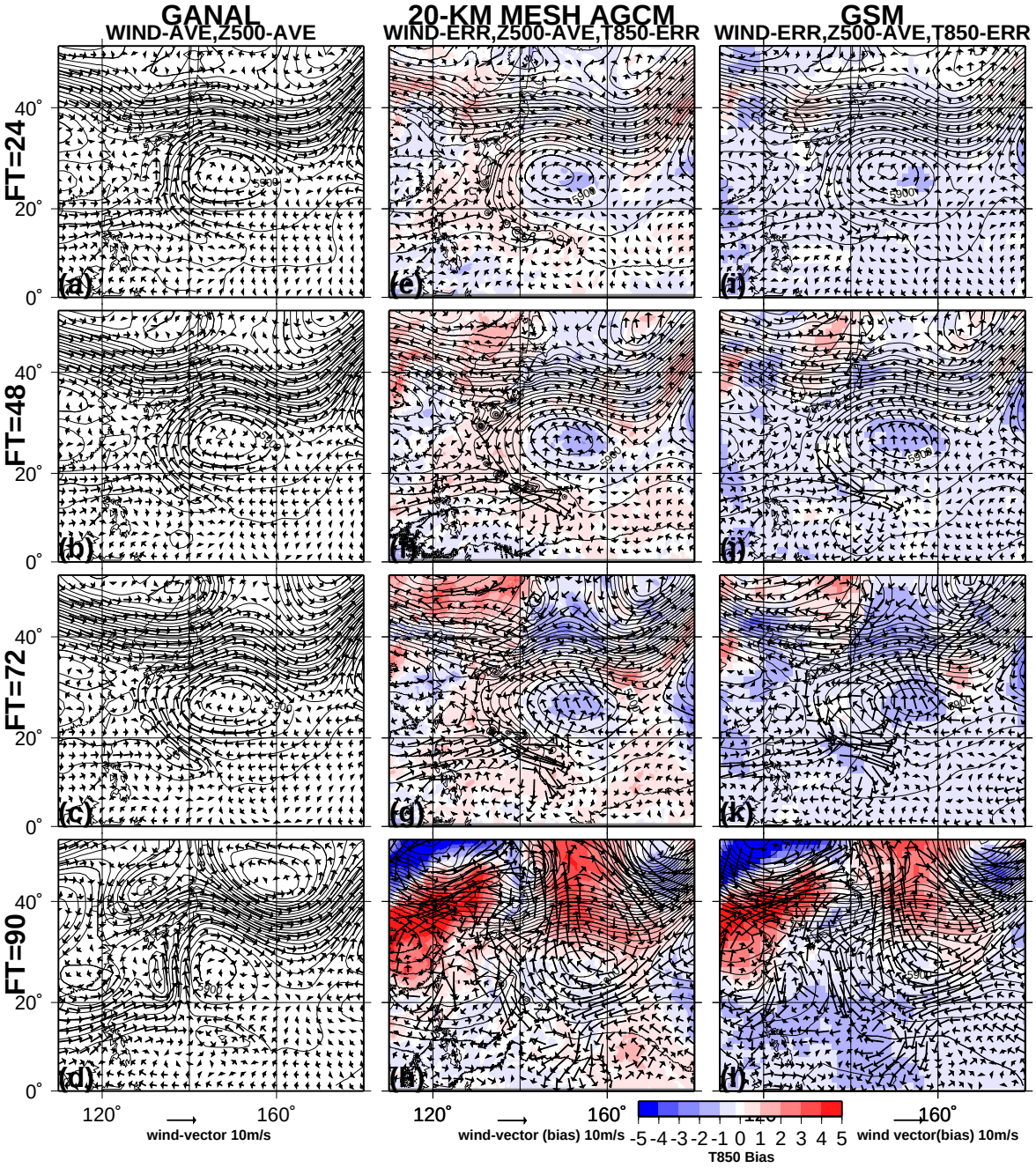

Figure 2.7: Composite large-scale field for the T0207 which is averaged before the typhoon recurves. The left panels are averaged analysis field. The contour lines show geopotential height at 500hPa (Z500). Vectors show weight-averaged wind from 1,000 to 300 hPa (WIND). The middle panels are by the 20-km mesh AGCM, and the right panels are by the GSM. The contour lines are Z500, the vectors show WIND bias against analysis, and the colors show temperature bias at 850 hPa level.

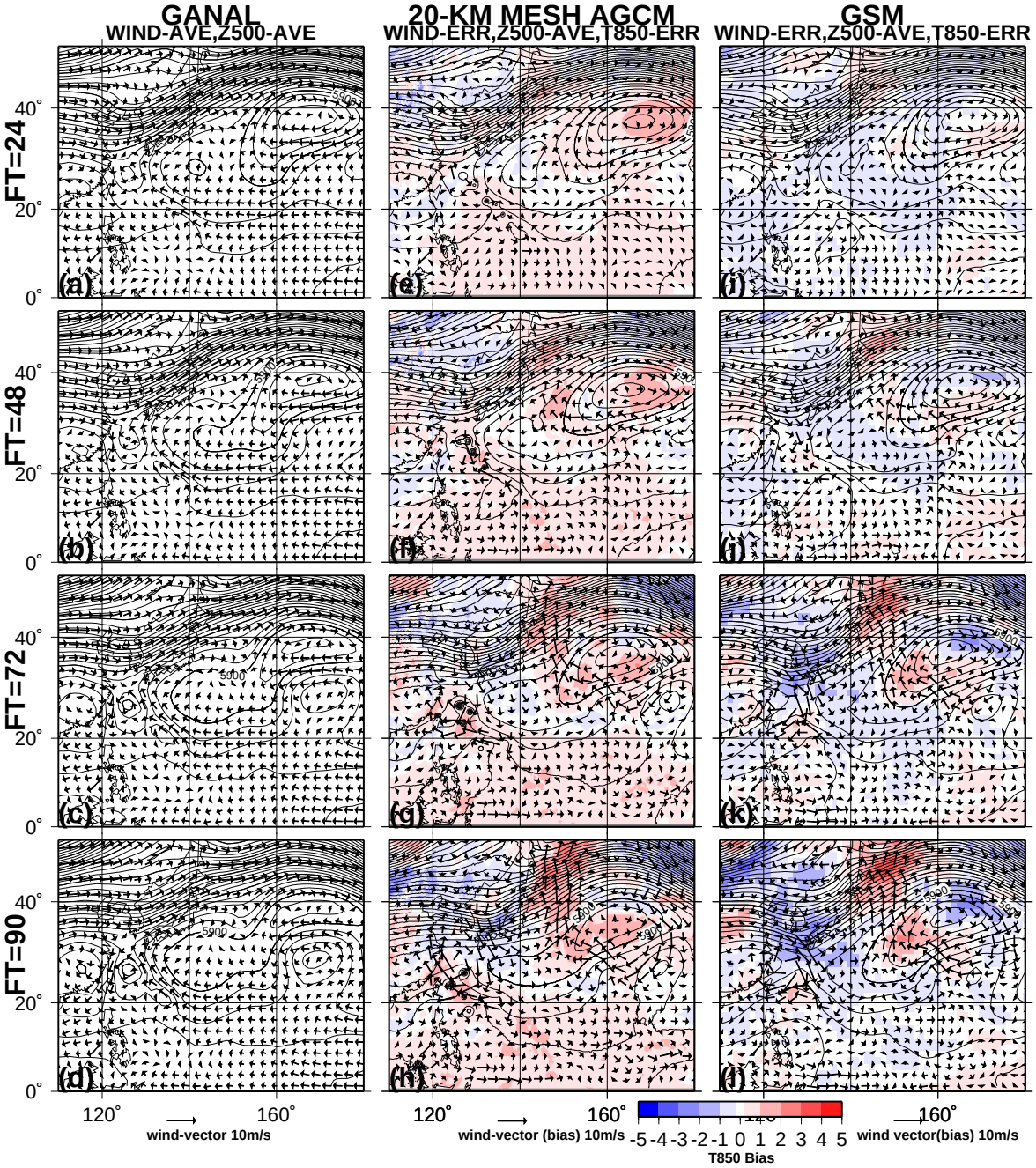

Figure 2.8: Same as Figure 2.7 but for T0421 case.

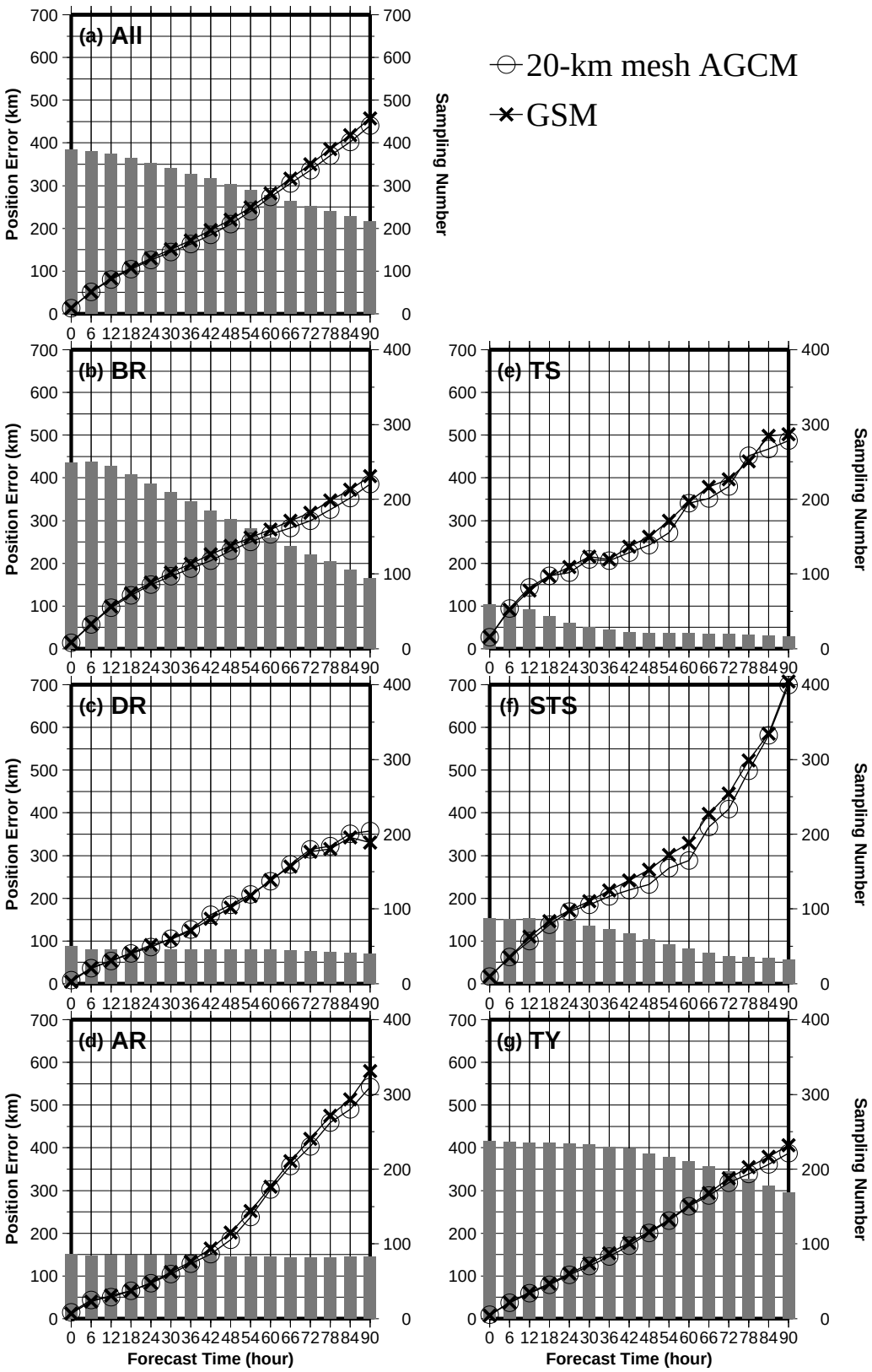

Figure 2.9: Simulated position error (km). (a) is the position error for all cases. All cases are classified according to the moving direction as (b) before the recurvature (BR); (c) during the recurvature (DR); and (d) after the recurvature (AR). All cases are also classified according to intensity as (e) TS; (f) STS; and (g) TY. The open-circle plots show the error by the 20-km mesh AGCM, and the cross plots show the error by the GSM. The sampling number is shown in the histogram.

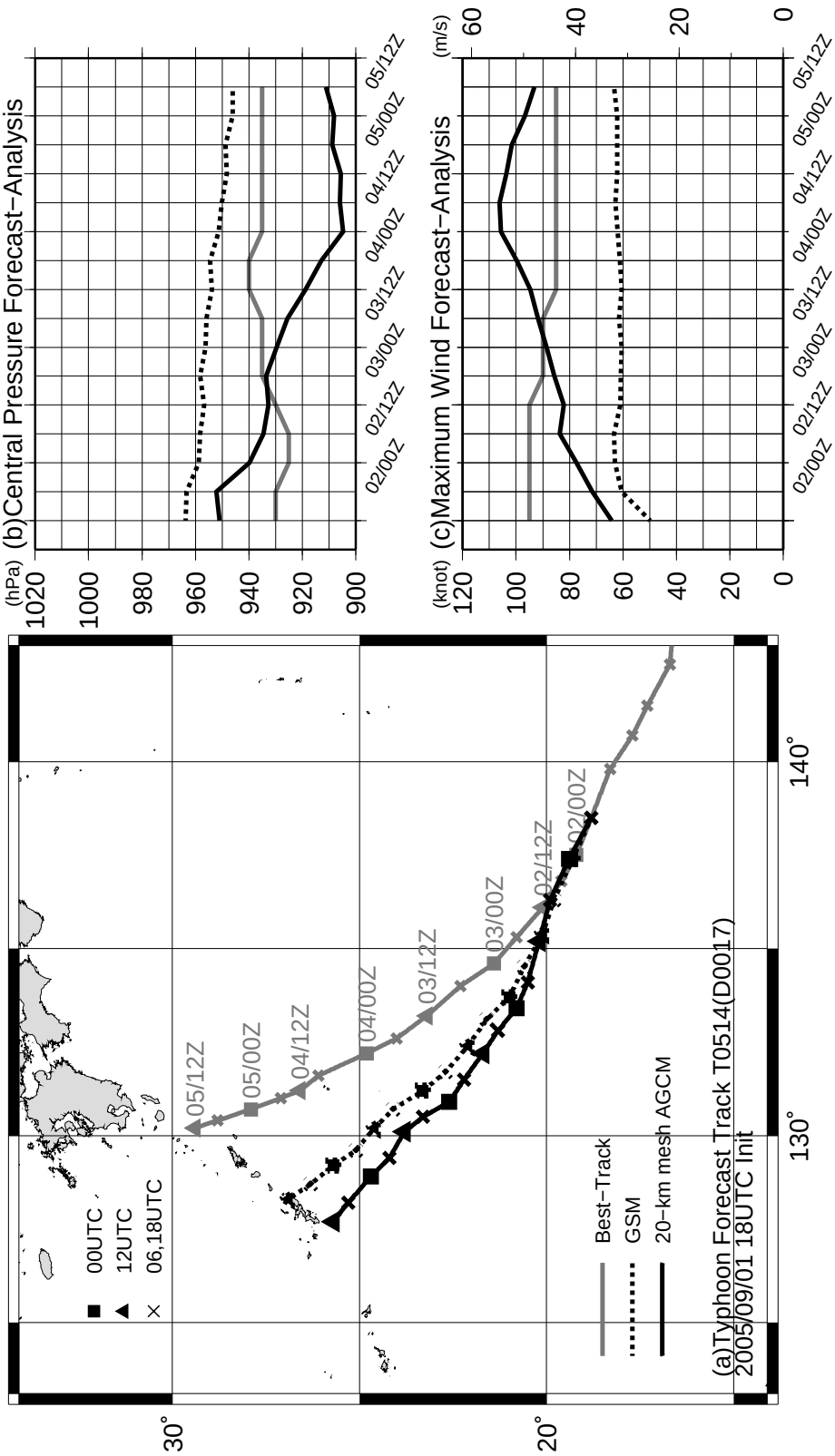

Figure 2.10: An example of position error in the DR stage of T0514 case. (a)the typhoon position, (b) the central pressure, and (c) the maximum wind. The black-solid lines are by the 20-km mesh AGCM, the black-broken lines are by the GSM, and the gray lines are by the best-track. The initial time is 18UTC on September 5 of 2005.

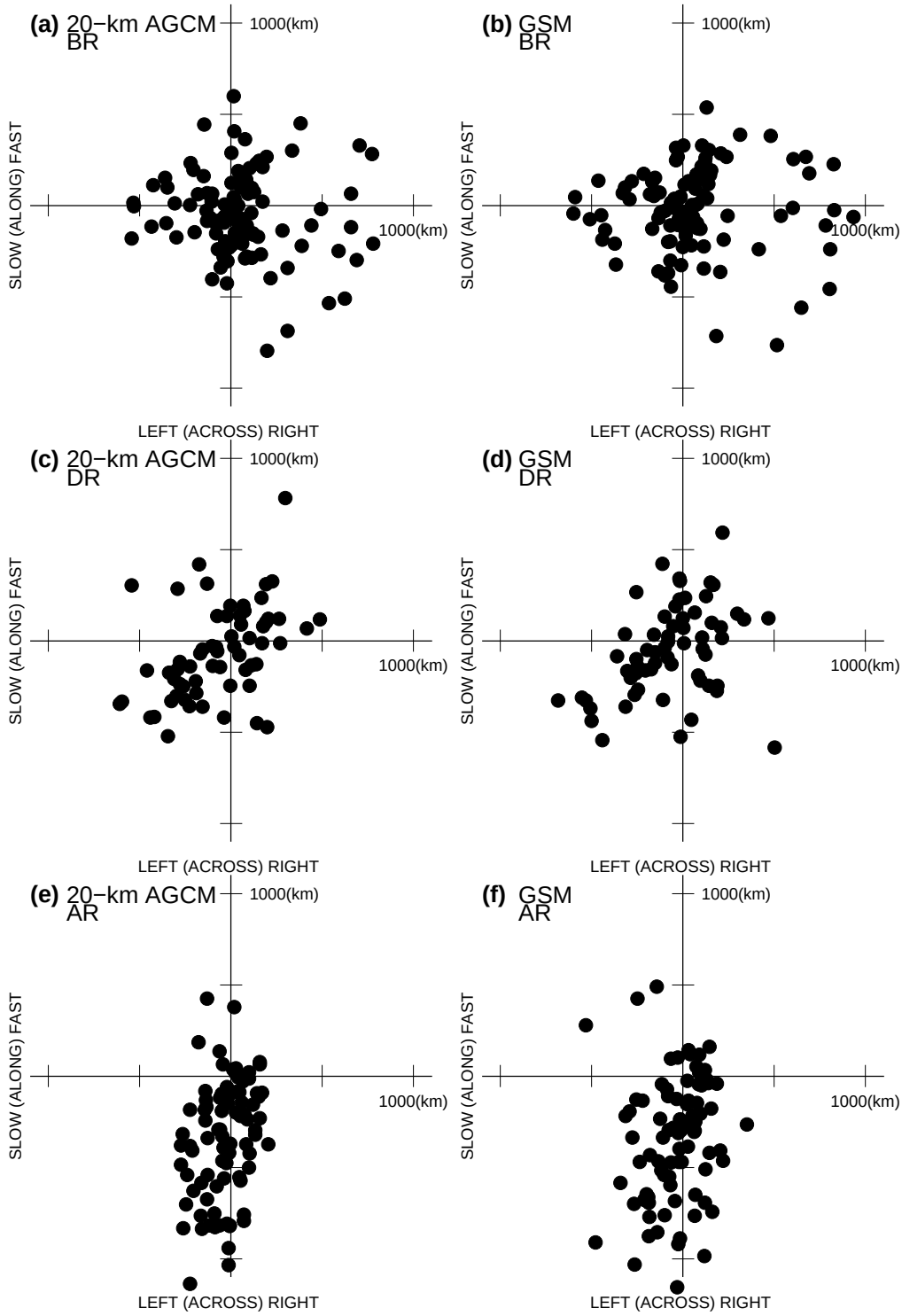

Figure 2.11: Simulated central typhoon position along/across the moving direction relative to the storm position of analysis. The typhoon positions at 72 forecast hours are plotted for (a)–(b) as before the recurvature (BR), (c)–(d) during the recurvature (DR), and (e)–(f) after the recurvature (AR) stage. (a), (c), and (e) are according to the 20-km mesh AGCM; (b), (d), and (f) are according to the GSM. The abscissa and ordinate represent the error of the across moving direction and the along moving direction, respectively.

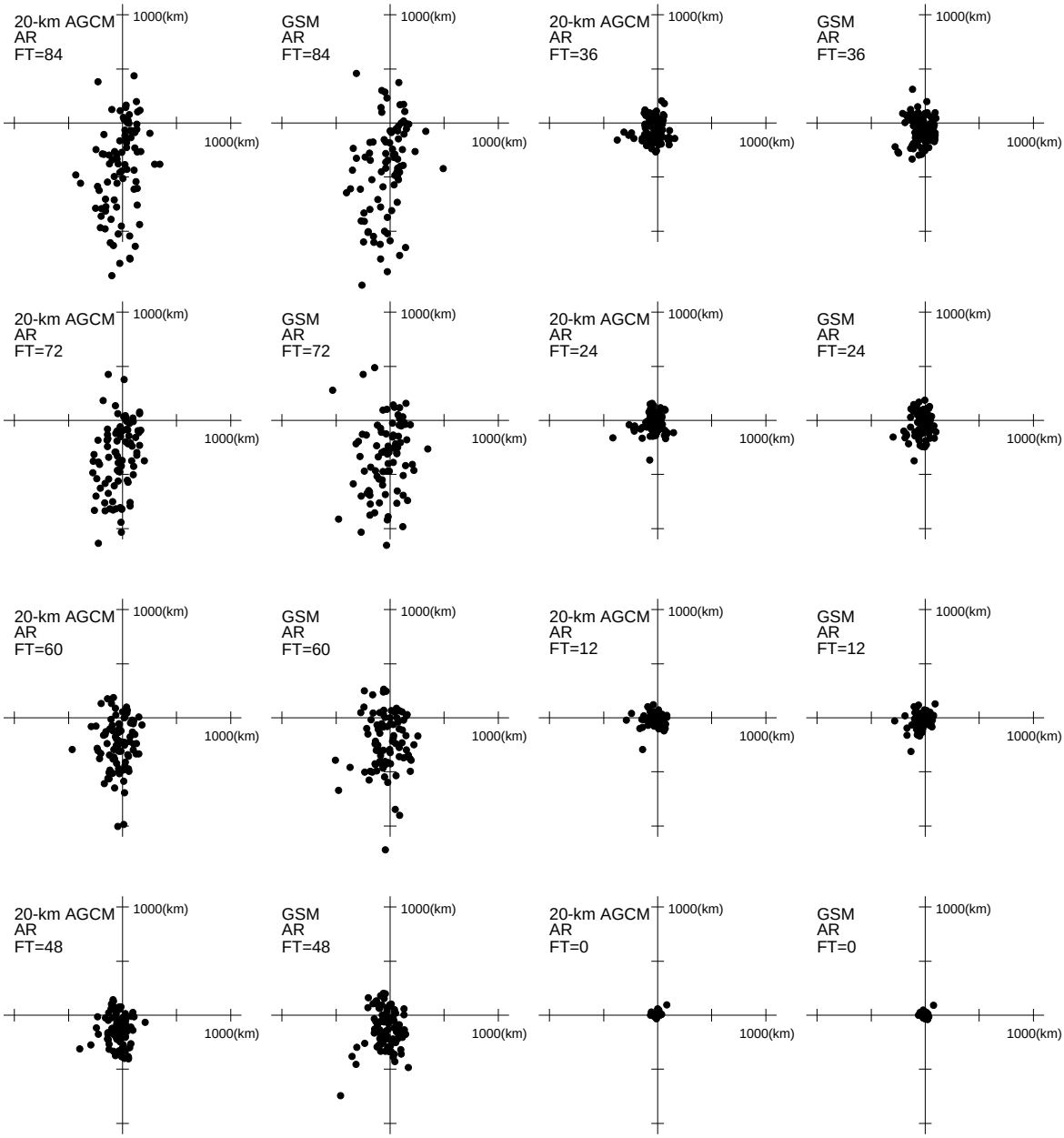

Figure 2.12: Same as Figure 2.11 but for AR stage for each forecast hour.

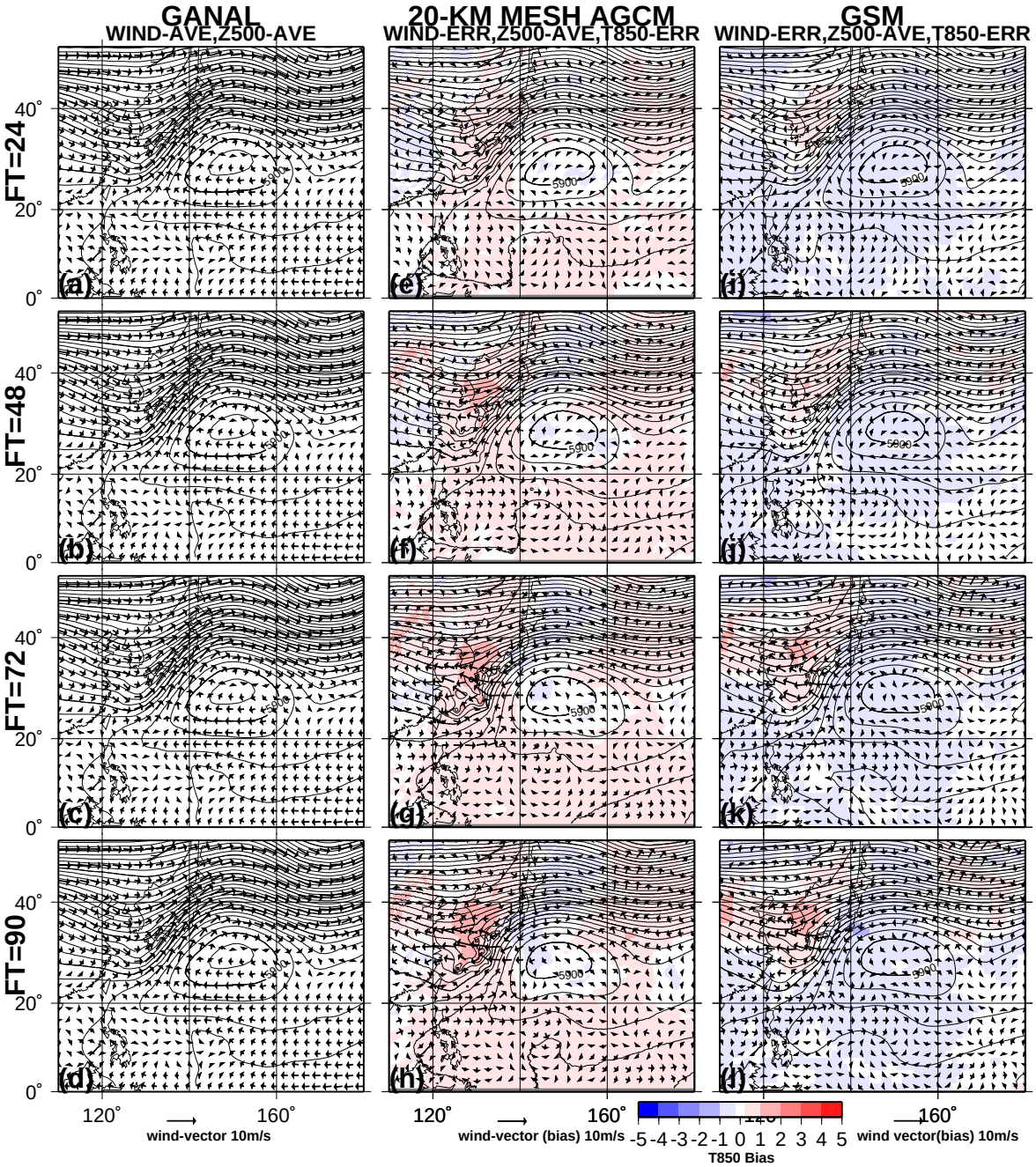

Figure 2.13: Same as Figure 2.7 but for the all typhoon cases in the AR stage.

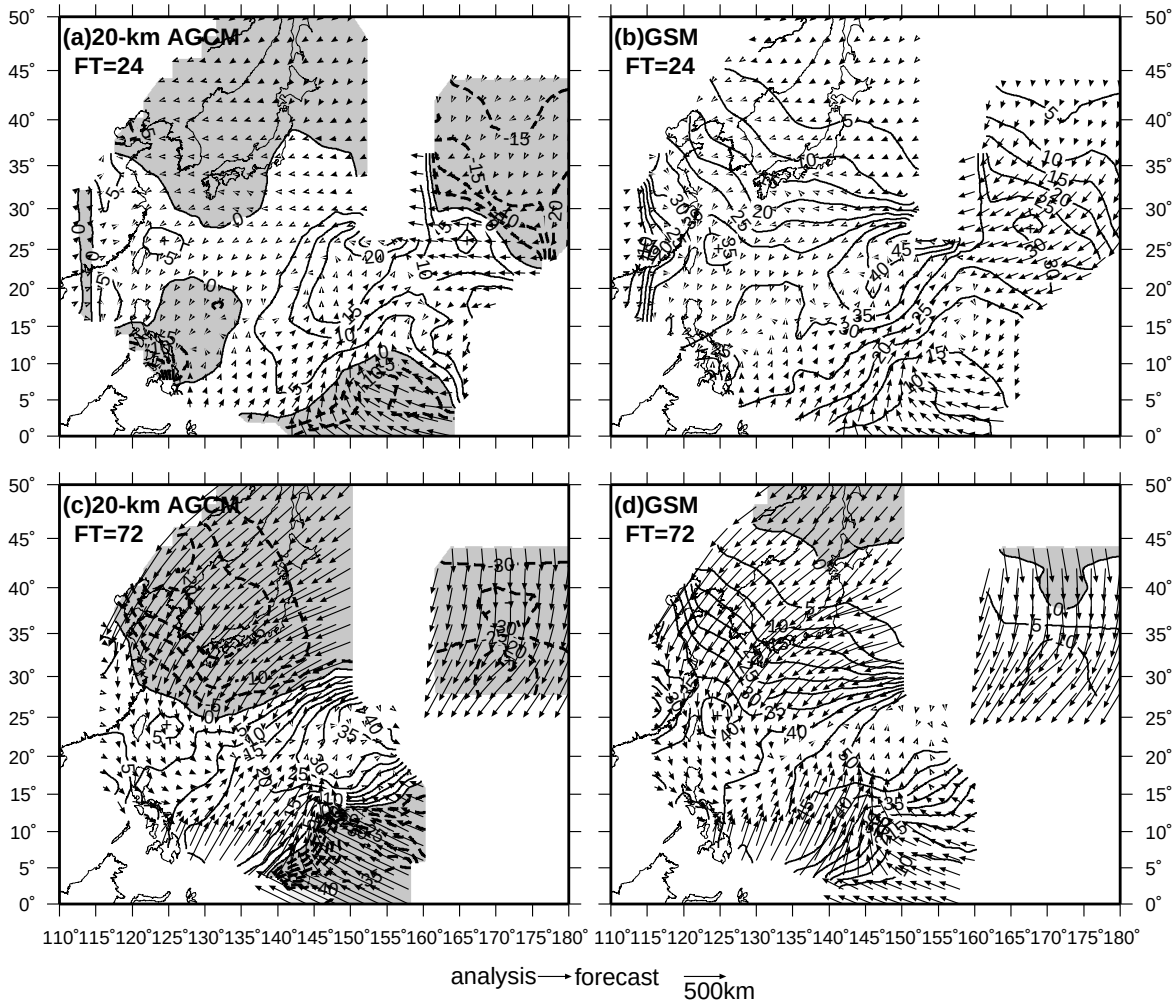

Figure 2.14: Systematic bias of the mean position (vector) and sea level pressure (contour; hPa). The head, tail, and length of each arrow show the model forecast position, the best-track position, and the magnitude of the mean position error, respectively. Errors at 24 forecast hours (a) by the 20-km mesh AGCM and (b) by the GSM are shown. (c) and (d) are the same as (a) and (b) but for 72 forecast hours.

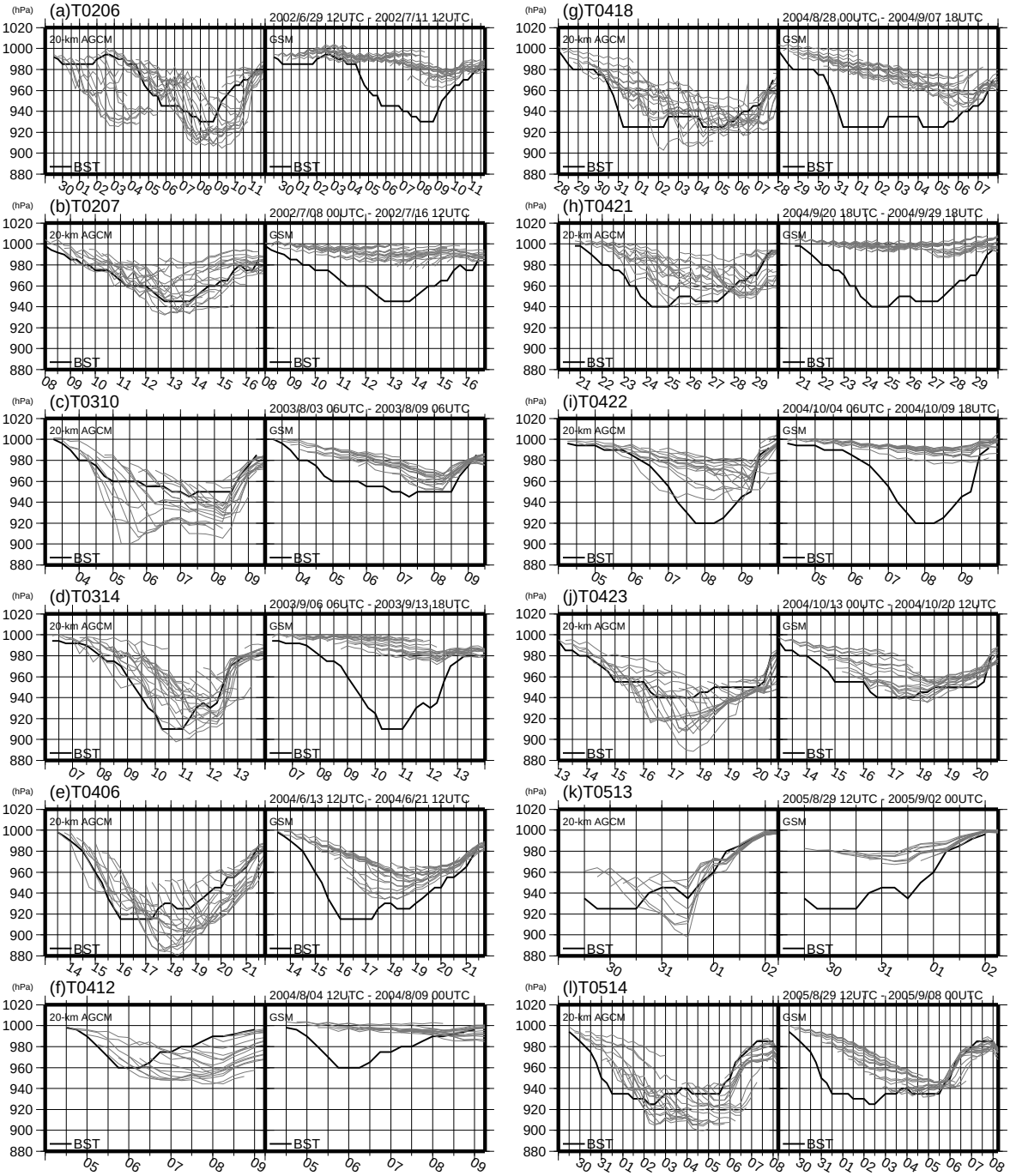

Figure 2.15: Simulated typhoon central pressure by each model. For each typhoon, the left panel shows the central pressure (hPa) by the 20-km mesh AGCM, whereas the right panel shows that by the GSM. The gray and black lines display the central pressure simulated by the model and best-track data, respectively. The numerical annotations of the abscissa denote the date.

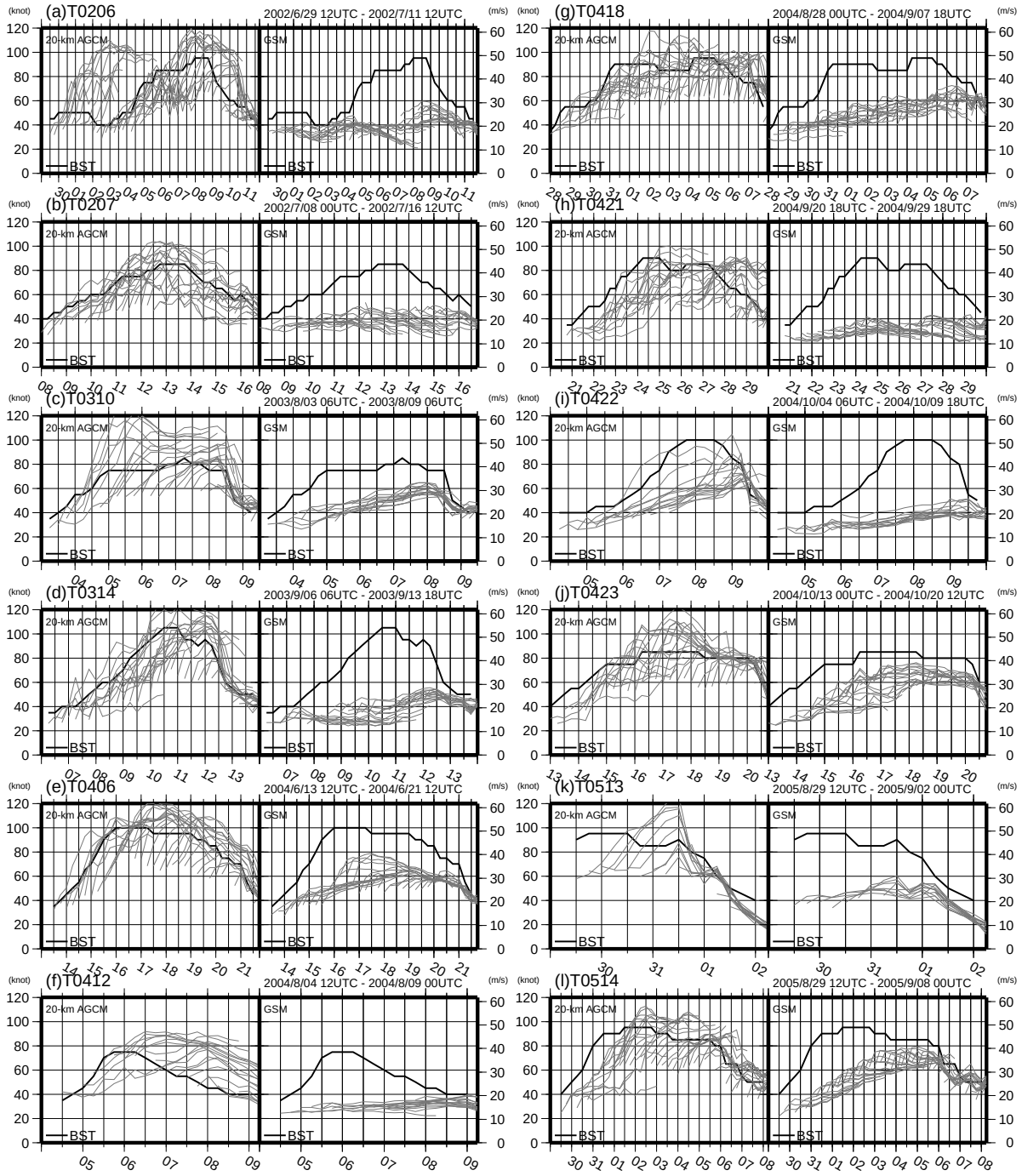

Figure 2.16: Same as Figure 2.15 but for the maximum sustained wind [knots]. The unit of the wind velocity that corresponds to ms^{-1} is shown in right ordinate.

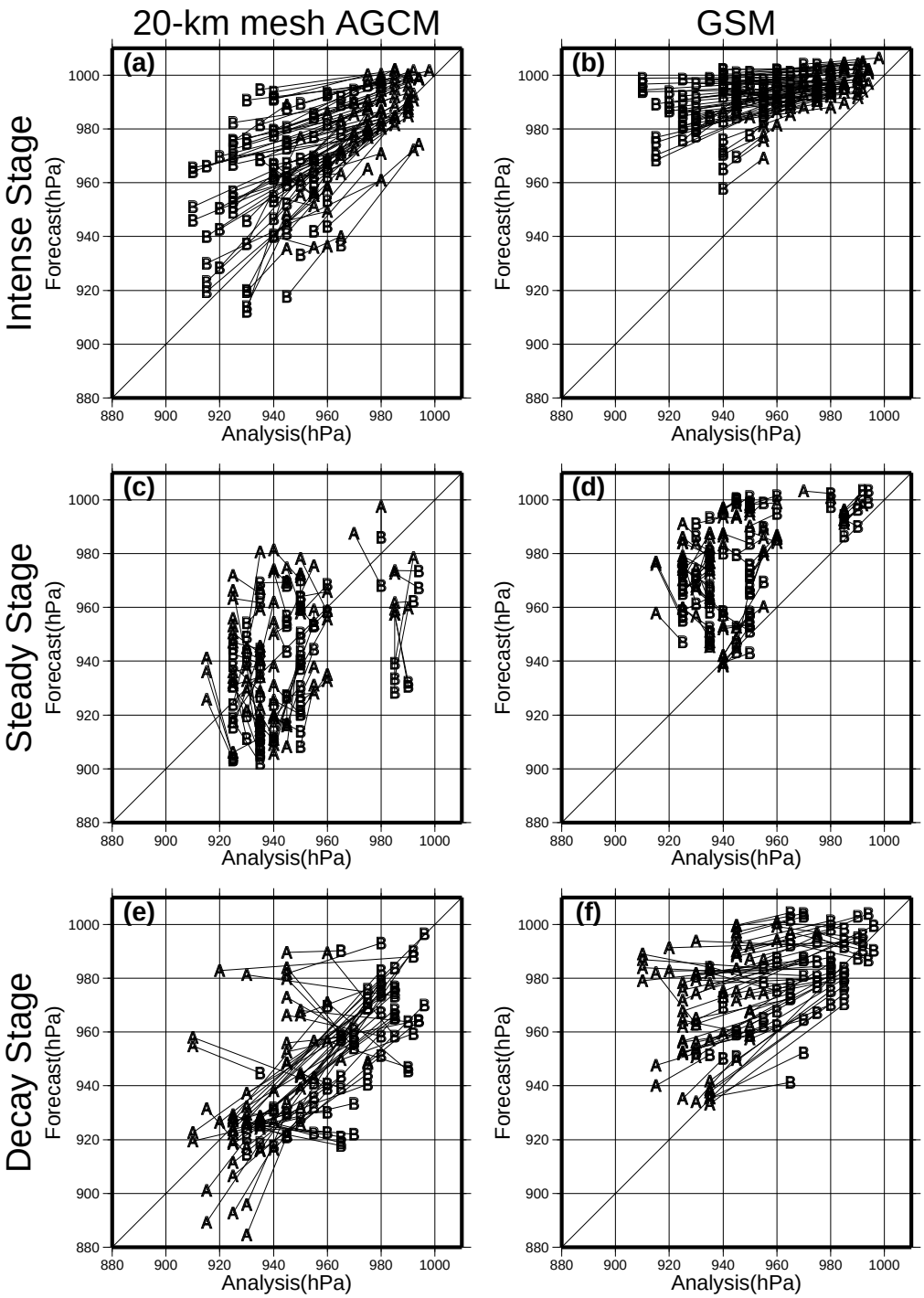

Figure 2.17: Tendency of the central pressure. The unit is hPa. The ordinate is the simulated central pressure, whereas the abscissa is the corresponding central pressure of the best-track data. "A" denotes the central pressure at 24 forecast hours. "B" denotes that at 72 forecast hours. Three stages are defined as follows: (a) and (b): the intense stage, in which the observed typhoon records a 10 hPa decrease; (c) and (d): the steady stage, showing between a –10 hPa and 10 hPa decrease; (e) and (f): the decay stage, showing a 10 hPa increase. (a), (c), and (e) are according to the 20-km mesh AGCM. (b), (d), and (f) are according to the GSM.

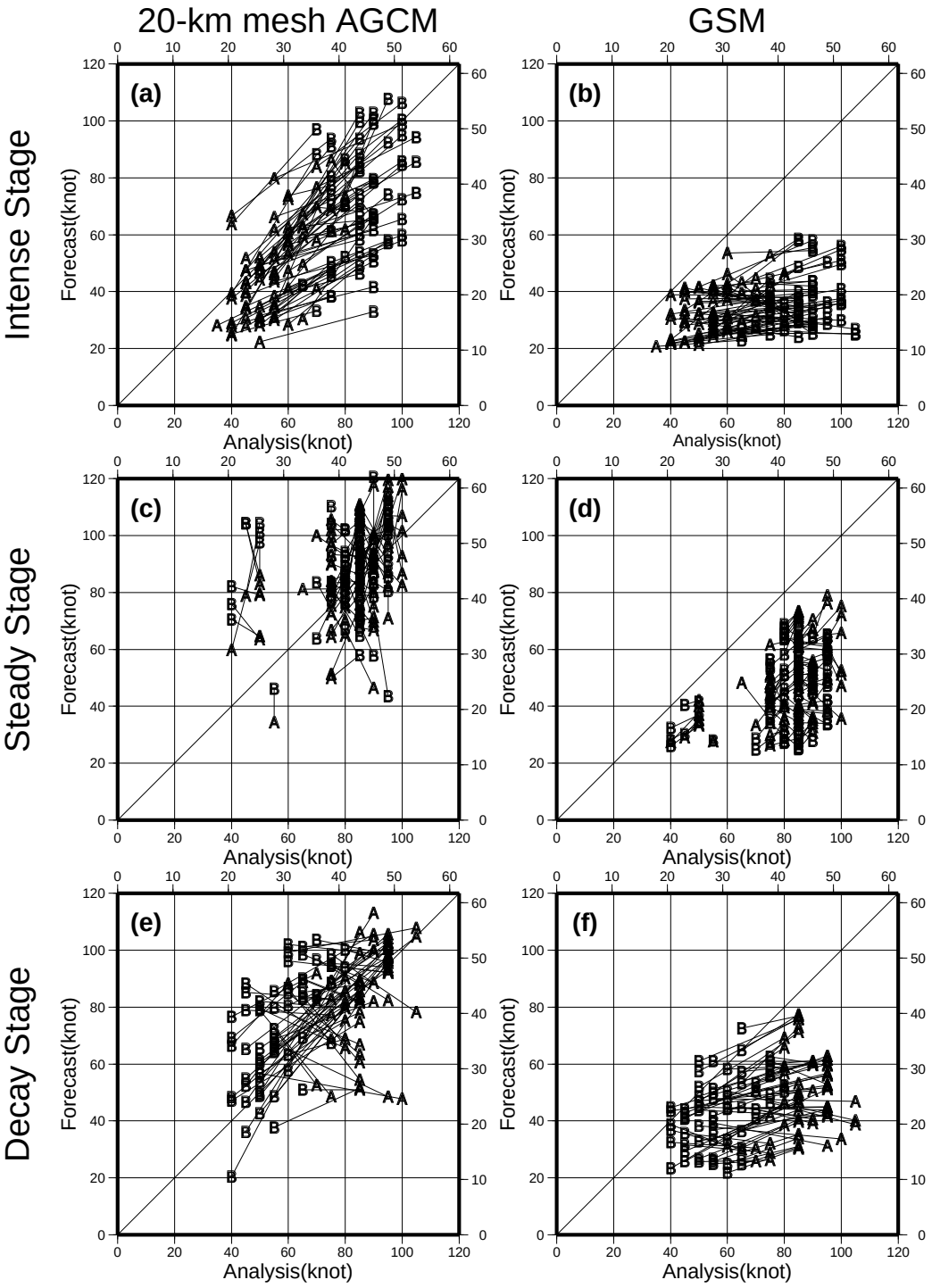

Figure 2.18: Same as Figure 2.17 but for the maximum wind velocity. The unit is the knot (ms^{-1} in top and right axises). The three stages are defined as follows: (a) and (b): the intense stage, in which the analyzed typhoon maximum wind velocity records a 10-knot increase; (c) and (d): the steady stage, showing between a –10-knot and a 10-knot increase; (e) and (f): the decay stage, showing a 10-knot decrease.

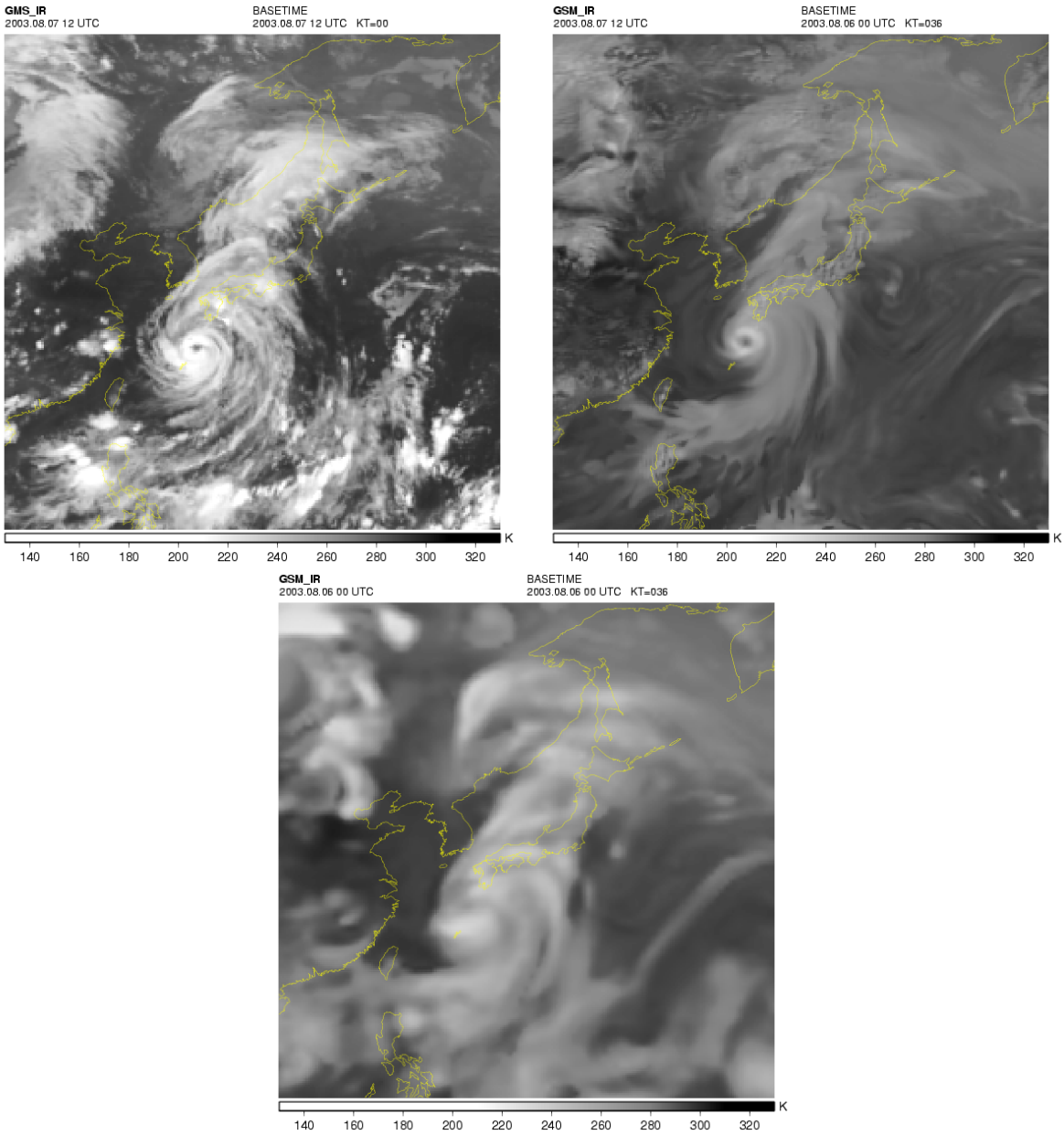

Figure 2.19: Comparison of infrared images. Top left: image by the GOES-9. Top right: image by the 20-km mesh AGCM. Bottom: image by the GSM. The typhoon of the image is the T0310. The date is 00 UTC August 06, 2003. The simulated forecast hour is 36.

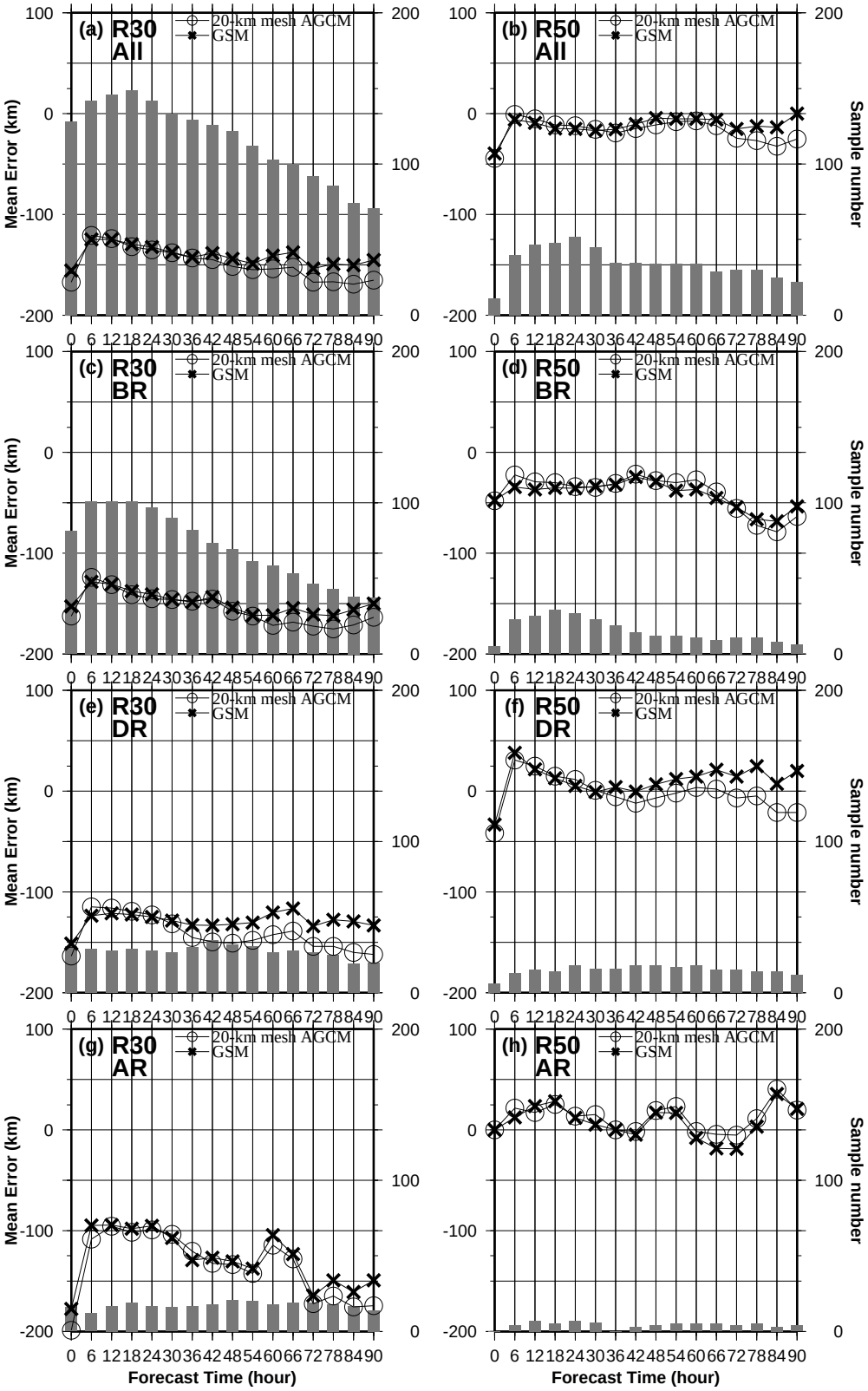

Figure 2.20: Mean errors of (a) R30 and (b) R50. (c) and (d) are the same as (a) and (b) but before the recurvature; (e) and (f) are during the recurvature; (g) and (h) are after the recurvature. The legends are the same as for Figure 2.9. The abscissa shows the forecast hour. The ordinate shows the mean error [km].

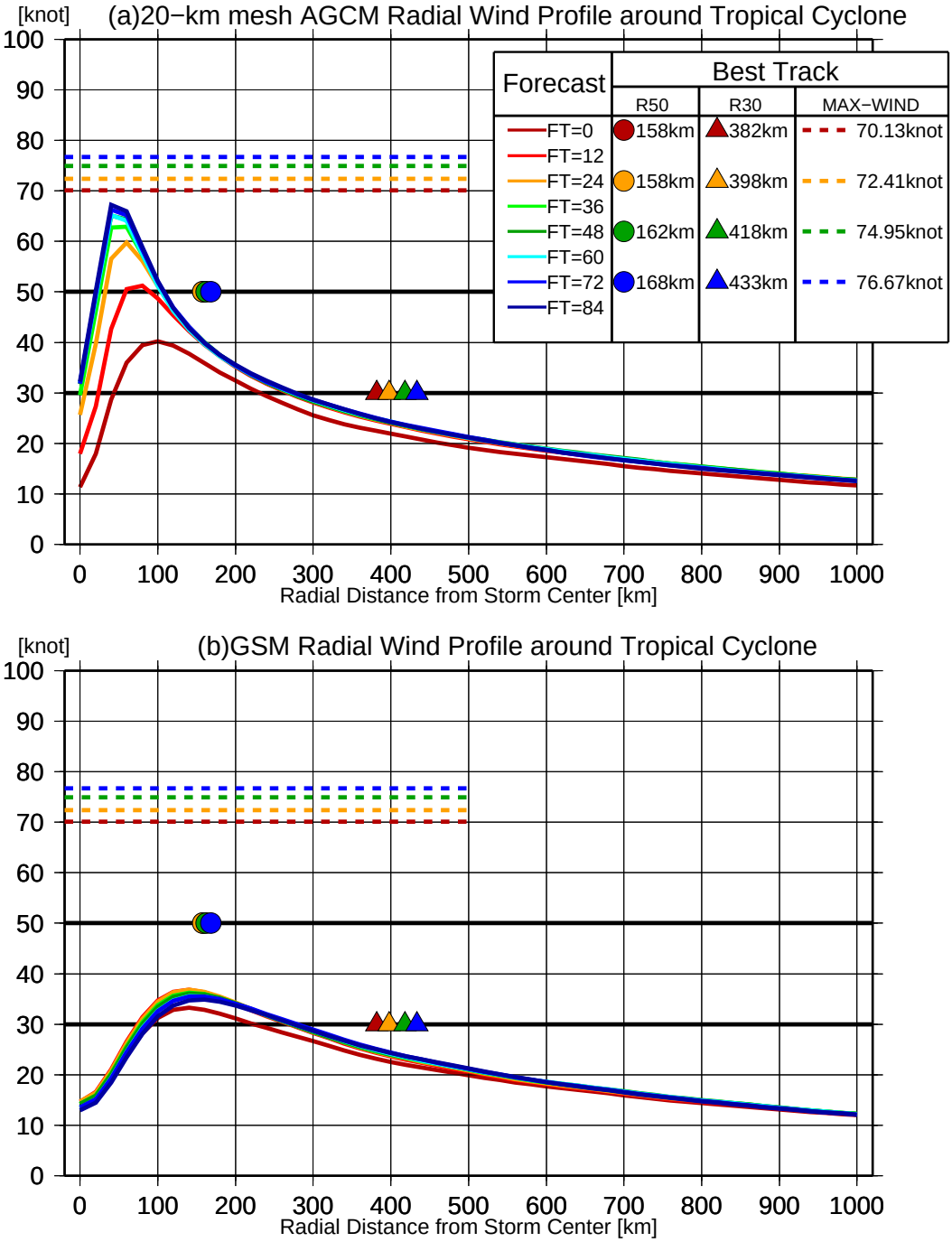

Figure 2.21: Mean wind profile for each forecast time. The abscissa shows the distance from the storm center. The ordinate shows the averaged wind velocity [knot]. The colored solid lines show model results. (a) is by the 20-km mesh AGCM, and (b) is by the GSM. The circle (triangle) plots show the best-track 30 (50) knot radius, which were averaged by the corresponding forecast time. The colored broken lines show the maximum wind velocity by the best-track. (radius is unknown)

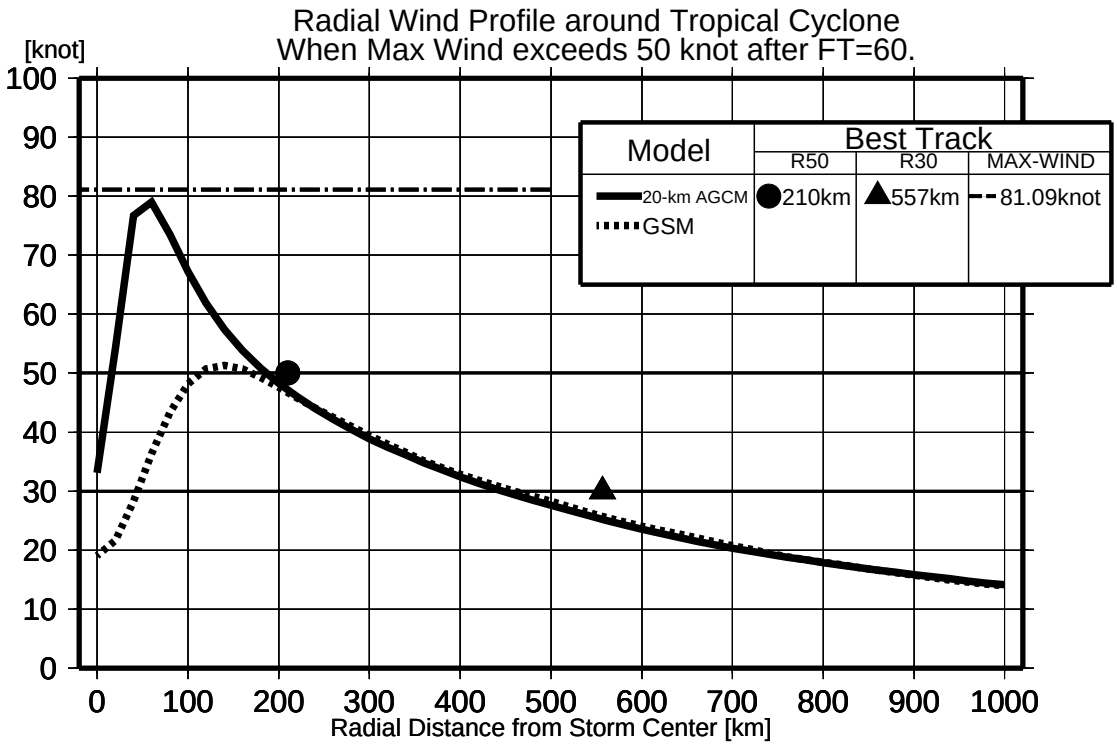

Figure 2.22: Mean wind profile of storms whose wind velocity is more than 50knot after 60 forecast hours. The abscissa shows the distance from the storm center. The ordinate shows the averaged wind velocity [knot]. The solid line shows by the 20-km mesh AGCM. The dotted line shows by the GSM. The circle (triangle) plot shows the best-track 30 (50) knot radius, which was averaged by the corresponding time. The long broken line shows the maximum wind velocity by the best-track. (radius is unknown)

Chapter 3

Effect of model resolution on tropical cyclone climate projections

While past studies have conducted climate projections using state-of-the-art models (Knutson et al., 2010), one issue that has yet to be clearly addressed is the effect of model resolution on the climatological features of projected TCs. This lack of information reflects the fact that high-resolution global model projections remain extremely expensive; consequently, most climate runs are performed with a relatively coarse resolution (e.g., 100–200-km mesh). This chapter reveals resolution-related differences in the projected features of TC climatology (e.g., TC intensity, temporal variations in TC genesis number, and the spatial pattern of TC genesis frequency (TGF)) using four resolutions, ranging from TL95 (180-km mesh) to TL959 (20-km mesh). Section 3.1 presents model descriptions, analysis methodology, and observations used in this study. Section 3.2 provides the results, and Section 3.3 summarizes the main conclusions. Details are also available in Murakami and Sugi (2010).

3.1 Methodology

3.1.1 Model descriptions

Table 3.1 lists the models considered in this study. Models (a)–(d) are the MRI/JMA-AGCMs, one of which is the same model as that used in Oouchi et al. (2006), but with model resolutions of (a) TL959 (20-km mesh), (b) TL319 (60-km mesh), (c) TL159 (120-km mesh), and (d) TL95 (180-km mesh).

Details of the model descriptions are available in Section 2.1. As reported in Mizuta et al. (2006), the climate model also applied several sets of adjustments for the TL959 projections as described below.

1. Evaporation effect is reduced by 10% in the TL959 model compared with other coarser models.
2. Assumed sub-grid variance of water vapor is set to be 10% smaller in the cloud scheme in the TL959 model than that used in other coarser models.
3. The amount of detrainment of cloud water at the top of the cumulus convection, as well as transformation speed from cloud water to precipitation in the cloud scheme, is reduced in the TL959 model.
4. The vertical transport of horizontal momentum in the convection scheme is reduced by 60%, resulting in more realistic organization of tropical cyclones.
5. The surface roughness length over the ocean is set larger in order to enhance thermal interaction between sea surface and boundary layer.
6. The gravity wave drag coefficient for short waves is increased in order to control excessive developments of extratropical cyclones.

Among the above adjustments, the reduction of vertical transport of horizontal momentum (No. 4 in the list) appears to affect directly tropical cyclone structure. This treatment was applied because a convective-scale pressure gradient force was not included in the convection scheme, causing excess of momentum transport and underestimate of tropical cyclone intensity. Since this adjustment assumes independent of resolution, it may be justified to apply it to other coarser resolutions. Therefore, this study applies the reduction of momentum effect to all resolutions. Other adjustments are only applied to

the TL959 model. In other words, this study uses the same physical processes and adjustment parameters for TL95, TL159, and TL319 projections; however, all adjustments were applied for TL959 projections, indicating TL959 has effects of both high resolution and parameter adjustments when compared with other resolutions.

3.1.2 Observations

The Japanese 25-year Re-Analysis (JRA-25) dataset (Onogi et al., 2007) was used for a test case employing the TC direct detection method described in Section 3.1.4 and latter for GPI analysis in Section 4.1.2. The JRA-25 reanalysis system was constructed based on the former global operational forecast and assimilation system at JMA. The system consists of a three-dimensional variational data assimilation (3DVAR) and a spectral forecast model with a resolution of T106L40 (triangular truncation at wave number 106 in the horizontal and 40 vertical layers). The data available period is from 1979 to 2004. One of the advantages of the JRA-25 is that it adopted TC retrieved (TCR) data in the assimilation process (Hatsushika et al., 2006). The TCR data provide an artificial three-dimensional TC structure constructed using information from the best-track data, such as position, motion, maximum surface winds, and the radii of 30- and 50-knot wind speeds. The TCR was then treated as observational data in the assimilation process. This approach yields both realistic environmental flows around a TC and TC structure.

The global TC dataset, obtained from the Web site of Unisys Corporation (Unisys, 2010), was used to evaluate present-day TC projections. The dataset consists of best-track data compiled by the National Hurricane Center (NHC) and Joint Typhoon Warning Center (JTWC), and contains historical TC information regarding the center location, intensity (maximum 1-minute surface wind speed), and sea level pressure at 6-hourly intervals from 1851 to 2009. This study uses only the TCs with tropical storm intensity or stronger (i.e., TCs that possess 1-min sustained surface wind of 35 knot or greater).

3.1.3 Prescribed external boundary forcings

Each resolution was employed for a pair of integrations: a present-day projection (1979–2003) with prescribed observed SST and sea ice concentrations (SICs) and a global-warming projection (2075–2099) with prescribed future SST based on an ensemble mean of 18 IPCC-AR4 (IPCC, 2007) models projected under the IPCC SRES A1B. The multi-year climate projections were performed based on the so-called time slice experiments (Bengtsson et al., 1996), in which SST, SIC, and greenhouse gases are given as external forcings.

Figure 3.1 shows how to prescribe SST and SIC in this study. Details are also available in Mizuta et al. (2008). For the present-day simulation, observed SST and SIC were prescribed, with the monthly-mean data being interpolated to daily values. For the future projection, future SST and SIC were created using the ensemble mean of 18 IPCC-AR4 models as listed in Table 3.2. First, observed SST and SIC were decomposed into a trend (PDTR) component and an interannual variation (PDIV) for the 25 years from 1979 to 2003. Second, the same decomposition was applied to the ensemble mean of the AR4 models, thereby obtaining the future trend (GWTR) and interannual variation (GWIV) for the 25 years from 2075 to 2099. The average values of SST and SIC for each period were also computed, yielding the future change (GWDT). Finally, future forcing conditions were reconstructed as a recomposition of GWDT, GWTR, and PDIV. Here, the amplitude and phase of the interannual variations are assumed to be conserved in the future setting. This study does not use the raw time series of the multi-model ensemble mean because the averaging smoothes out year-to-year variability of SST and excludes ENSO. Figure 3.2 shows climatological mean of prescribed SST for (a) the present-day, (b) the future projection, and (c) the future changes. The future increases in SST are characterized as (i) relatively larger in the Northern Hemisphere than the Southern Hemisphere and (ii) relatively larger in the Arabian Sea, the tropical central Pacific, the subtropics of the

central Pacific, and the Inter-Tropical Convergence Zone (ITCZ) of the eastern North Atlantic than other regions.

The annual concentrations of greenhouse gases (CO_2, CH_4, and N_2O) were derived from observed values for the present-day projection, and from the A1B IPCC emission scenario (IPCC, 2007) for the future projection. For aerosols, the climatological monthly mean values were calculated from the global chemical transport model (Tanaka et al., 2003). The same aerosols were also used for the future projection.

The projections performed in this study are expected to be more reliable than those reported by Oouchi et al. (2006) because this study employs more realistic features in the experimental design. For example, the future projection is prescribed by an 18-model ensemble mean of future SST change, whereas Oouchi et al. (2006) used SST projected by a single model; in addition, the model simulations cover a 25-year period and include interannual variations in the SST forcing field, whereas Oouchi et al. (2006) covered 10-year periods using climatological mean SST.

3.1.4 TC detection method and definition of TGF

Model-generated TCs were detected directly using globally uniform criteria similar to those reported in Oouchi et al. (2006), as follows.

1. The magnitude of the maximum relative vorticity at 850 hPa (ζ_{850}) exceeds a threshold that depends on the resolution (see Table 3.1).

2. The temperature structure aloft has a marked warm core, such that the sum of the temperature deviations at the 300, 500, and 700 hPa vertical levels exceeds 1.0 K (0.7 K for JRA-25). The temperature deviation for each level was computed

by subtracting the maximum temperature from the mean temperature over the surrounding $10^\circ \times 10^\circ$ grid box.

3. The maximum wind speed at the 850 hPa vertical level is higher than that at 300 hPa (to exclude extra-tropical cyclones).

4. The genesis position, defined as the first position at which conditions (1)–(3) are satisfied, is over the ocean.

5. The duration exceeds 36 hours. To prevent double TC counts arising from detection and termination during a single time step, termination during a single time step is allowed.

The resolution-dependent value of ζ_{850} ensures the observed global-mean annual TC number (i.e., 84.8 for the period 1979–2003) which is attained in the present-day simulation, for each resolution. To show the sensitivity of the value of the criterion ζ_{850} to detected TC number, Figure 3.3 shows the accumulated global TC number for each value of ζ_{850} applied to the TL959 present-day simulation. Although the TL959 model underestimates observed intensity, the shape of curves are reasonably projected.

The TC genesis locations were counted for each $5^\circ \times 5^\circ$ grid area over the global domain. The total counts were defined as Tropical cyclone Genesis Frequency (TGF) in this study. Figure 3.4 shows the TGF obtained from the best-track data, along with the result obtained by applying the above detection method to JRA-25 data. The detection method performs reasonably well in identifying observed TCs. The Taylor skill score I (i.e., the combination of the error and spatial correlation; Taylor, 2001) for evaluating the spatial distributions of TGF shows a high value of 0.96 (Table 3.1). The robustness of the present results, regardless of the defined grid box size, was experimentally confirmed using different grid box sizes (e.g., $2.5^\circ \times 2.5^\circ$ or $10^\circ \times 10^\circ$; data not shown). A TC detection method using the objective resolution-dependent criteria proposed by Walsh et al. (2007)

were also experimentally applied, resulting in robust conclusions (data not shown). Nine ocean basins were considered for verifications: global (GL), Northern Hemisphere (NH), Southern Hemisphere (SH), North Indian Ocean (NIO), Western North Pacific (WNP), Eastern North Pacific (ENP), North Atlantic (NA), South Indian Ocean (SIO), and South Pacific Ocean (SPO) (see Figure 3.4 for region boundaries).

3.2 Results and discussion

3.2.1 Effect of model resolution on projected TC intensity

Figure 3.5 shows the relationship between maximum wind velocity (MWV) and sea level pressure (SLP) for all detected TCs. Overall, TC intensity shows a dependency on horizontal resolution, although all resolutions more or less reproduce the observed relationship. Because JRA-25 (Fig. 3.5b) uses TL159 as the resolution in its assimilation process, the MWV-SLP relationship is similar to that obtained by TL159 (Fig. 3.5e). The regression lines for all resolutions are located below the green dashed regression line obtained for the best-track data. This discrepancy is mainly due to the differences in the definition of MWS; i.e., the best-track applies 1-minute sustained MWS (see Section 3.1.2), whereas the model applies time-step mean MWS (e.g., 10 min for TL959). However, the modeled relationships appear to be in good agreement with the observed regression line proposed by Atkinson and Holiday (1977; pink curves in Fig. 3.5). It is also evident that TL959 performs best in reproducing the observed intense TCs, although it still underestimates extremely intense TCs, such as those with MWV $> 60\ ms^{-1}$ and SLP < 920 hPa.

For the future projections, all resolutions except for TL95 show an increase in mean TC intensity. However, in terms of the probability density of life-cycle maximum surface wind speed (Fig. 3.6), resolutions of TL319 and finer show a significant increase in the range of

intense TCs, whereas resolutions of TL159 and coarser show no such significant increase. Previous studies that used a global model with a horizontal resolution of T106 (roughly equivalent to TL159 in the present study) reported no coherent changes in intense TCs in global warming experiments (Bengtsson et al., 1996; Sugi et al., 2002; Yoshimura et al., 2006; Gualdi et al., 2008). Moreover, Bengtsson et al. (2007) compared a global model with resolutions of T63 (192 $\times$ 96 grid) and T213 (640 $\times$ 320 grid), which are roughly equivalent to TL95 and TL319 in the present study, respectively. The authors reported that T213 showed a future increase in the frequency of intense TCs, whereas T63 did not. The authors also performed an additional experiment using a T319 (about 40-km mesh) model, which showed a clear increase in intense TCs in the future projection. Zhao et al. (2009) reported a significant increase in relatively intense TCs using a global model with 60-km grid spacing, which is equivalent to TL319 in the present study. Overall, 60-km mesh may be a critical resolution in projecting future increases in intense TCs. The view is supported by a recent report by Knutson et al. (2010). Although the physical reason for this critical resolution remains unknown, the authors also reported that high-resolution models commonly showed increased rainfall in the inner-core region, within 100 km of the TC center. Figure 3.7 shows TC composite structures projected by the TL959 model when TCs are at their maximum surface-wind velocity. For both the precipitation and surface-wind velocity fields, marked increases appear in the inner-core region. These results indicate that the accurate simulation of inner-core structure (e.g., eye walls) may be a key factor in simulating future increases in the frequency of intense TCs.

3.2.2 Effect of resolution on projected TC genesis number

Table 3.3 shows the percentage of model biases in annual mean TC genesis number for different basins. It must be noted that the basin-scale TC number is more or less independent of model resolution; e.g., all resolutions commonly underestimate TC numbers in NH, WNP and NA, and overestimate TC numbers in SH, ENP, and SIO. Overall,

it appears that the inter-basin balance in TC genesis number is not determined by the resolution, but by other parameters such as model physics. However, a comparison of inter-annual variations with observations reveals that finer resolutions show relatively higher skills (Table 3.4); e.g., TL959 shows statistically high correlation coefficients for four of the basins. The resolution dependency is clearer in the case of seasonal variations (Table 3.5)[1].

Table 3.6 lists the percentage change in annual mean TC genesis number compared with the present-day projection. All resolutions except for TL95 share similarities in future changes; e.g., significant reductions in GL, NH, SH, WNP, ENP, SIO, and SPO, and generally an increase in NA. Although the relatively fine resolutions (TL959 and TL319) show similar future changes at hemispheric scales (GL, NH, and SH), they are inconsistent in several sub-basins in terms of both the sign and magnitude of change.

3.2.3 Effect of resolution on the projected spatial distributions of TC genesis frequency

Figure 3.8a–d shows the spatial distributions of model biases in TGF for the present-day simulation for each resolution. All the resolutions show similarities in their biases: underestimates in the Bay of Bengal, WNP, coastal ENP, mid-latitudes of NA, and central SIO, and overestimates in the Arabian Sea, South China Sea (SCS), central ENP, Inter-Tropical Convergence Zone (ITCZ) in NA between 10 °N and 20 °N, African coastal SIO, and northeast Australia. When verified against observations, the Taylor skill score I (Table 3.1) shows similar values for the different resolutions. Table 3.7 lists the inter-resolution correlations for the spatial patterns of bias for the global domain, revealing correlation coefficients greater than 0.6, indicating that the model biases are common to

[1]The correlation coefficients in Table 3.5 were computed by comparing climatological monthly mean of observed and modeled TC numbers for the 25 years.

the various resolutions.

Figure 3.8e–h shows similar future changes in TGF among the different resolutions, with general increases in TGF for the Arabian Sea, Bay of Bengal, southeastern quadrant of WNP, and the ITCZ in NA; decreases are seen in SCS, central SIO, and northeast Australia. Table 3.8 indicates that each resolution, except for TL95, shows a positive correlation with the other resolutions in terms of future change in TGF, although the correlation coefficients are smaller than those for bias (Table 3.7). Moreover, similar resolutions show relatively strong correlations (e.g., TL959 and TL319, TL319 and TL159, and TL159 and TL95) compared with other resolution combinations, indicating that similar resolutions tend to show comparable spatial changes in TGF. Overall, future changes in TGF are independent of resolution; instead, they appear to be sensitive to model physics and the spatial pattern of prescribed SST (Sugi et al., 2009).

3.3 Summary

This chapter investigated the effect of model resolution on projected TC climatology, temporal variations in TC genesis, and future changes using four different resolutions, ranging from TL95 (180-km mesh) to TL959 (20-km mesh). The finest resolution (TL959) showed the highest skills in terms of mean TC intensity, and inter-annual and seasonal variations in TC genesis number, indicating that a high resolution is generally desirable for accurate projections of TC intensity and temporal variations in TC genesis. However, TL959 contains parameter tunings in the physical processes, indicating both effects of high-resolution and turning. Even if TL959 is removed from the comparisons, TL319 still shows the highest skills among coarser models, indicating high resolution is still preferable.

Regarding future changes in TC intensity, resolutions of TL319 (60-km mesh) and

finer projected a significant future increase in the frequency of intense TCs; this significant increase was not projected by resolutions coarser than TL319. Comparisons with other studies that employed global models reveal that TL319 may be a critical resolution in terms of projecting future increases in the frequency of intense TCs. Biases in basin-scale annual mean TC genesis number and the spatial distributions of TC genesis frequency (TGF) were not critically dependent on resolution, indicating the influence of other parameters such as model physics. Moreover, the nature of future changes is similar among the various resolutions except for TL95, indicating that future changes in climatological mean features projected by a high-resolution model could also be obtained using coarser resolutions.

In summary, the use of a higher-resolution model is generally desirable for accurate climate projections, although in the present study, future changes and present-day climatology in TGF showed little dependence on resolution, except for TL95. This finding indicates the potential validity of using a model with relatively coarse resolution. For example, ensemble realizations may be useful in minimizing uncertainties in future projections that are difficult to perform with a higher-resolution model due to the large demand on computational resources. A model with coarse resolution may also be useful in a model-development process in improving the TGF climatology for better climate projections that would later be performed using a higher-resolution model.

Table 3.1: Main features of the models considered in this study, including the threshold value of the relative vorticity criterion (ζ_{850}) and the Taylor skill score I of tropical cyclone genesis frequency (TGF) against best-track data.

Model/Reanalysis name	Abbreviation	Resolution (km)	ζ_{850} ($\times 10^{-5} s^{-1}$)	Taylor skill score I
(a) JMA/MRI 20km	TL959	20 × 20	31.28	0.87
(b) JMA/MRI 60km	TL319	60 × 60	11.43	0.82
(c) JMA/MRI 120km	TL159	120 × 120	8.33	0.87
(d) JMA/MRI 180km	TL95	180 × 180	7.68	0.80
(e) Japanese Re-Analysis	JRA-25	140 × 140	0.62	0.96

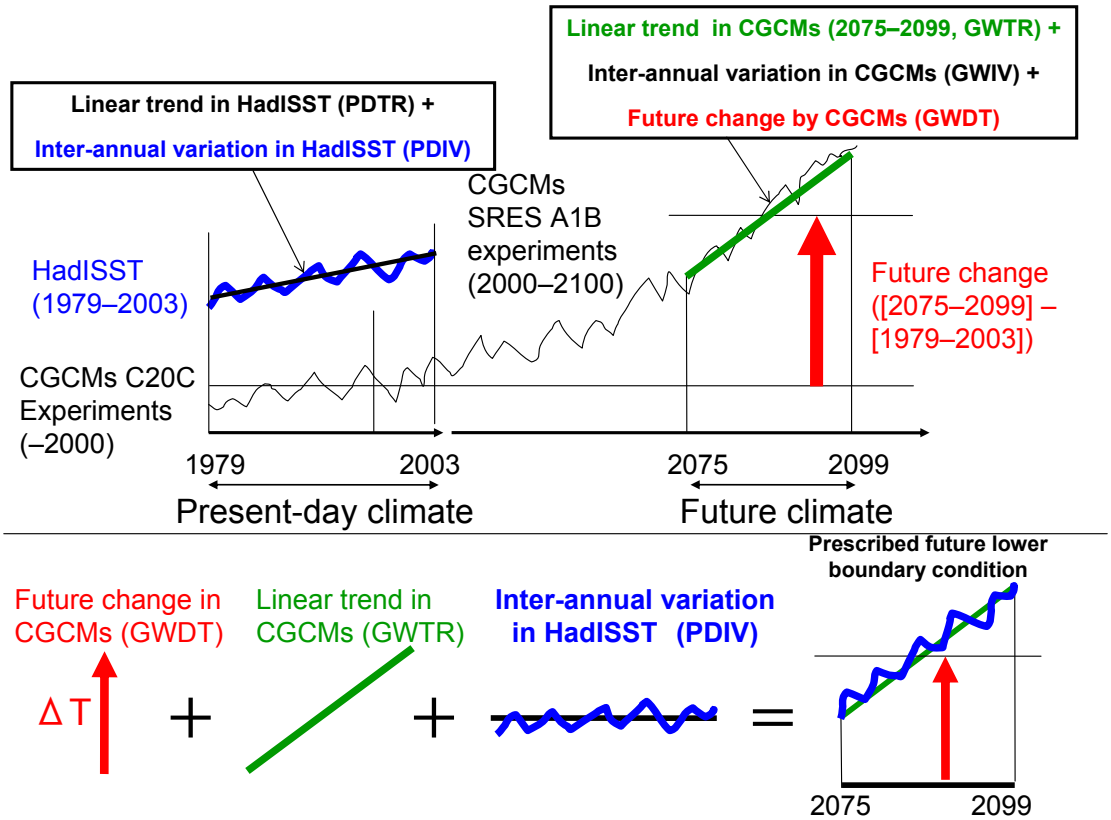

Figure 3.1: Schematic diagram of prescribed lower boundary conditions for the future simulation. The abbreviations are as follows: SST (Sea Surface Temperature), HadISST (Hadley Center observational SST), PDTR (trend in the present-day SST), PDIV (inter-annual variation in the present-day SST), GWTR (trend in the ensemble mean of future SSTs), GWIV (inter-annual variation in the ensemble mean of future SSTs), GWDT (averaged future change in the ensemble mean of SSTs), CGCM (Coupled General Circulation Model), and C20C (Climate of the Twentieth Century).

Table 3.2: CMIP3 models used for future prescribed lower boundary conditions

CMIP3 I.D.	Model Name	Institute
BCCR BCM2 0	The Bergen Climate Model version 2	Bjerknes Centre for Climate Research, Norway
CGCM3.1 T47 CGCM3.1 T63	The third version of the Canadian Centre for Climate Modelling and Analysis (CCCma) Coupled Global Climate Model	Canadian Centre for Climate Modeling & Analysis, Canada
CNRM CM3	The Centre National de Recherches Meteorologiques Coupled global climate Model, version 3	Météo-France/Centre National de Recherches Météorologiques, France
CSIRO Mk3.0	The CSIRO Mark 3 climate model	CSIRO Atmospheric Research, Australia
GFDL CM2.0 GFDL CM2.1	The Geophysical Fluid Dynamics Laboratory Coupled Model version 2.0 (2.1)	Geophysical Fluid Dynamics Laboratory/NOAA/U.S. Dept. of Commerce, United States
GISS AOM	The NASA/GISS Atmosphere-Ocean Model	Goddard Institute for Space Studies, National Aeronautics and Space Administration, United States
INM CM3.0	The Institute for Numerical Mathematics (INM) Coupled Model version 3.0	Institute for Numerical Mathematics, Russia
IPSL CM4	The ocean-atmosphere coupled model-LInstitut Pierre-Simon Laplace Coupled Model, version 4	Institut Pierre Simon Laplace, France
MIROC3.2 hires MIROC3.2 medres	The high (mid) resolution Model for Interdisciplinary Research on Climate version 3.2	Center for Climate System Research (University of Tokyo), National Institute for Environmental Studies, and Frontier Research Center for Global Change (JAMSTEC), Japan
MIUB ECHO-G	The Meteorological Institute of the University of Bonn Germany global climate model version ECHO-G	Meteorological Institute of the University of Bonn, Meteorological Research Institute of KMA, and Model and Data Group, Germany and Korea
MPI ECHAM5	The fifth-generation atmospheric general circulation model and the Max- Planck-Institute ocean model (ECHAM5/MPIOM)	Max Planck Institute for Meteorology, Germany
MRI CGCM2.3	The Meteorological Research Institute (MRI)-coupled atmospheric-ocean general circulation model version 2.3.2	Meteorological Research Institute, Japan
NCAR CCSM3.0	The Community Climate System Model version 3	National Center for Atmospheric Research, United States
UKMO HadCM3	The Met Office's Third Hadley Center Coupled Ocean-Atmosphere GCM	Hadley Centre for Climate Prediction and Research/Met Office, United Kingdom
UKMO HadGem1	The Hadley Center Global Environmental Model version 1	

Table 3.3: Model biases in annual mean TC genesis number for each basin. The unit is percentage change compared with observations. Blue (red) numbers indicate that the negative (positive) bias is statistically significant at the 95% level (two-sided Student's t-test).

	GL	NH	SH	NIO	WNP	ENP	NA	SIO	SPO
TL959	0.0	–10.0	22.5	–10.5	–40.5	55.2	–38.4	20.4	20.9
TL319	0.0	–2.9	6.3	12.3	–57.4	104.7	–45.6	7.5	–0.8
TL159	0.0	–5.9	13.3	23.7	–47.4	69.2	–35.7	12.3	11.0
TL95	0.0	–15.9	35.7	27.2	–35.8	32.9	–63.1	4.8	73.6

Table 3.4: Correlation coefficients for the inter-annual TC genesis number for each basin compared with observations. Red numbers indicate that the positive correlation coefficient is statistically significant at the 95% level (significance test for Pearson's product-moment correlation).

	GL	NH	SH	NIO	WNP	ENP	NA	SIO	SPO
TL959	0.28	0.11	0.53	0.14	0.60	–0.33	0.42	0.48	0.17
TL319	0.26	0.21	0.04	0.06	0.58	–0.22	0.56	0.18	–0.06
TL159	0.17	0.23	0.22	–0.04	0.44	–0.04	0.24	0.25	–0.13
TL95	0.31	0.36	0.30	0.03	0.33	–0.07	–0.01	–0.10	0.10

Table 3.5: As for Table 3.4, but for seasonal TC genesis number.

	GL	NH	SH	NIO	WNP	ENP	NA	SIO	SPO
TL959	0.82	0.93	0.99	0.91	0.86	0.83	0.99	0.95	0.98
TL319	0.69	0.87	0.98	0.89	0.91	0.54	0.99	0.96	0.96
TL159	0.56	0.80	0.98	0.66	0.91	0.39	0.97	0.98	0.96
TL95	0.16	0.20	0.82	0.35	–0.11	0.07	0.83	0.44	0.87

Table 3.6: As for Table 3.3, but for future changes in TC genesis number compared with the present-day projection.

	GL	NH	SH	NIO	WNP	ENP	NA	SIO	SPO
TL959	–15.8	–15.5	–16.4	–11.8	–26.8	–14.5	5.6	–4.8	–34.9
TL319	–18.8	–18.9	–18.5	18.0	–11.7	–30.5	4.2	–8.9	–33.7
TL159	–29.0	–21.5	–43.0	–2.8	–26.0	–24.7	–14.2	–32.7	–62.8
TL95	–1.2	8.6	–14.8	22.1	–18.5	17.3	56.7	–17.0	–14.3

Table 3.7: Inter-resolution correlation coefficients for biases of tropical cyclone genesis frequency (TGF). Red numbers indicate that the positive correlation coefficient is statistically significant at the 95% level (significance test for Pearson's product-moment correlation).

	TL959	TL319	TL159	TL95
TL959		0.80	0.74	0.63
TL319			0.87	0.61
TL159				0.63

Table 3.8: As for Table 3.7, but for future changes in TGF

	TL959	TL319	TL159	TL95
TL959		0.31	0.20	0.02
TL319			0.37	0.00
TL159				0.11

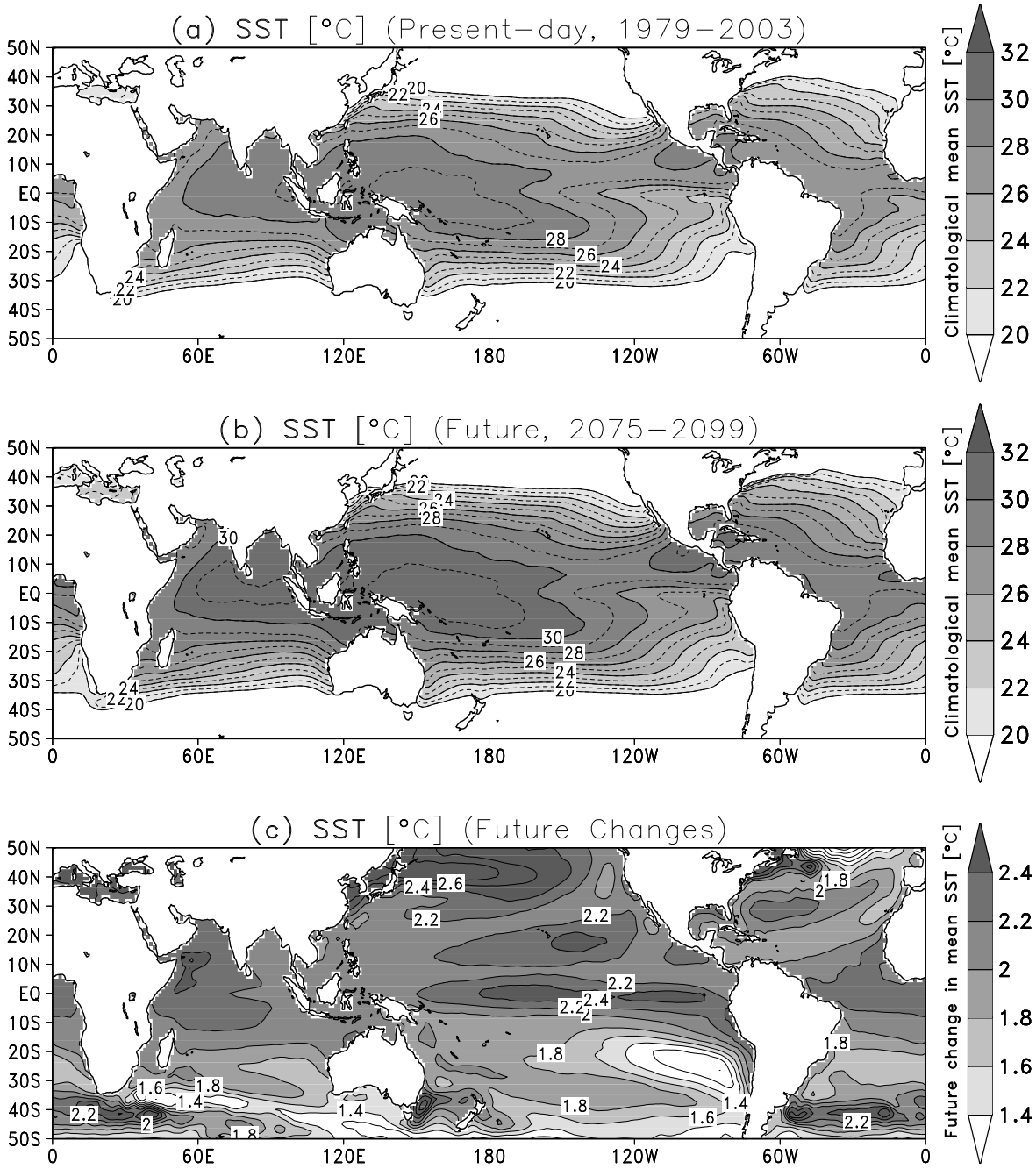

Figure 3.2: Climatological mean of prescribed SST [℃] for (a) the present-day run, (b) the future run, and (c) the future changes. The SSTs cooler than 20 ℃are filtered out in (a) and (b).

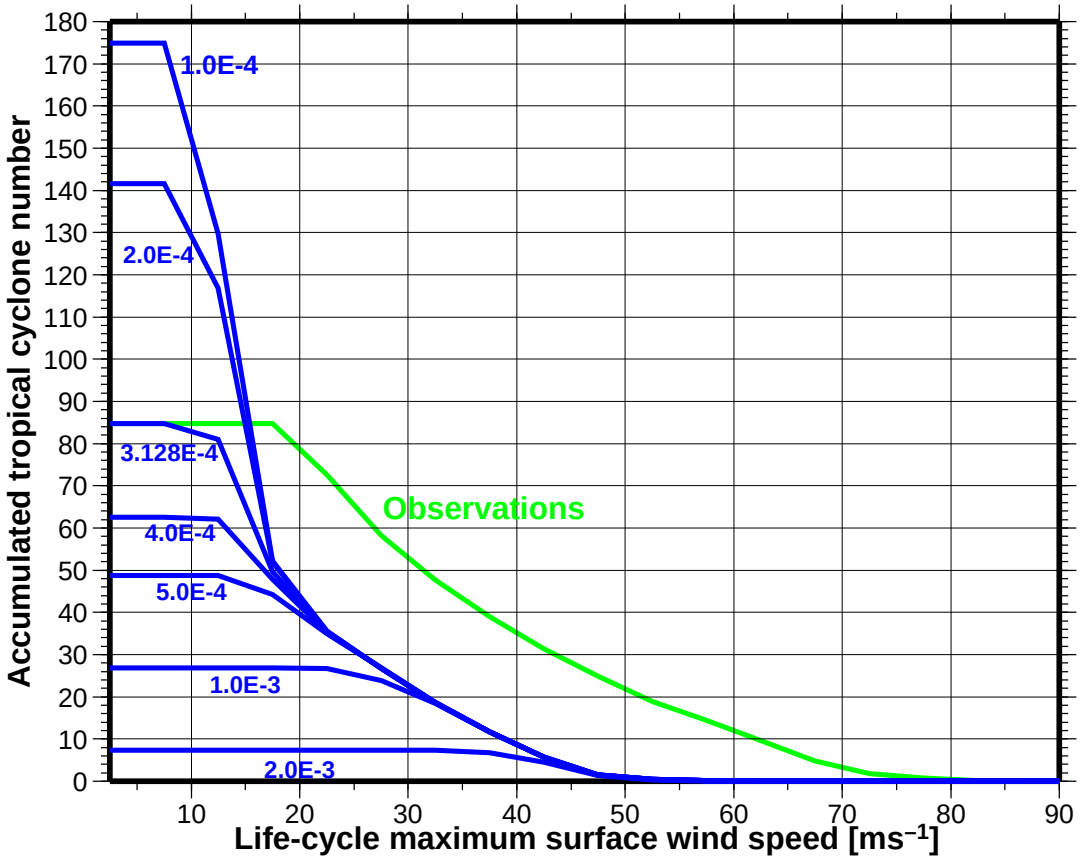

Figure 3.3: Accumulated number of detected tropical cyclones using different values of criterion ζ_{850} (blue numbers) applied to the TL959 present-day projection (blue lines). Green line shows the trend obtained from best-track data.

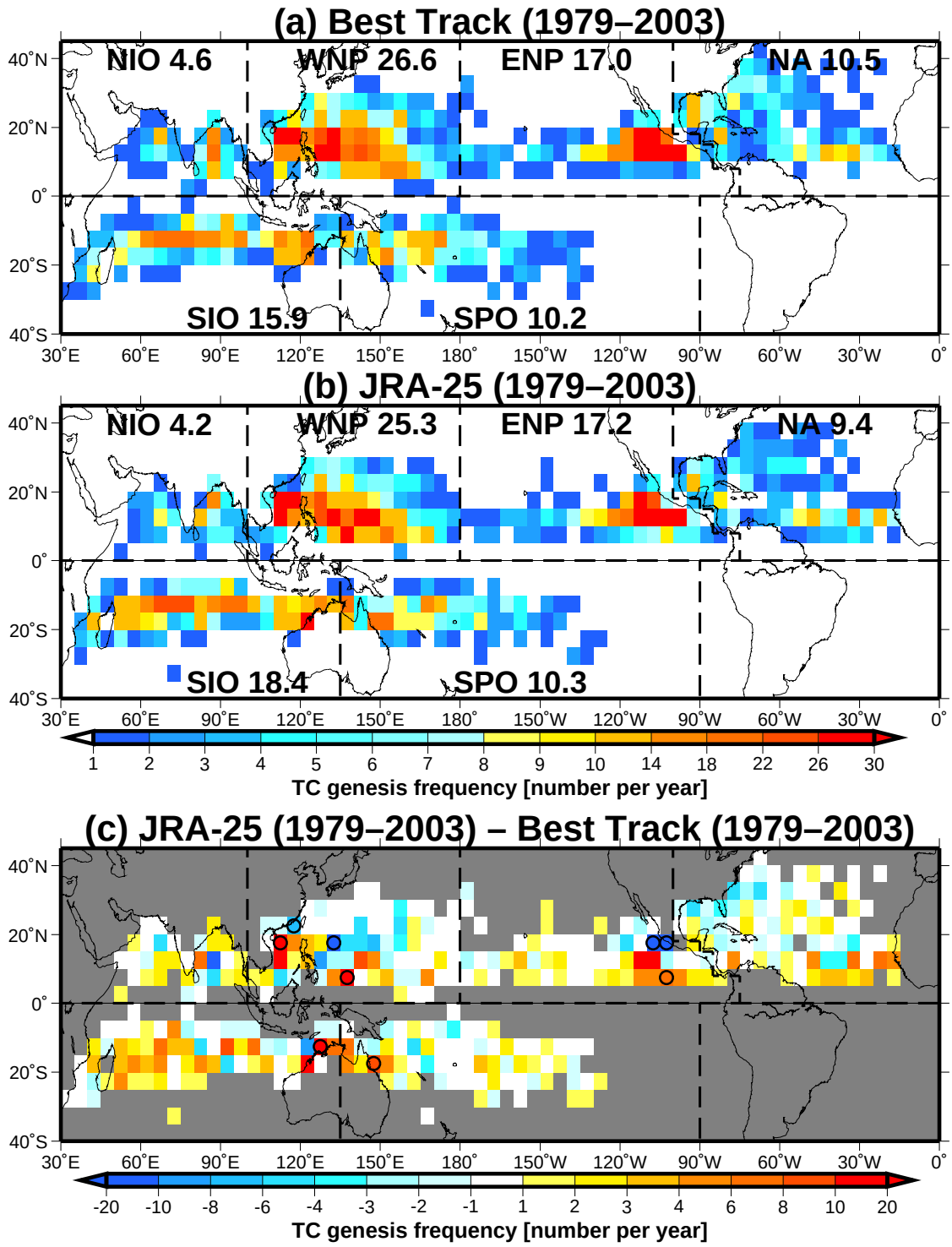

Figure 3.4: Tropical cyclone genesis frequency (TGF) by (a) best-track data, (b) JRA-25, and (c) bias. The numbers in (a) and (b) represent the annual mean TC genesis number for each basin. The small circles in (c) indicate that the bias is statistically significant at the 95% level (two-sided Student's t-test).

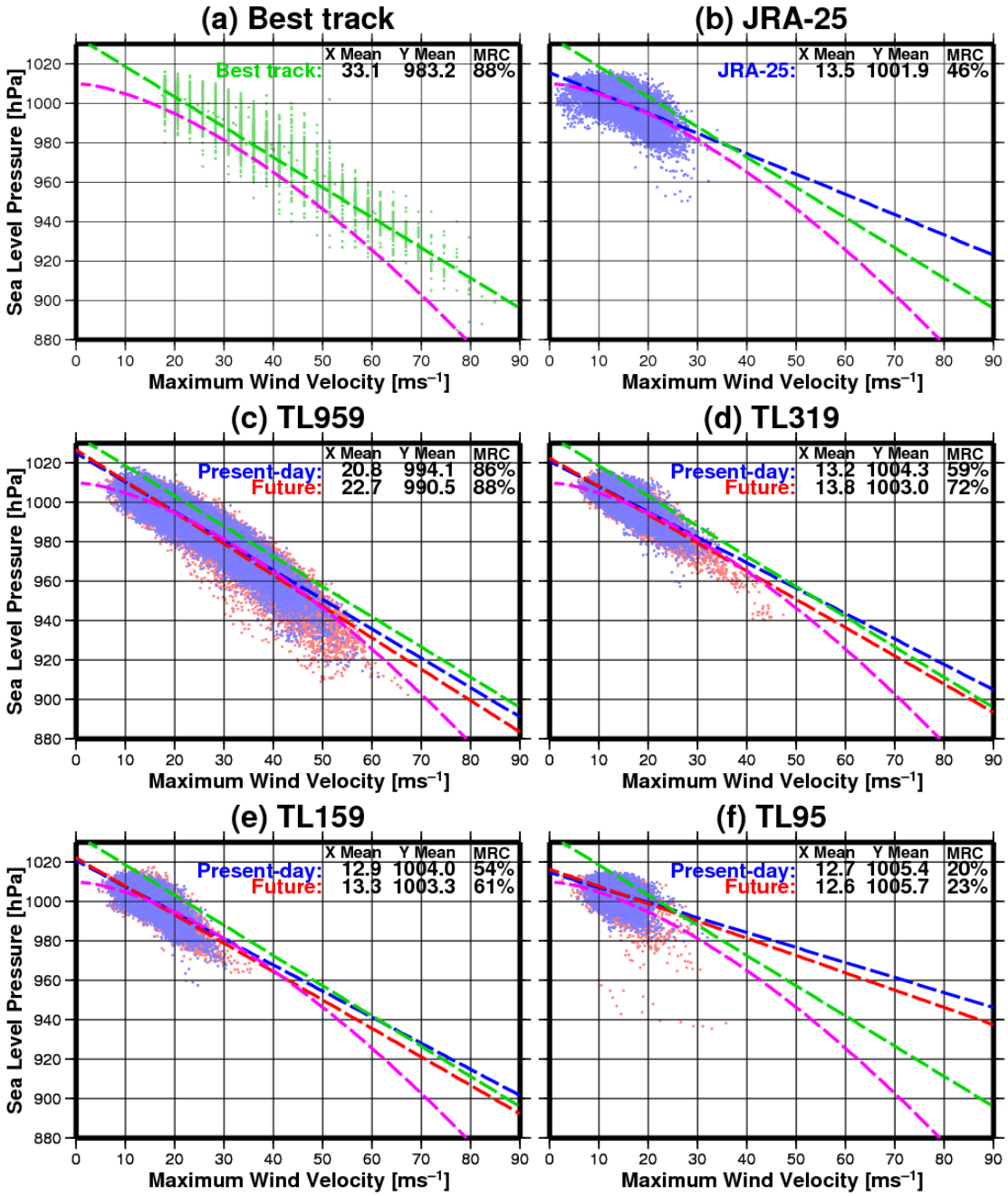

Figure 3.5: Maximum wind velocity (MWV, unit: ms^{-1}) versus sea level pressure (SLP, unit: hPa) for (a) best-track data, (b) JRA-25, (c) TL959, (d) TL319, (e) TL159, and (f) TL95. The green, blue, and red lines are linear regression lines for the best track, present-day, and future projection data, respectively. The pink curve is the observed regression line proposed by Atkinson and Holiday (1977). Also listed in each panel are the values of mean MWS, SLP, and the multiple regression coefficient (MRC).

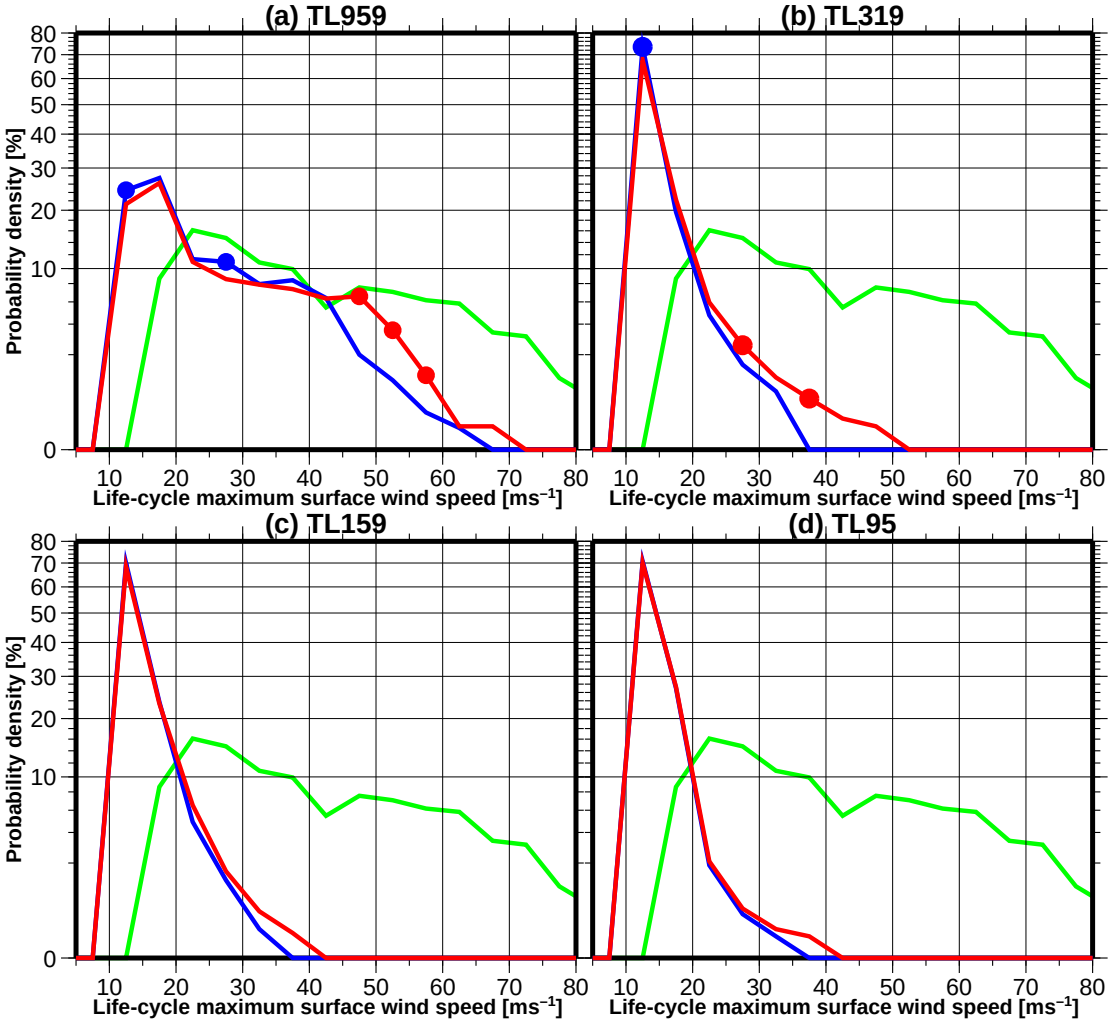

Figure 3.6: Probability density of life-cycle maximum surface wind speed $[ms^{-1}]$ for the global domain for observations (1979–2003, green lines), present-day projections (1979–2003, blue lines), and future projections (2075–2099, red lines) for resolutions of (a) TL959, (b) TL319, (c) TL159, and (d) TL95. The red (blue) circles indicate that the probability bin for the future projection is significantly higher (lower) than that for the present-day projection at the 95% level of significance (two-sided Student's t-test). Bin widths are 5 ms^{-1}.

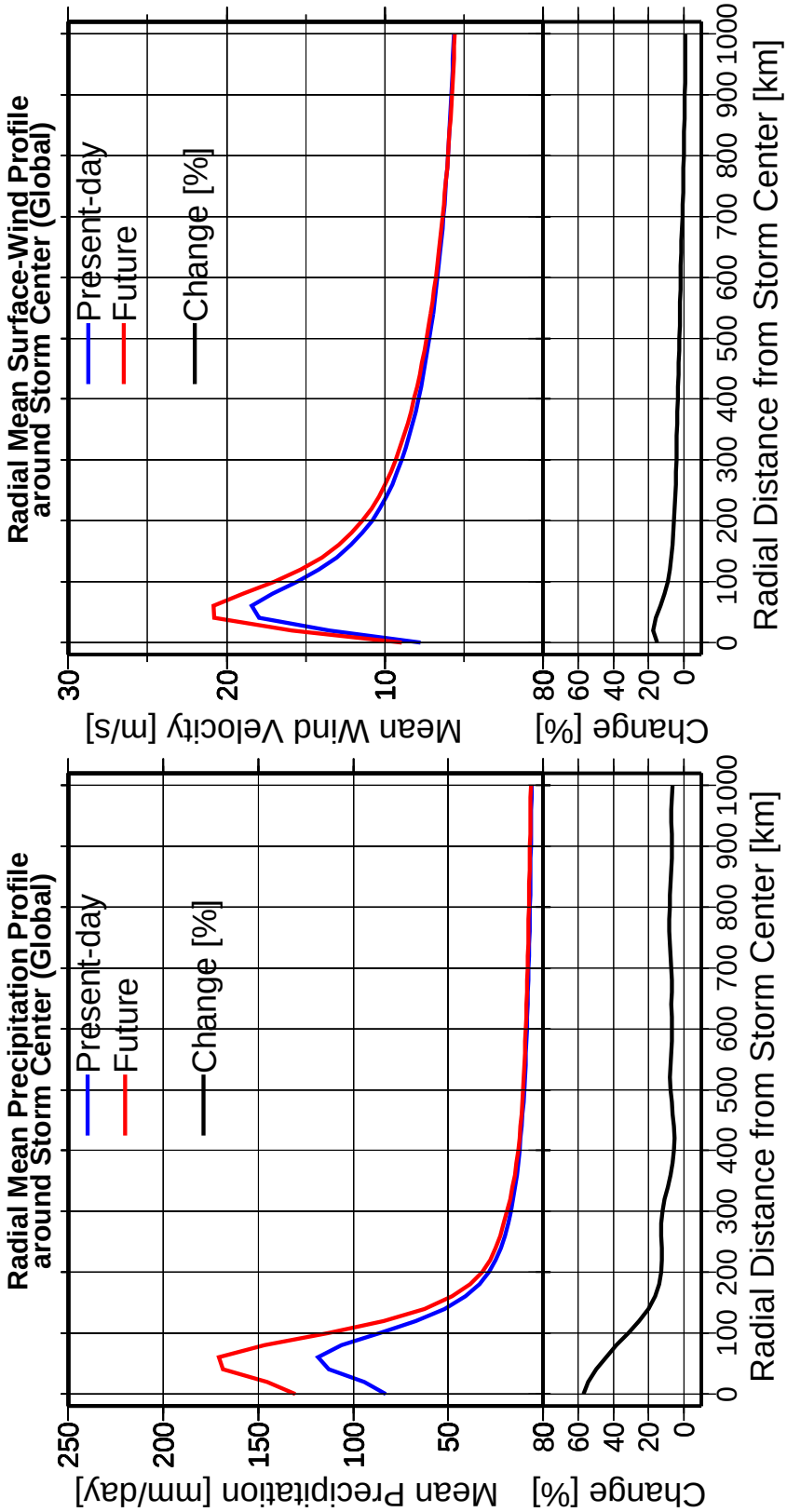

Figure 3.7: Azimuthal mean of (a) precipitation [mm/day] and (b) maximum surface wind [knot] for global TCs at their maximum intensity. The blue (red) line shows the present-day (global warming) simulation projected by TL959 (20-km mesh) MRI/JMA AGCM. The black line shows the ratio of future change [%]. Sampling number is 2,086 (1,667) for the present-day (future) projection.

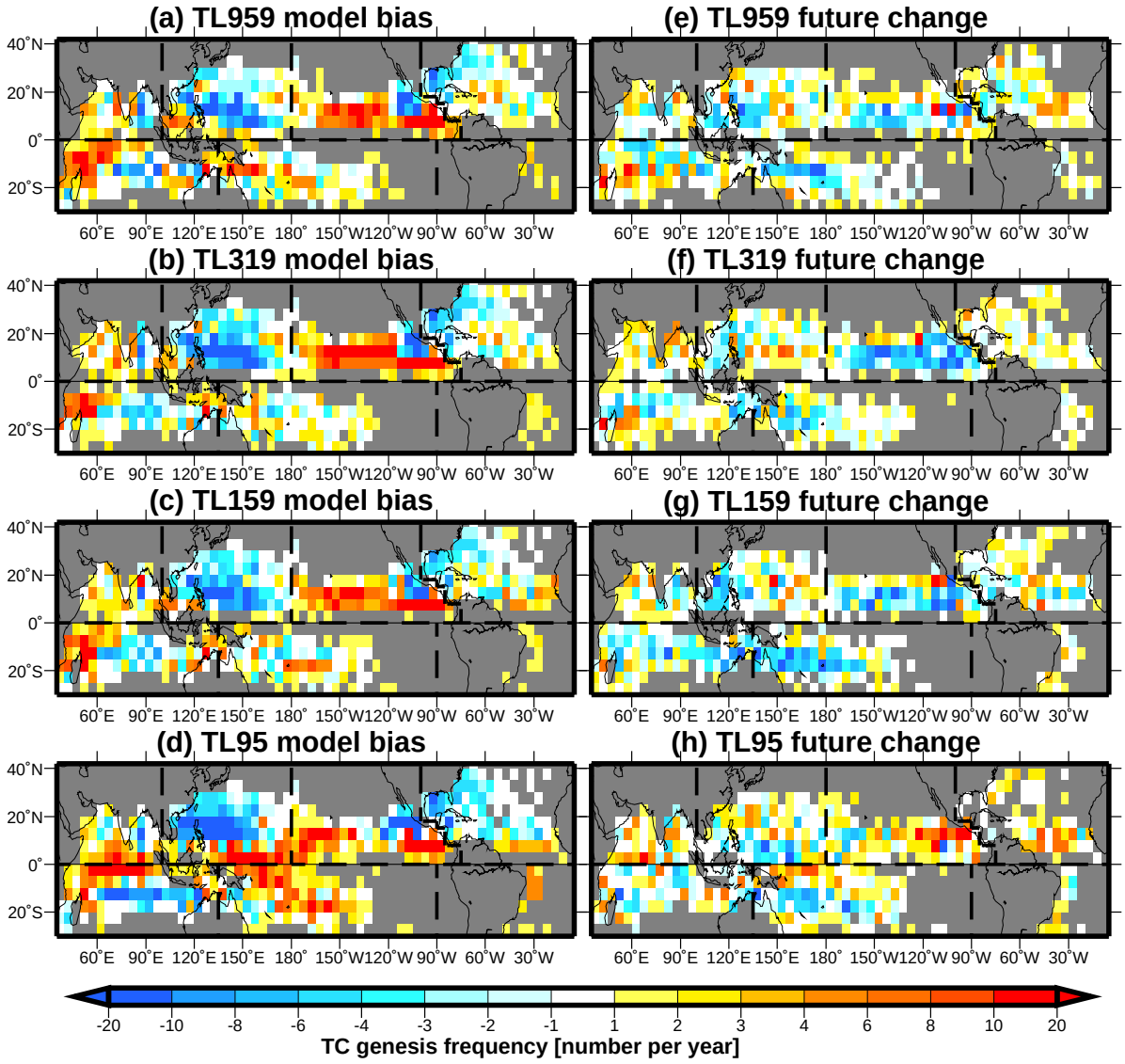

Figure 3.8: (a–d) Biases and (e–h) future changes in tropical cyclone genesis frequency (TGF) projected by (a, e) TL959, (b, f) TL319, (c, g) TL159, and (d, h) TL95.

Chapter 4

Projected future change in North Atlantic tropical cyclone tracks

This chapter investigates future changes in TC activity, especially changes in TC tracks using a 20-km-mesh AGCM. The geographic focus is North Atlantic (NA).

The model, simulation settings, and observational datasets used in this chapter are exactly same as those described in Section 3.1. The observed SST was prescribed in the present-day run (1979–2003), while the ensemble mean of 18 IPCC-AR4 models under the IPCC SRES A1B was prescribed in the future run (2075–2099) (See Fig. 3.2c for the future changes in the climatological mean SST).

Section 4.1 outlines the analytical methods, including TC detection and the GPI. Section 4.2 provides details on model performance in the present-day simulation. Section 4.3 describes the simulation results in terms of future changes in TCs, and Section 4.4 examines the reasons for the predicted future changes. Finally, Section 4.5 provides a summary of the main findings. Details are also available in Murakami and Wang (2010).

4.1 Analysis methods for projected output

4.1.1 Detection method for tropical cyclones

TC-detection method adopted in this section is a modified version of that used by Oouchi et al. (2006), who employed six criteria to identify TCs in order to match the simulated

annual mean number of global TC genesis with observations. However, the simulated TC numbers in each ocean basin do not agree with observations. The present-day simulation performed by Oouchi et al. (2006) shows that the TC number was markedly underestimated in the WNP, somewhat underestimated in the NA, and significantly overestimated in the South Indian Ocean. Given that this section focuses on changes in TC tracks over the NA, the detection criteria were modified to ensure that the simulated annual number and duration of TCs resemble the observed counterparts. The modified detection criteria are as follows:

1. Across the latitudinal belt of 45 S–45 N, the grid point of the candidate TC-center is defined as that where the minimum surface pressure is at least 2 hPa lower than the averaged surface pressure over the surrounding $7^\circ \times 7^\circ$ grid box.
2. The magnitude of the maximum relative vorticity at 850 hPa exceeds $3.0 \times 10^{-5}\ s^{-1}$ (original value: $3.5 \times 10^{-5}\ s^{-1}$).
3. The maximum wind speed at 850 hPa exceeds 14.0 ms^{-1} (original value: 15.0 ms^{-1}).
4. The temperature structures aloft show a marked warm core: the sum of the temperature deviations at 300, 500, and 700 hPa exceeds 1.2 K (original value: 2 K).
5. The maximum wind speed at 850 hPa (WS850) exceeds that at 300 hPa (WS300) at the first detection (i.e., generation time) of a TC. After generation, WS850 increased by 2.5 ms^{-1} should be greater than WS300 (this latter condition was not required in the original detection).
6. The duration of a TC exceeds 36 hours.

Conditions (1) and (6) are the same as the original conditions employed by Oouchi et al. (2006), whereas conditions (2)–(5) have been modified. The latter part of condition (5) results in a greater number of TC occurrence at mid-latitudes. This criterion is

added because a comparison of simulated TC tracks with observed track data reveals that the model underestimates the number of TC tracks at mid-latitudes in the case that this relaxation is not employed. It might be argued that this relaxation would increase the number of extra-tropical cyclones; however, this condition is only valid for TCs generated at low latitudes. In other words, this study only selects those cyclones with transient characteristics that were generated at low latitudes. This study included these transitional TCs because evaluation of their future changes is important when estimating the future socioeconomic costs arising from TC-related damage.

The model TC positions were counted for every 2.0° × 2.0° grid point over the NA region (0–45 °N, 110 °W–0, excluding the Pacific) every 6 hours. The total count was defined as the frequency of TC occurrence, which indicates the probability of a TC occurring in a certain grid point. When the counting is only applied to genesis location (i.e., when initially identified according to the detection method), the total number of TCs is defined as the frequency of TC genesis. Because TCs in the NA are generated mainly during the boreal summer (July–October; JASO), this study primarily focuses on changes in TC tracks during these months.

4.1.2 Genesis Potential Index (GPI)

To determine the factors responsible for genesis location changes, we used the Genesis Potential Index (GPI) originally developed by Emanuel and Nolan (2004), motivated by the work of Gray (1979). Although the GPI was developed using a statistical fitting procedure, based only on climatological seasonal and spatial variations in TC genesis, it shows some skill in reproducing inter-annual variations in the observed frequency and location of TC genesis for several basins (Camargo et al., 2007a). GPI values increase when large-scale conditions are favorable for TC genesis, and decrease when conditions

are unfavorable. The formulation of the original GPI is as follows:

$$GPI = |10^5\eta|^{\frac{3}{2}} \left(\frac{RH}{50}\right)^3 \left(\frac{V_{pot}}{70}\right)^3 (1 + 0.1V_s)^{-2}, \tag{4.1}$$

where η is the absolute vorticity (s^{-1}) at 850 hPa, RH is the relative humidity (%) at 700 hPa, V_{pot} is the maximum potential intensity (MPI; ms^{-1}) of Emanuel (1995), and V_s is the magnitude of the vertical wind shear (ms^{-1}) between 850 and 200 hPa. Among these factors, only vertical wind shear is negatively correlated with the GPI. The relative humidity and maximum potential intensity are considered as thermo-dynamical factors. The MPI is an empirical value, and is determined by the vertical structure of temperature and moisture, and SST. The definition of MPI is based on Emanuel (1995), but as modified by Bister and Emanuel (1998):

$${V_{pot}}^2 = \frac{C_k}{C_D}\frac{T_s}{T_0}\left(CAPE^* - CAPE^b\right), \tag{4.2}$$

where C_k is the exchange coefficient for enthalpy, C_D is the drag coefficient, T_s is the SST (K), and T_0 is the mean outflow temperature (K). The quantity $CAPE^*$ is the value of convective available potential energy (CAPE) of air lifted from saturation at sea level, with reference to the environmental sounding, and $CAPE^b$ is that of the boundary layer air. Both quantities are evaluated near the radius of maximum wind which is iteratively determined assuming the wind field is balanced by the radial pressure gradient in the eye region.[1]

Camargo et al. (2007a) calculated the GPI using reanalysis data, showing good agreement between observational data and the climatology and ENSO-related variability in GPI. Camargo et al. (2007b) applied the GPI to model outputs. The GPI is not only used to provide supplemental information regarding TC genesis estimated from model simulations, but also to clarify the most influential factor in the case of GPI variation due to ENSO or the case of differences identified when comparing different models.

[1] A program source code for computing the MPI is available online at http://texmex.mit.edu/pub/emanuel/TCMAX/

When the original GPI was applied to JRA-25 data, significant discrepancies between the GPI (Fig. 4.1a) and the observed distribution of TC genesis (Fig. 4.1c) were found. First, the original GPI underestimates the frequency of genesis in the Inter-Tropical Convergence Zone (ITCZ) between 7 °N and 15 °N. Second, the GPI underestimates the frequency of TC genesis in the eastern Pacific.

It is expected that TC generation is strongly related to large-scale mean vertical motion. Indeed, the regions with a high frequency of TC genesis correspond to areas with large upward motion. It is possible that upward motion was not fully taken into account in the original GPI, although the relative humidity term may reflect it to some degree. In the present study, the original GPI was modified by explicitly incorporating the following vertical motion term:

$$GPI = |10^5\eta|^{\frac{3}{2}} \left(\frac{RH}{50}\right)^3 \left(\frac{V_{pot}}{70}\right)^3 (1 + 0.1V_s)^{-2} \left(\frac{-\omega + 0.1}{0.1}\right), \tag{4.3}$$

where ω is the vertical wind velocity ($Pa \cdot s^{-1}$) at 500 hPa. Figure 4.1b shows the modified GPI, which yielded improved results in general, including higher values over the eastern Pacific and the Atlantic ITCZ region. However, the modified GPI remains inconsistent with observations of TC genesis around the Florida Peninsula and off coast of west Africa. This inconsistency also appears when the modified GPI is applied to model output, as shown later in Fig. 4.8. Although further improvement of the GPI may be needed, the modified GPI shows future change in detected TC genesis more clearly than did the original GPI.

No other study has applied GPI analysis to such a high-resolution simulation. A concern might naturally arise, that the vertical motion field induced by TCs may contribute to the seasonal mean field. Although the degree to which TCs affect climatological mean vertical motion remains unclear, it is conceivable that the influence is rather limited, given the fact that on average only 9 storms occur during the 4-month peak season. On the other hand, the incorporation of vertical motion into the GPI provides additional

information regarding the physical mechanism for future change in TC genesis.

4.2 Evaluation of the present-day simulation

4.2.1 TC tracks and frequency of occurrence

To evaluate the TC climatology and variations simulated in the present-day (hereafter referred to as "PD") run, this study compared the results with observations. Figure 4.2a and b (Fig. 4.2c and d) show JASO TC tracks (frequency of occurrence) observed and simulated in the PD run, respectively. The difference between the observed and simulated (PD run) frequency of occurrence is shown in Fig. 4.2e. Overall, the simulated TC tracks and frequency of occurrence are similar to the corresponding observations; however, the PD run overestimates the frequency of occurrence in tropical regions (south of 25 ℕ), and underestimates the frequency north of 25 ℕ. The underestimation mainly reflects a lack of cyclogenesis within mid-latitude regions in the PD run. The PD run also underestimates TC genesis over the Gulf of Mexico and the frequency of TCs moving northward from this region, and overestimates the frequency of occurrence in the region offshore from West Africa.

4.2.2 Inter-annual and seasonal variability in TC genesis

Because the prescribed SST and SIC vary from year to year, it is expected to see a corresponding inter-annual variation in TC genesis in the PD run. Figure 4.3a compares the simulated and observed yearly number of TC genesis. The average numbers of TC genesis are 10.5 (observed) and 8.7 (PD run), meaning that the total number of TCs is underestimated. The recently observed upward trend in TC genesis, which is conspicuous from the mid-1990s, is insufficiently reproduced in the PD run. The coefficient of correla-

tion between the PD run and observations is 0.46, which is statistically significant at the 95% level. Therefore, to some degree, the PD run reproduces the observed year-to-year variation in TC genesis number. However, this correlation is weaker than that reported in other studies. For example, ensemble simulations conducted by LaRow et al. (2008) using a global spectral model at a resolution of T126L27 (Gaussian grid spacing of 0.94°) yielded a correlation coefficient of 0.78. Ensemble simulations conducted by Zhao et al. (2009) with a global atmospheric model with a 50-km mesh horizontal grid spacing yielded a correlation coefficient of 0.83. However, the results in the present study are derived from a single run and if the correlation is computed only for the last 15 (10) years of the experiment, the correlation coefficient would increases to 0.65 (0.73).

Figure 4.3b shows seasonal variations in TC genesis. As in nature, the simulated TC genesis shows a rapid increase from June to July, peak in September, and a decrease toward the northern winter. This pattern of variation is well simulated in the PD run. Although LaRow et al. (2008) accurately reproduced the inter-annual variation in TC number, their seasonal cycle of TC number was not well simulated in the NA. In contrast, the experiment by Zhao et al. (2009) performed very well in reproducing both inter-annual variations and the seasonal cycle of TC number. These results, in combination with the present findings, suggest that model performance in simulating of inter-annual variations may be weakly related to performance in simulating the seasonal cycle.

4.2.3 Change in TC activity induced by ENSO

It is clear from Fig. 4.3a that the simulated TC number (PD run) is strongly affected by El Niño-Southern Oscillation (ENSO). For example, TC genesis shows a marked decline during El Niño years (1982, 1986, 1987, 1997, and 2002), consistent with the finding of Gray (1984), who attributed this decrease to enhanced vertical shear of zonal wind over the Gulf of Mexico and Caribbean Sea. In La Niña years (e.g., 1988, 1995, 1998, and 1999),

TC genesis increases due to decreased vertical wind shear; however, this increase is poorly captured by the PD run. This deficiency in TC genesis is generally caused by a number of errors, such as those in the simulated large-scale environment field, and deficiencies in the model's teleconnection linking ENSO and Atlantic atmospheric anomalies. In addition, the integration in this present study is a single run. Use of ensemble simulation may get better results.

To clarify whether the 20-km mesh AGCM employed in the present study contains large-scale errors, the modified GPI was applied to the PD run; it was also applied to the JRA-25 large-scale field to evaluate the influence of the ENSO signal on TC genesis. Figure 4.4 shows GPI anomalies and the locations of TC genesis in July–October (JASO) for each ENSO developing year. Here, El Niño (La Niña) years are defined as 1982, 1986, 1987, 1991, 1997, and 2002 (1988, 1995, 1998, and 1999), following Camargo and Sobel (2005). For JRA-25 and best-track data (Fig. 4.4a and b), marked differences are seen in both GPI and genesis locations. There exists a negative (positive) anomaly in GPI values and frequency of genesis during El Niño (La Niña) years in the main developing regions (MDR, 10–20 °N, 30–80 °W). This contrast in the GPI field between El Niño and La Niña years at lower latitudes (south of 20 °N) is reflected in the PD run (Fig. 4.4c and d), although the GPI signal is different from observations in areas offshore from West Africa in La Niña years. This finding indicates that 20-km mesh AGCM, at least to some extent, simulates differences in the large-scale field between El Niño and La Niña years, which affects TC genesis. The locations of TC genesis in the PD run also differ between the two ENSO phases, although the difference is weaker than that observed. There also exists an inconsistency between the GPI and detected TCs in the PD run. For example, many TCs are generated in the region offshore from West Africa during El Niño years, whereas the corresponding GPI values are small. This overestimation is unrelated to large-scale field errors, although the exact reasons remain to be investigated.

4.3 Projected future change in TC tracks, frequency, and inter-annual variation

Figure 4.5a and b (Fig. 4.5c and d) shows JASO TC tracks (frequency of occurrence) simulated in the PD and future global-warming (hereafter referred to as "GW") runs, respectively. The difference in frequency of occurrence between the two runs is shown in Fig. 4.5e. Compared with the PD run, substantial changes are apparent in the GW run, including an increase in the frequency of TC occurrence over the tropical eastern North Atlantic (hereafter ENA), and the northwestern North Atlantic (hereafter NWNA; around 32–45 °N, 55–80 °W), and a decrease in the frequency over the tropical WNA (including the Caribbean Sea and Gulf of Mexico). This result indicates a decrease in the frequency of TCs that affect the North American continent south of approximately 32 °N and the West Indies. To ensure the physical significance and robustness of the shifts in TC tracks, this study implemented two additional analyses with different TC criteria: one used relatively constrained criteria (compared with the one used in the present study), as employed by Oouchi et al. (2006); and the other used less constrained criteria. These two new sets of detection criteria result in very similar future change in TC tracks (data not shown), thereby demonstrating that the projected future change is independent of the TC criteria employed.

The dotted line in Fig. 4.3a and b shows inter-annual and seasonal variability for the future run, respectively. The annual mean number of TC genesis is 9.2, slightly higher than that in the PD run, although the difference is not statistically significant at the 95% level. Oouchi et al. (2006) also showed increasing TC number over the NA in their future experiment. A resent study by Sugi et al. (2009), using the same MRI/JMA-AGCM but with different resolutions, showed that future change in TC number within a specific ocean basin is strongly controlled by the distribution of relative SST changes rather than the absolute value of local SST. A similar finding was reported by Vecchi and

Soden (2007a). Sugi et al. (2009) also reported an experiment that showed decreasing TC number over the NA with a relatively small future SST change in the NA. However, Knutson et al. (2008) and Zhao et al. (2009) reported decreasing TC number in their future experiment, when SST is prescribed by the same CMIP3 ensemble mean. Overall, the nature of future change in TC number in the NA remains uncertain, as also concluded by Emanuel et al. (2008).

Although the two runs prescribe similar inter-annual variations in SST and SIC (See Section 3.1.3), the inter-annual variation in the GW run (Fig. 4.3a) differs from that in the PD run. This discrepancy is more apparent in the first 20 years for the simulations. The inter-annual variation in TC number in the GW run is strongly affected by the specified ENSO (dotted line in Fig. 4.3a). For example, local minima occur in El Niño years (e.g., 2082, 2083, 2087, 2093, and 2098). Interestingly, the local maxima in La Niña years are more clearly resolved than those in the PD run (e.g., 2084, 2094, and 2095). The seasonal variation in TC frequency (Fig. 4.3b) is similar to that in the PD run, indicating no future change in seasonal distribution.

4.4 Reasons for future change

4.4.1 Reason for future change in TC tracks

The projected change in frequency of TC occurrence is thought to result from changes in steering flows or genesis locations. To help assess which of these two factors is more influential, JASO mean steering flows are shown in Fig. 4.6. Here, steering flows are defined as the pressure-weighted mean flow from 850 to 300 hPa, as suggested by Holland (1993). Overall, TC tracks (Fig. 4.5a and b) follow a combination of the steering flows and beta drift. The beta drift arises from interaction between the gradient of earth's vorticity

and the primary TC circulation, which is generally westward and poleward (Wang et al., 1998). Tracks are followed by westward steering flows around the region offshore from West Africa, north-westward steering flows over the Caribbean Sea and Gulf of Mexico, and north-eastward flows along the area offshore from North America. However, the PD and GW runs show only a small difference in steering flows (Fig. 4.6c), indicating that this is not a primary reason for the predicted change in frequency of TC occurrence. Furthermore, Fig. 4.7 shows a comparison of climatological mean TC translation vectors. The mean TC translation vectors are calculated at every $2.5° \times 2.5°$ grid point based on all the TCs that passed across each point. The TC translation vectors are similar between the PD and GW runs, indicating that each TC moves in a similar direction for both runs for a given genesis location.

In contrast, there exist marked differences in genesis locations between the PD and GW runs. Figure 4.8a and b shows the frequency of TC genesis during the peak cyclone season (JASO) for the PD and GW runs, respectively. The future change is shown in Fig. 4.8c. It is clear that the genesis locations shift eastward from the PD to GW runs, resulting in a large increase in TC genesis in the ENA and a decrease in the WNA. There is also an increasing signal in the NWNA. The increase in the frequency of TC genesis in the ENA indicates that many TCs experience early recurvature and then move northward, whereas the decrease in the WNA indicates a smaller risk of TCs approaching the coast of southeast United States. These changes appear to be consistent with the predicted change in frequency of TC occurrence (Fig. 4.5), thereby indicating that the change of TC frequency is caused mainly by the change in genesis locations.

4.4.2 Reasons for future change in genesis locations

This study investigates the reason for changes in genesis locations based on an analysis using the modified GPI. Figure 4.8d and e shows the GPI in JASO for PD and GW

runs. When these data are compared with the frequency of genesis (Fig. 4.8a and b), the GPI performs reasonably well in capturing the distributions of detected genesis, although it shows large values in the area around the Florida Peninsula, where TC genesis does not occur. When future changes in the GPI (Fig. 4.8f) are compared with those of TC genesis frequency (Fig. 4.8c), the GPI change largely captures the change in TC genesis frequency. For example, contrasting changes in the frequency of genesis are found across the longitude 50 °W, with an increase in the ENA and a decrease in the WNA. The GPI change also shows an increasing change in the NWNA.

The GPI can be used to determine which of the factors contributes most to its future change. Here, this study assigns the future value to one of the five GPI elements in Eq.4.3; the other elements are kept at present-day values, as used in the PD run. The "virtual" GPI value is then subtracted from the present-day GPI value. In the case of a large difference, the assigned GPI element is considered an influential factor in terms of GPI change. Figure 4.9 shows the various GPIs in which individual factors are varied. Here, the logarithm of each GPI is considered because summation of the logarithm changes in virtual GPIs (Fig. 4.9b–f) is equivalent to the total change in logarithm GPI between the present and future (Fig. 4.9a) (equivalent to the fractional change used in Vecchi and Soden (2007c)).

Figure 4.10 also shows selected area means of future change in GPI and virtual GPIs for July–October and each month. It is notable that changes in the maximum potential intensity and omega terms make a dominant contribution to the increase in GPI within the ENA (Fig. 4.10b). The vertical shear term also contributes to the future increase in GPI to some degree, but the vorticity term makes only a minor contribution in the ENA (Fig. 4.10b). In contrast to the ENA, the relative humidity and omega terms make the largest contribution to the decrease in GPI within the WNA (Fig. 4.10a). The dominant contributions of these terms are robust for the entire peak season (Fig. 4.10a). The

increase in GPI in the NWNA is due to an increase in maximum potential intensity (Figs. 4.9d and 4.10c) and in part to an increase in the vertical shear term (Figs. 4.9c and 4.10c).

Although many studies have reported that vertical shear is crucial for future change in TC genesis over the WNA (e.g., Knutson et al., 2008; Vecchi and Soden, 2007c), the GPI analysis performed in the present study reveals that vertical shear has relatively small influence on the future change in GPI in the WNA. However, this does not necessarily mean that signals of circulation change projected by our simulations are markedly different from those reported in other studies. For example, the spatial distribution of future change in the vertical shear of horizontal wind (Fig. 4.11) is somewhat similar to that reported by Vecchi and Soden (2007c) (see their fig. 1b), indicating that the vertical shear also contributes, at least to some extent, to future change in TC genesis in our projections. Vecchi and Soden (2007b) also examined the response of tropical atmospheric circulation to global warming experiments using projections by the IPCC AR4 models. The authors reported that in all models, the strength of atmospheric overturning circulation decreases as the climate warms. Similarly, our projection resulted in a consistent future change: a weakening in overturning circulation of about 10–12% in the GW run. Vecchi and Soden (2007b) also reported that the weakening occurs preferentially in the zonally asymmetric (i.e., Walker) rather than zonal-mean (i.e., Hadley) component of the tropical circulation. This change is also found in our projections, whereby, weakening was more pronounced in the zonally asymmetric component than in the zonally symmetric component.

As shown above, the GPI change in the ENA is mainly due to change in large-scale vertical motion and maximum potential intensity, which appear to be related to enhanced convective activity in the ITCZ. Figure 4.12 shows changes in the July–October mean vertical velocity at 500 hPa and relative humidity at 600 hPa in the NA. It is clear that

upward motions are enhanced in the ENA, as is relative humidity. These changes are consistent with a predicted increase in precipitation (Fig. 4.13). Overall, these favorable environmental conditions for convective activity promote TC genesis near the eastern Atlantic ITCZ. In contrast to the findings for ENA, the WNA features a decrease in upward motion (Fig. 4.12c), and reduced relative humidity (Fig. 4.12f) and precipitation (Fig. 4.13c).

The increase in convective activity in the ENA appears to be related to the prescribed future SST distribution. Figure 4.14 shows the distribution of forced SST and the difference between present and future values. The magnitude of increase in SST over the NA ranges from 1.8 to 2.8 K; however, the SST changes are spatially variable, with a relatively large increase in the ENA and NWNA, and a relatively small increase in the WNA. Note that precipitation is reduced in the WNA (Fig. 4.13c) despite the local increase in SST (Fig. 4.14c). This finding indicates that the increase in vertical motion in the eastern MDR region acts to enhance zonal circulation, which in turn results in the suppression of convective activity over the WNA. The enhanced Pacific ITCZ precipitation along 5–10 °N (Fig. 4.12c and Fig. 4.13c) can also reduce the ascent over the Caribbean Sea. In other words, the distribution of the SST anomaly is important not only for local TC genesis, but also for remote TC genesis in the NA.

The projected future change in NA SST is a robust signal. Figure 4.15 shows future change in SST relative to the tropical mean for 18 individual CMIP3 models. These models are used for computing the prescribed SST change and trend in the GW run. It is notable that most of the CMIP3 models show a larger SST increase in the ENA than in the WNA, indicating that the east-west contrast in SST change is robust across the models. The MRI/JMA-AGCM shows a higher frequency of TC genesis in the ENA, resulting in an increased TC number at the basin scale and increased TC frequency in the ENA. Although modeling studies have reported conflicting results regarding the future TC number, an

eastward shift of frequency of TC occurrence is probably robust if a model is forced by a prescribed SST change with an east-west contrast in the tropical NA. For example, Knutson et al. (2008) used a similar pattern of SST increase in a future simulation (see their fig. S2a) and obtained a decreased in the number of TC tracks in the WNA and an increase in the ENA (see their fig. 2). Interestingly, Vecchi and Knutson (2008) reconstructed an observational TC dataset since the late 1800s, and showed a similar trend with an east-west contrast in TC occurrence pattern. This consistency among different studies indicates the likelihood that a signal of climate change induced by global warming might have already appeared.

4.5 Summary

This study conducted a pair of 25-year climate simulations for the present day (1979–2003, PD) and the last quarter of the 21st century (2075–2099, GW), based on the A1B scenario using the MRI/JMA 20-km-mesh high-resolution atmospheric general circulation model. The analysis focused on tropical cyclone (TC) activity, especially TC tracks, over the NA. The PD simulation demonstrates that the MRI/JMA-AGCM simulated a reasonably realistic climatology and variations in TC activity over the NA (Fig. 4.2). The observed spatial distribution of the frequency of TC occurrence during July–October (JASO) was largely captured by the PD simulation, although overestimating TC frequency in tropical regions south of 25 °N and underestimating the frequency north of 25 °N. The underestimation is mainly due to a lack of cyclogenesis in mid-latitude regions. The correlation coefficient in inter-annual variation of the TC frequency between observations and the PD run was 0.46, which is statistically significant at the 95% level (Fig. 4.3). The simulated seasonal variation in TC counts is also realistic, although the TC genesis number is slightly underestimated for the entire year. To better understand climate control of TC genesis, the original GPI produced by Emanuel and Nolan (2004) was modified by

incorporating variations in environmental vertical motion. Overall, the modified GPI showed an improved representation of TC genesis climatology over the NA (Fig. 4.1). However, the modified GPI is still inconsistent with the observed TC genesis around the Florida Peninsula.

Concerning future change, the basin-wide TC frequency shows a slight increase in the GW run, but the increase was not statistically significant. The change in frequency of TC occurrence was spatially inhomogeneous, with a marked decrease in the WNA, including the Gulf of Mexico and Caribbean Sea, and an increase in the ENA and NWNA (Fig. 4.5). In theory, there are two possible explanations of the predicted changes in frequency of TC occurrence: changes in large-scale steering flow patterns and changes in TC genesis locations. A comparison of steering flow between the PD and GW runs reveals no significant change (Fig.4.6). Furthermore, mean TC translation vectors are similar between the two runs (Fig. 4.7). On the other hand, a significant change in the locations of TC genesis was found between the PD and GW runs (Fig. 4.8), which is the major reason for the predicted future change in frequency of TC occurrence. The signal of shift in TC locations is well captured by the projected GPI change (Fig. 4.8). Therefore, the GPI can be used to determine the main environmental factors responsible for future change in TC genesis. The main factors contributing to the predicted future increase in TC genesis in the ENA were changes in maximum potential intensity and vertical motion, which are related to the enhanced convective activity in the eastern Atlantic ITCZ (Fig. 4.10). The factors responsible for the increase in TC genesis in the NWNA were maximum potential intensity and reduced vertical shear. The former appears to be related to a relatively large local increase in SST compared with other regions in the NA, whereas the latter seems to be due to decreased westerly wind in the middle troposphere, which is a similar to a signal during El Niño years to that reported by Vecchi and Soden (2007b). The decrease in TC genesis in the WNA was mainly related to decreases in relative humidity and ascending motion. Although the prescribed sea surface temperature (SST) showed an increase in

the WNA, convective activity decreased, indicating that the effect of remote dynamical forcing exceeds the effect of local thermo-dynamical forcing. In other words, the increase in convective activity in the ENA or in the eastern Pacific was sufficiently large to result in a subsidence anomaly over the WNA, which suppressed convective activity and lead to decreased TC genesis.

Overall, present study suggests that the spatial pattern of the frequency of TC occurrence will show marked changes in the future, including a decrease in TC activity in the WNA and increases in the ENA and NWNA. However, it must be considered the fact that these changes are affected by marked model biases. To achieve more reliable future projections, these biases should be minimized. In addition, TC genesis appears to be sensitive to the spatial distribution of SST anomalies, and models with different physics probably respond differently to the SST increase. Although many CMIP3 models show a consistent spatial pattern of SST future change, it would be necessary to perform experiments with various spatial patterns of SST anomalies and model physics in order to reduce the degree of uncertainty in future projections.

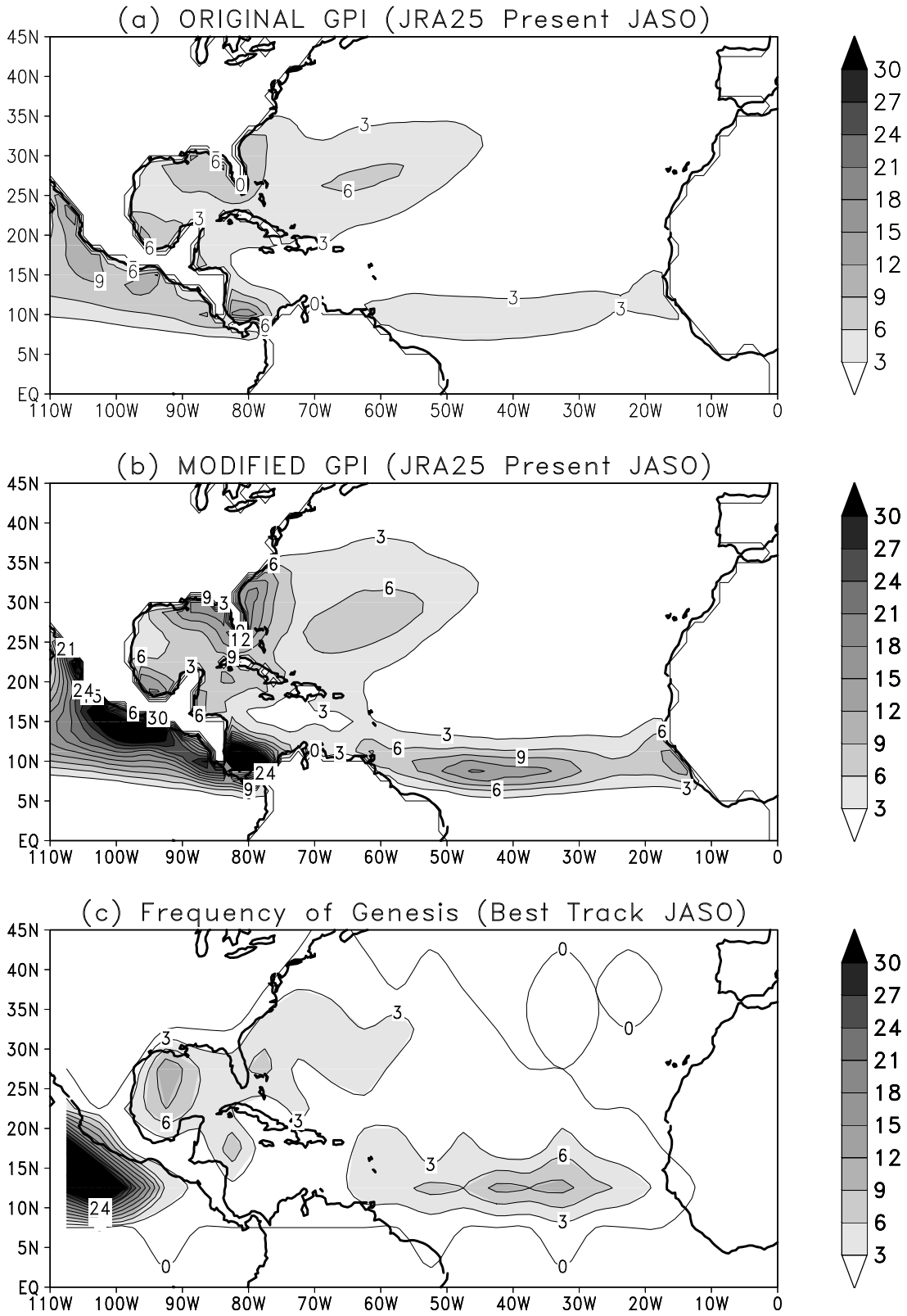

Figure 4.1: July–October (JASO) mean of (a) original Genesis Potential Index (GPI), (b) modified GPI, and (c) frequency of tropical cyclone genesis based on best-track data in the North Atlantic. The GPI data were calculated using JRA-25 reanalysis data for the period 1979–2003.

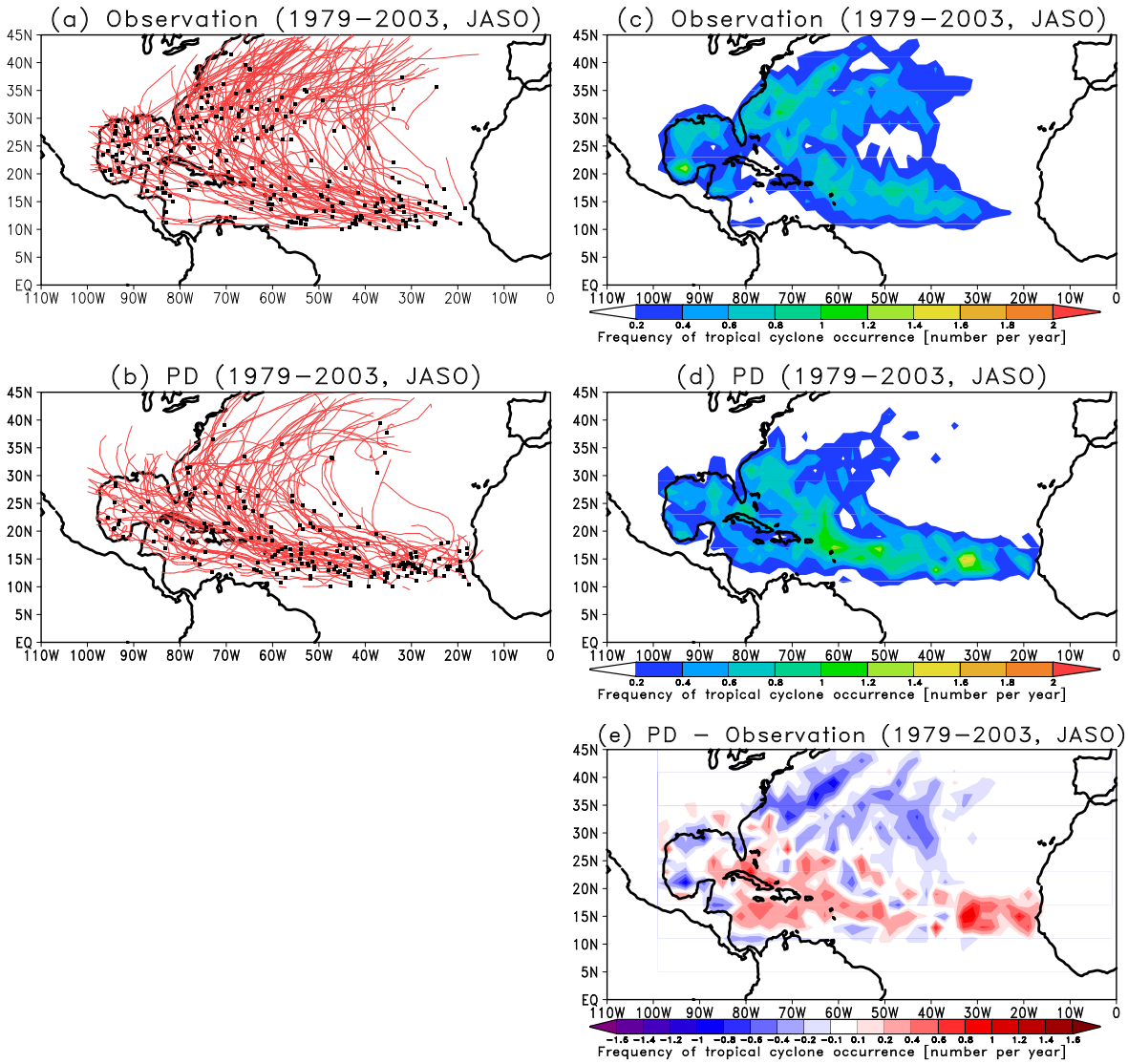

Figure 4.2: Total tropical cyclone tracks (a–b) and frequency of occurrence (c–e) during July–October (JASO) from 1979 to 2003 in the North Atlantic. (a) and (c) are observed data, while (b) and (d) are data from the present-day (PD) run. The difference in frequency of occurrence between the present-day (PD) run and observations is shown in (e). Black dots in (a)–(b) show TC-genesis locations.

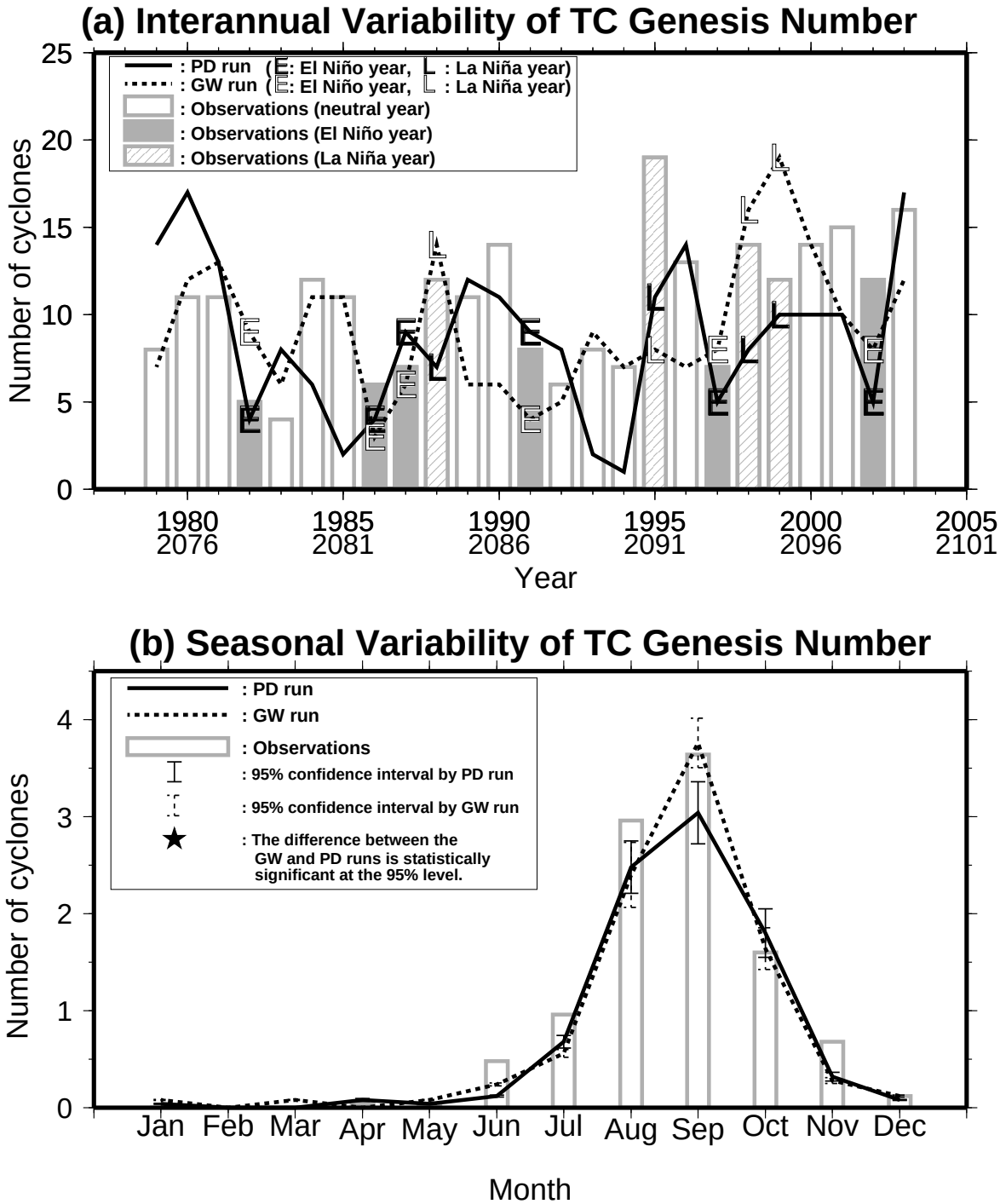

Figure 4.3: (a) Yearly and (b) seasonal variability in the number of generated tropical cyclones, based on observations (1979–2003; histogram), the present-day run (PD; 1979–2003; solid black line), and the global-warming run (GW; 2075–2099; dotted black line). The coefficient of correlation for yearly TC number between the PD run and observation is 0.46, which is statistically significant at the 95% level. The average annual numbers of TCs are 10.5 (observed), 8.7 (PD run), and 9.2 (GW run). The symbols "E" ("L") in (a) indicate El Niño (La Niña) years, whereas star marks in (b) indicate statistically significance for the difference between the GW and PD runs at the 95% level. The error bars in (b) show two-sided 95% confidence interval for each GW (dashed) and PD (solid) run.

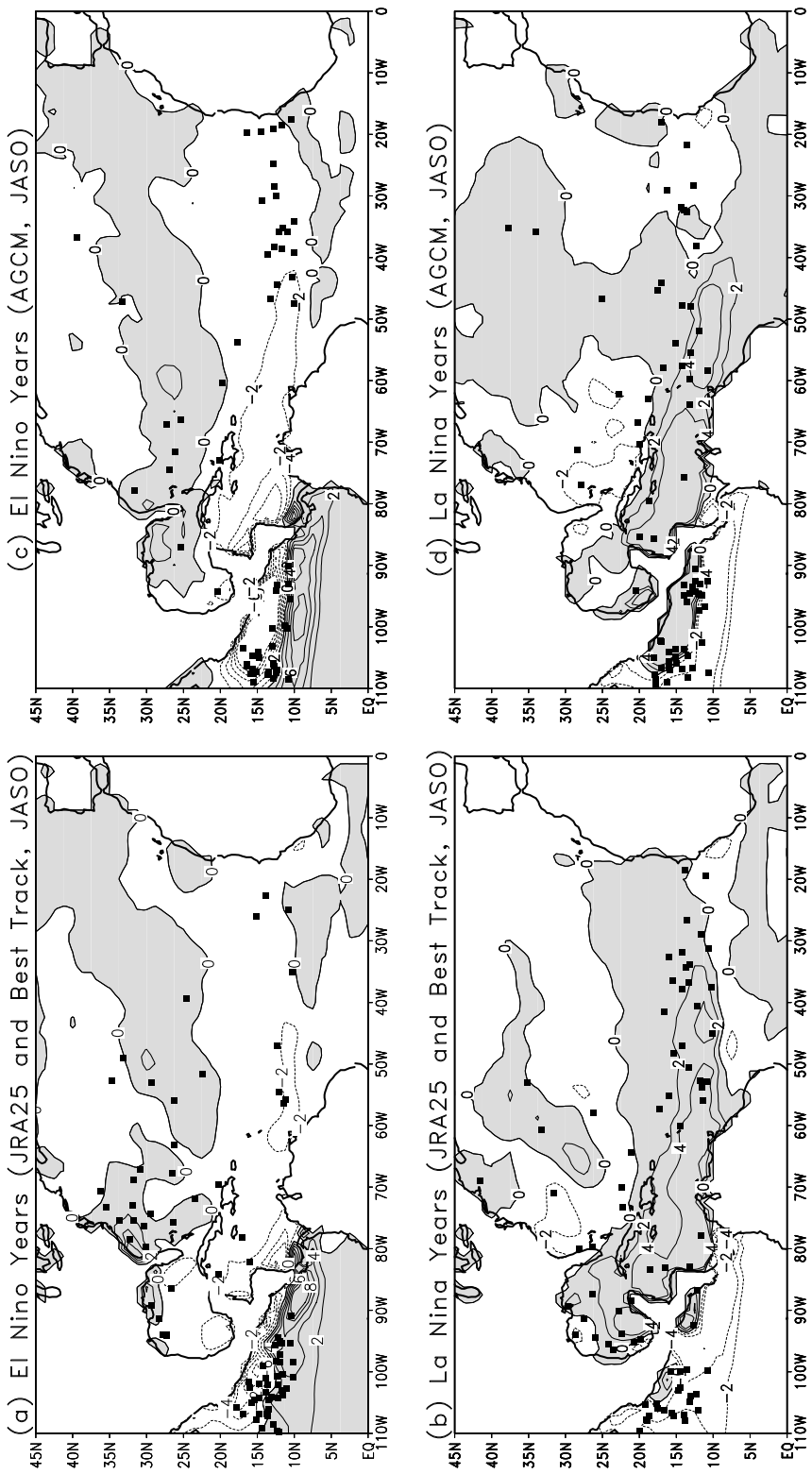

Figure 4.4: Locations of TC genesis (squares) and GPI anomalies (contours) for the period July–October (JASO) during El Niño years (a and c) and La Niña years (b and d). Gray shading indicates a positive anomaly in GPI. (a) and (b) are for the GPI calculated from JRA-25 reanalysis and best-track data. (c) and (d) are for the PD run. El Niño (La Niña) years are defined as 1982, 1986, 1987, 1991, 1997, and 2002 (1988, 1995, 1998, and 1999).

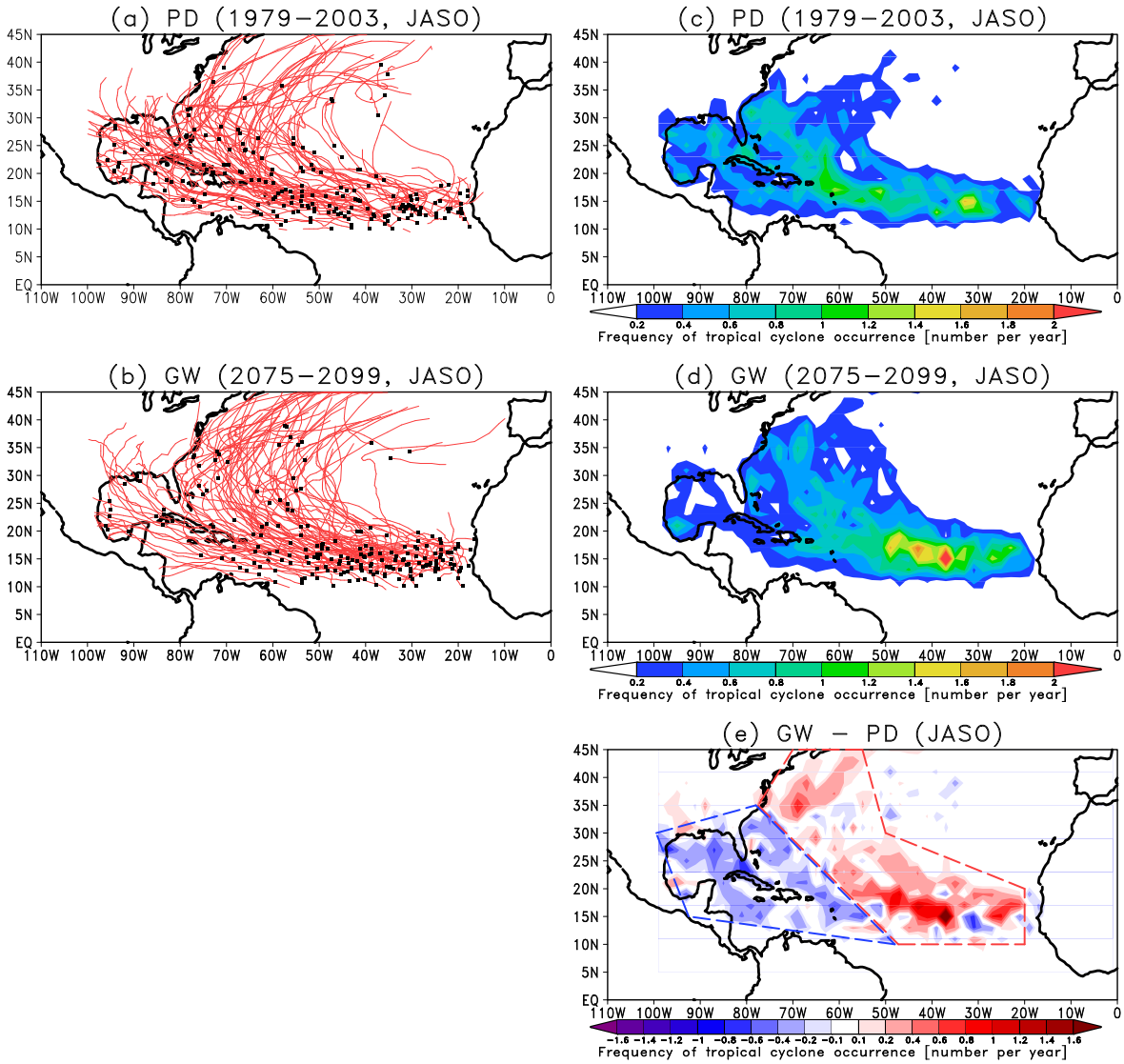

Figure 4.5: As for Fig. 4.2, but for comparisons between the present-day (PD) and the global warming (GW) runs. The dashed regions in (e) highlight an east-west contrast in future change of TC occurrence pattern.

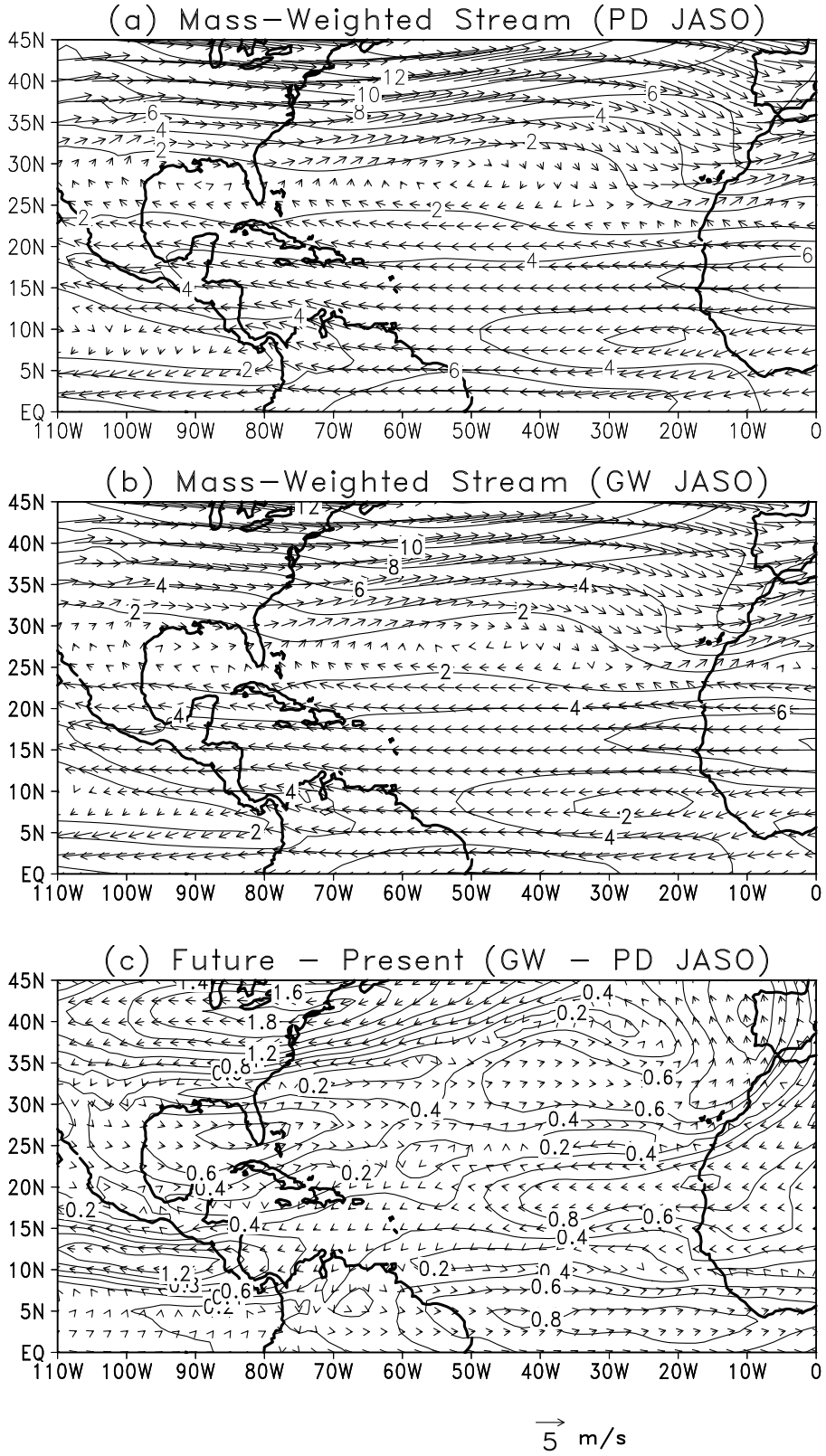

Figure 4.6: Simulated large-scale steering flows (ms^{-1}) for the peak cyclone season of July–October (JASO) for (a) the present-day (PD) run, (b) the global warming (GW) run, and (c) the difference between the GW and PD runs.

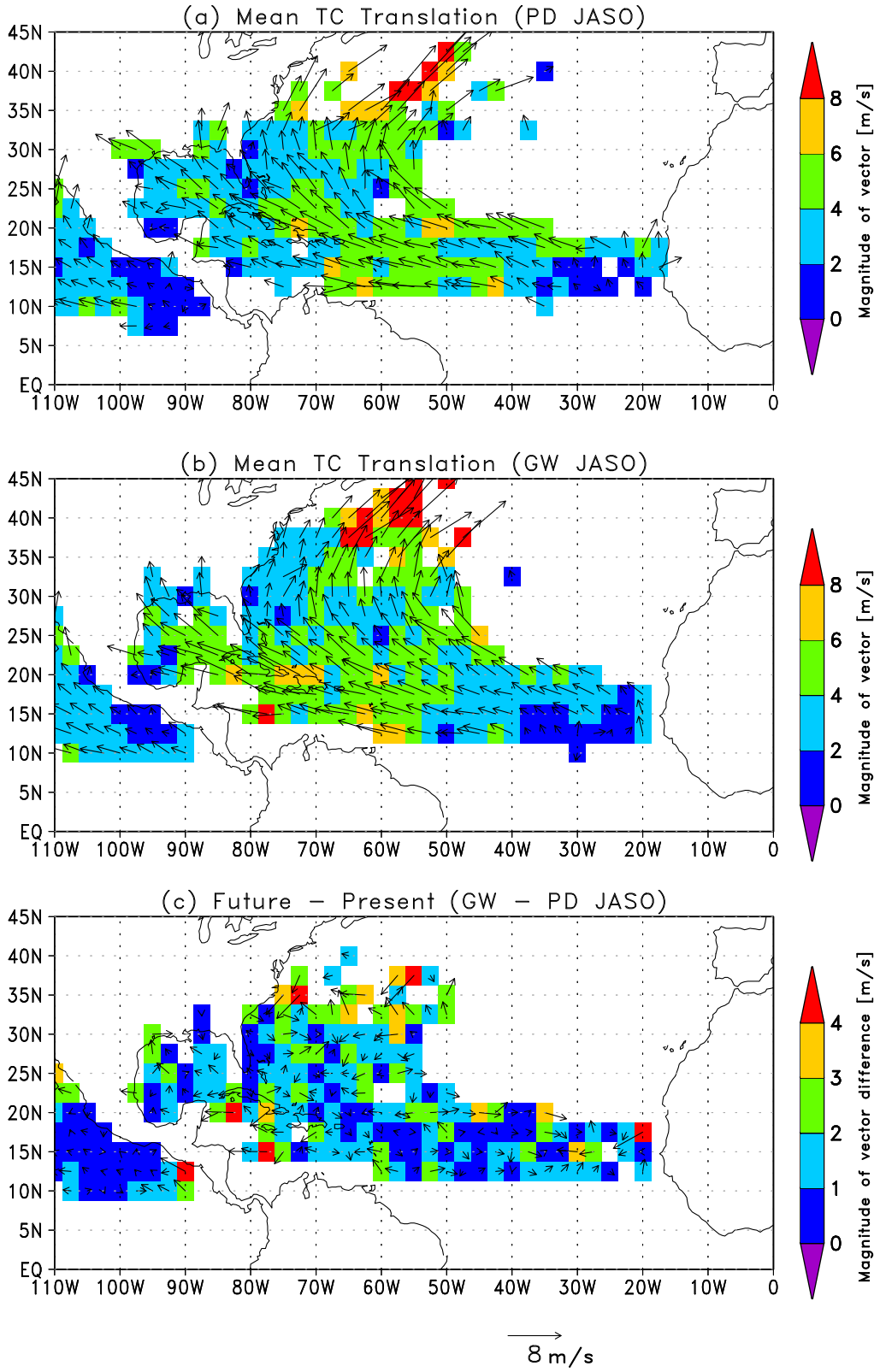

Figure 4.7: Simulated mean TC translation vectors and magnitudes (ms^{-1}) for the peak cyclone season of July–October (JASO) for (a) the present-day (PD) run, (b) the global warming (GW) run, and (c) the difference between the GW and PD runs. More than seven storms per each grid are required for the plots.

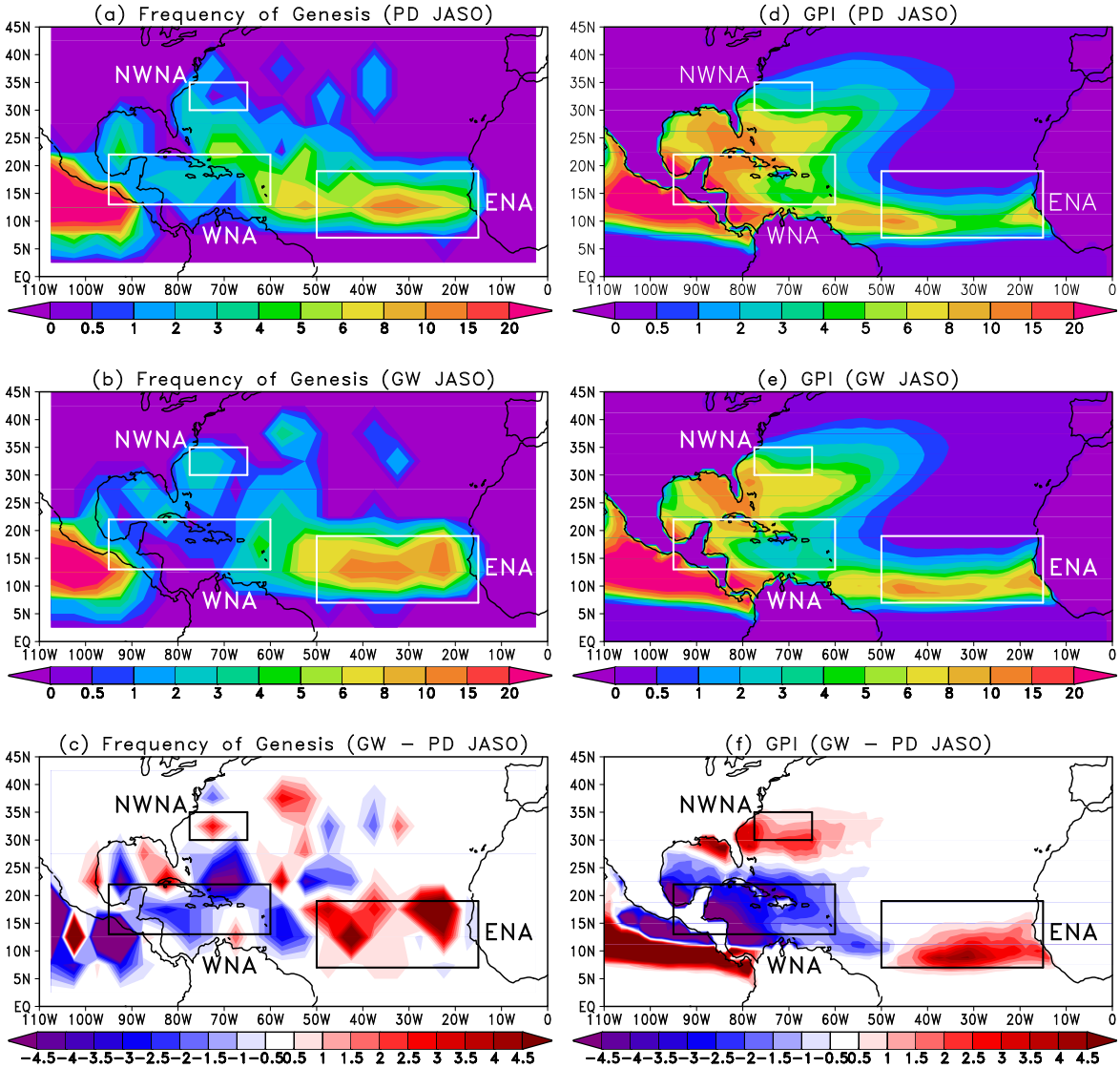

Figure 4.8: Simulated frequency of tropical cyclone genesis for the peak cyclone season of July–October (JASO) for (a) the present-day (PD) run, (b) the global warming (GW) run, and (c) the difference between the GW and PD runs. (d)–(f) are the same as (a)–(c), but for the Genesis Potential Index (GPI). Rectangles show regions (Eastern North Atlantic (ENA), Western North Atlantic (WNA), and Northwestern North Atlantic (NWNA)) with pronounced changes in TC genesis (see text).

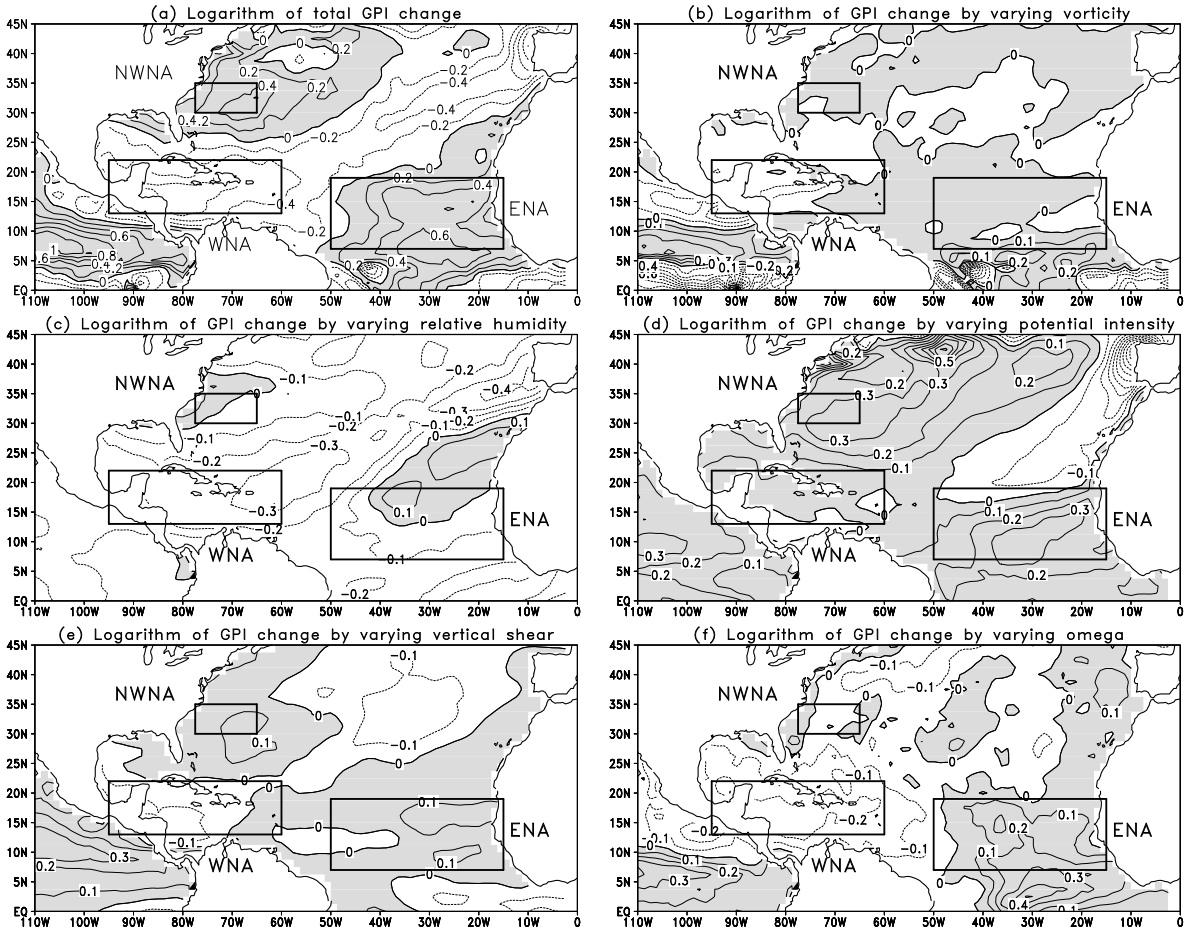

Figure 4.9: Future change in the Genesis Potential Index (GPI) during July–October (JASO) over the North Atlantic for (a) non-varying GPI (i.e., difference in GPI between the global warming (GW) and present-day (PD) runs), and for GPI changes obtained by varying (b) vorticity, (c) relative humidity, (d) maximum potential intensity, (e) vertical shear, and (f) omega, where in each case the other variables were those of the PD run. Gray shading indicates positive values. Rectangles show regions (Eastern North Atlantic (ENA), Western North Atlantic (WNA), and Northwestern North Atlantic (NWNA)) with pronounced changes in TC genesis (see text).

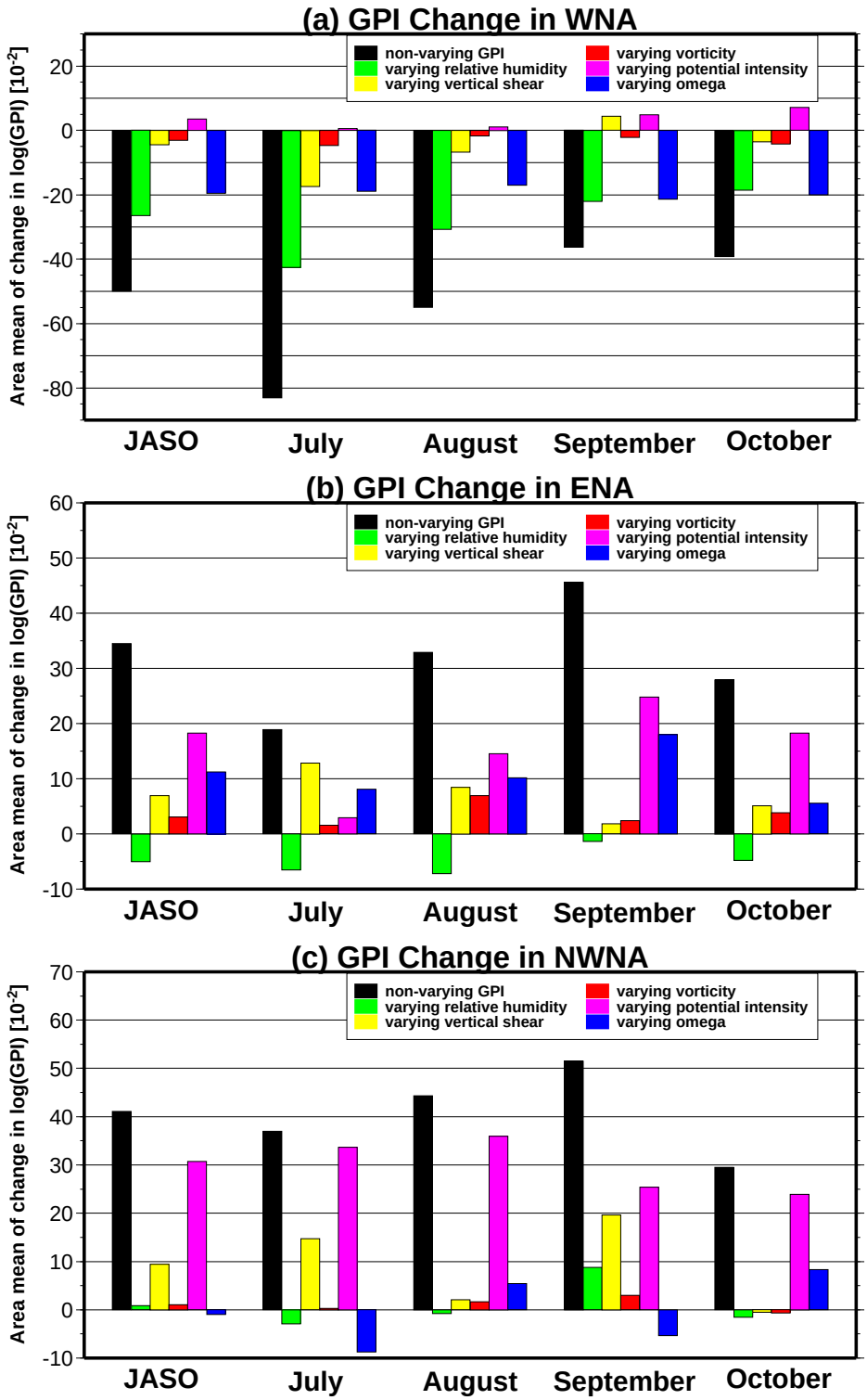

Figure 4.10: Area mean of future change in the Genesis Potential Index (GPI) during July–October (JASO) and each month for (a) western North Atlantic (WNA), (b) eastern North Atlantic (ENA), and (c) northwestern North Atlantic (NWNA). The non-varying GPI (black) is the difference in GPIs between the global warming (GW) and present-day (PD) runs. The varying GPIs (colors) are the virtual GPIs obtained by varying relative humidity (green), vertical shear (yellow), vorticity (red), maximum potential intensity (pink), and omega (blue), where in each case the other variables were those of the PD run.

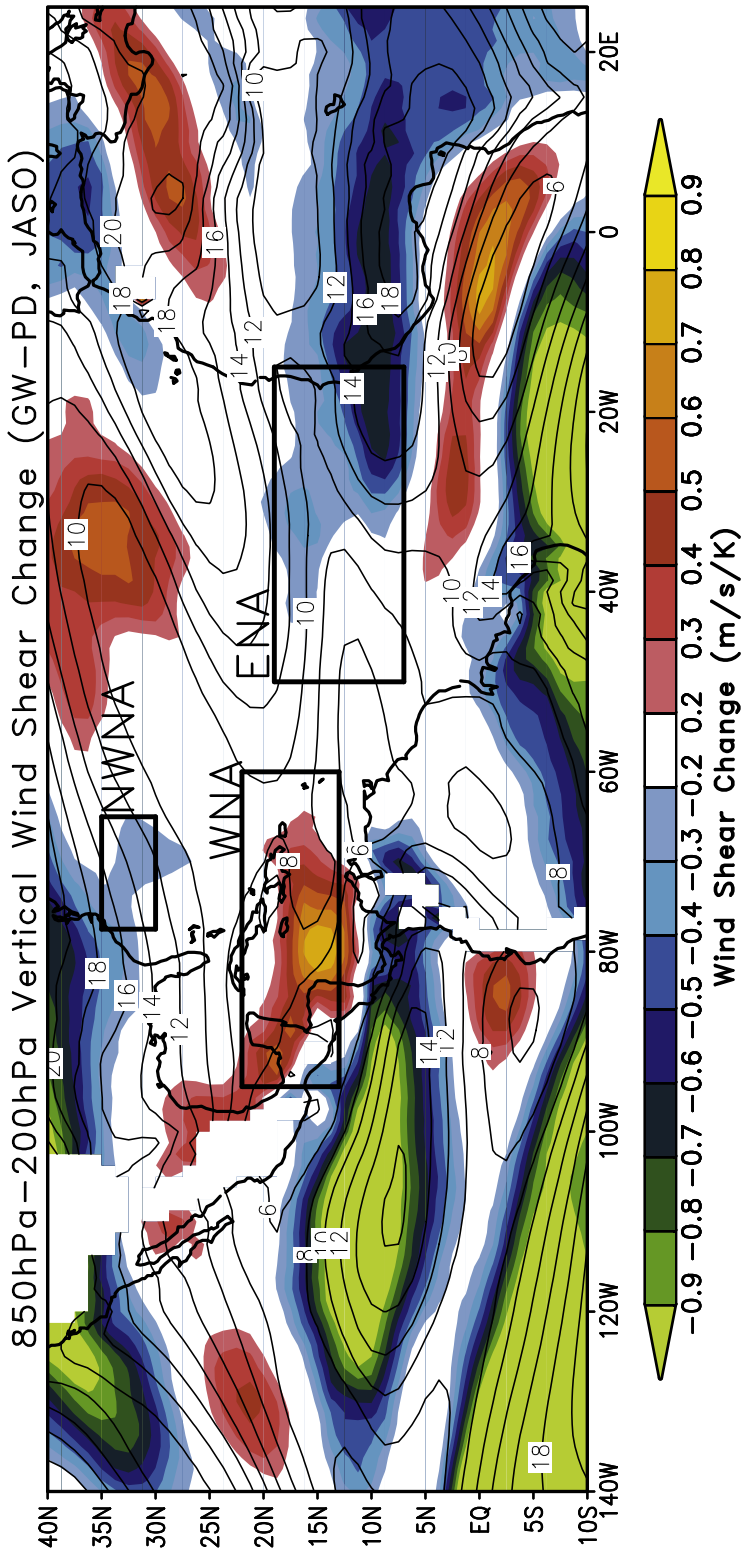

Figure 4.11: Simulated change in July–October (JASO) 850–200 hPa vertical wind shear (shaded, $ms^{-1}C^o$ warming). Contours show the absolute value of the vertical wind shear (ms^{-1}) simulated by the PD run. The figure corresponds to fig. 1a of Vecchi and Soden (2007c). Rectangles show regions (Eastern North Atlantic (ENA), Western North Atlantic (WNA), and Northwestern North Atlantic (NWNA)) with pronounced changes in TC genesis (see text).

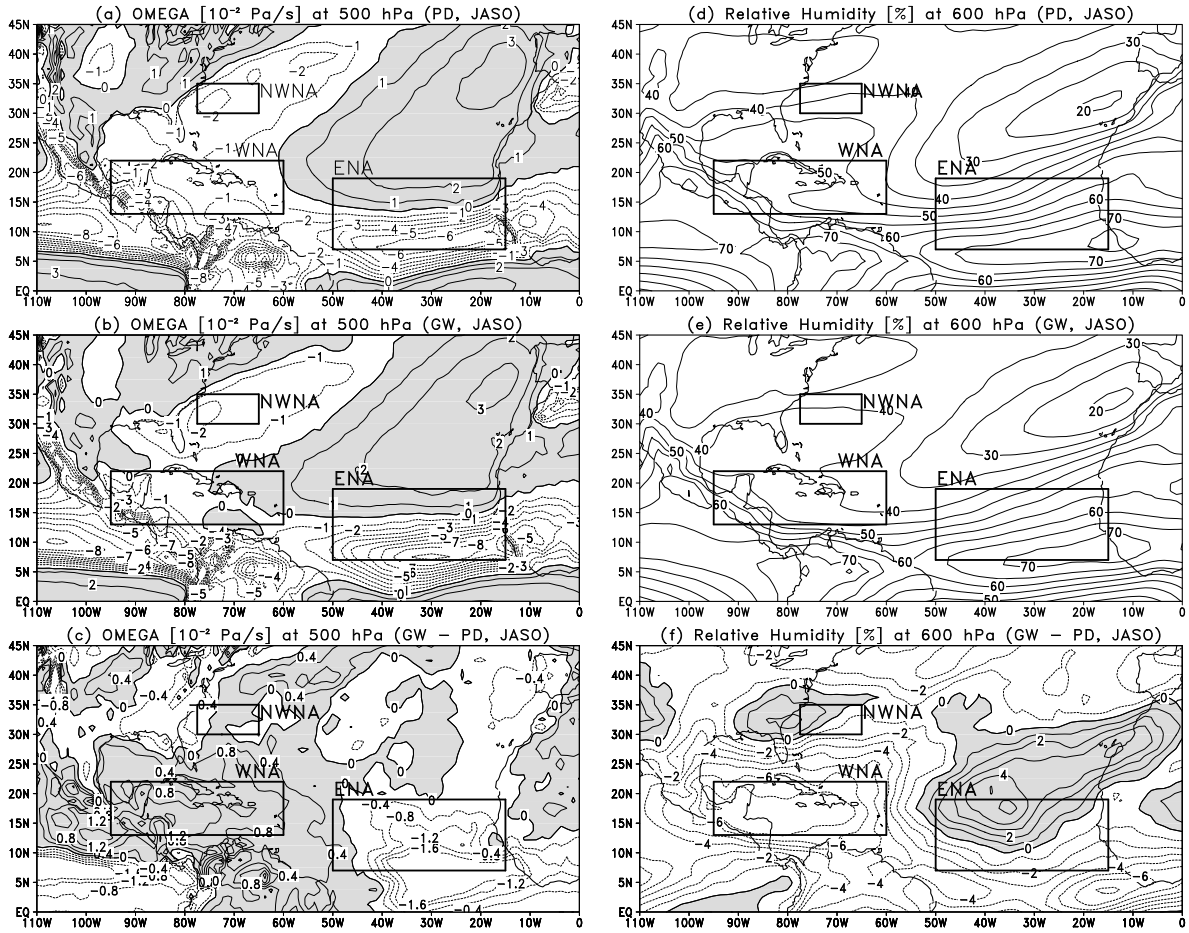

Figure 4.12: Vertical velocity at 500 hPa (a–c) and relative humidity at 600 hPa (d–f) for the peak cyclone season of July–October (JASO) for (a, d) the present-day (PD) run, (b, e) the global warming (GW) run, and (c, f) the difference between the GW and PD runs. Gray shading in (a)–(c) and (f) indicates positive values. Rectangles show regions (Eastern North Atlantic (ENA), Western North Atlantic (WNA), and Northwestern North Atlantic (NWNA)) with pronounced changes in TC genesis (see text).

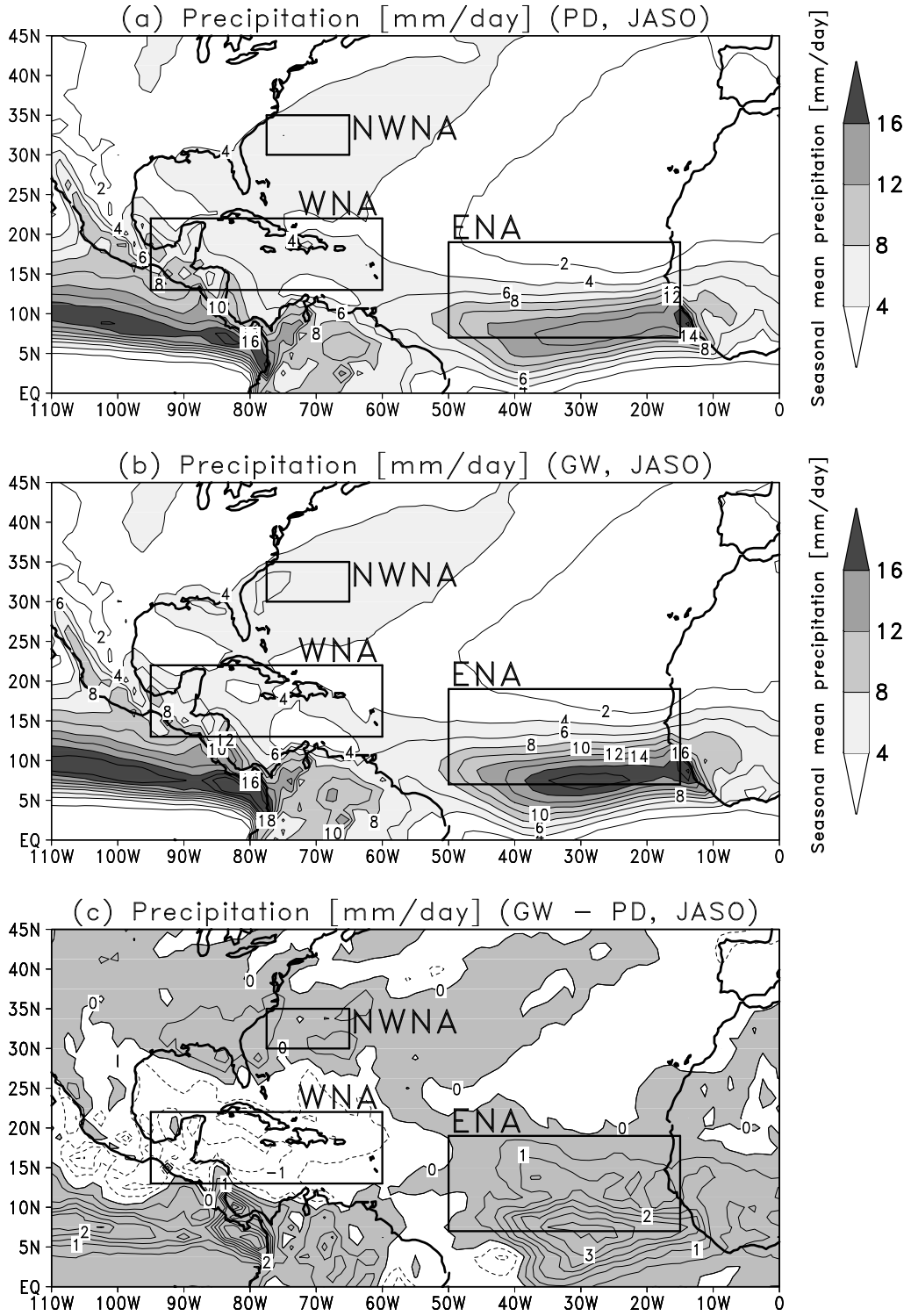

Figure 4.13: Seasonal mean precipitation [mm/day] for the peak cyclone season of July–October (JASO) for (a) the present-day (PD) run, (b) the global warming (GW) run, and (c) the difference between the GW and PD runs. Gray shading in (c) indicates positive values. Rectangles show regions (Eastern North Atlantic (ENA), Western North Atlantic (WNA), and Northwestern North Atlantic (NWNA)) with pronounced changes in TC genesis (see text).

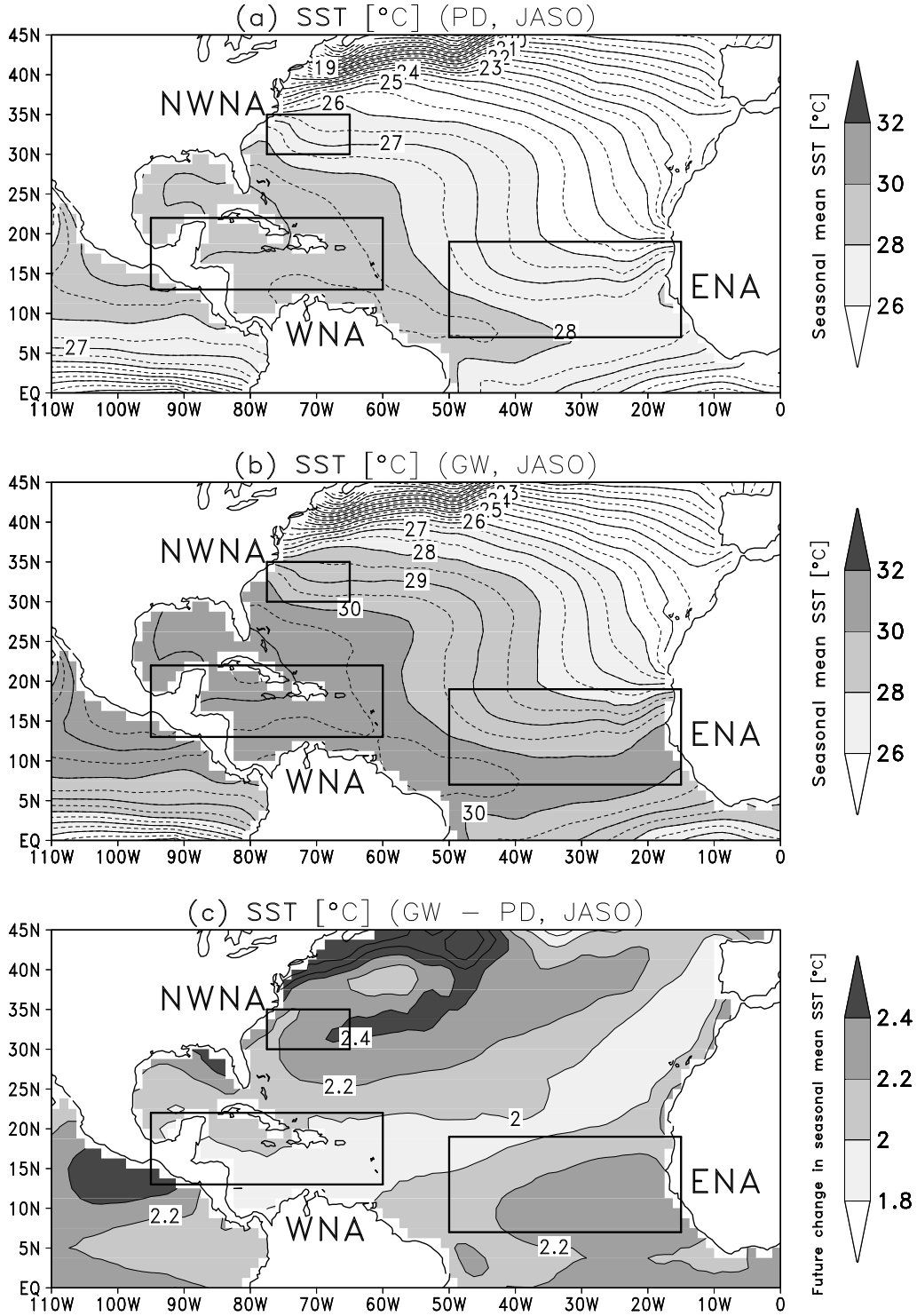

Figure 4.14: Seasonal mean of prescribed SST [℃] for the peak cyclone season of July–October (JASO) for (a) the present-day (PD) run, (b) the global warming (GW) run, and (c) the difference between the GW and PD runs. Rectangles show regions (Eastern North Atlantic (ENA), Western North Atlantic (WNA), and Northwestern North Atlantic (NWNA)) with pronounced changes in TC genesis (see text).

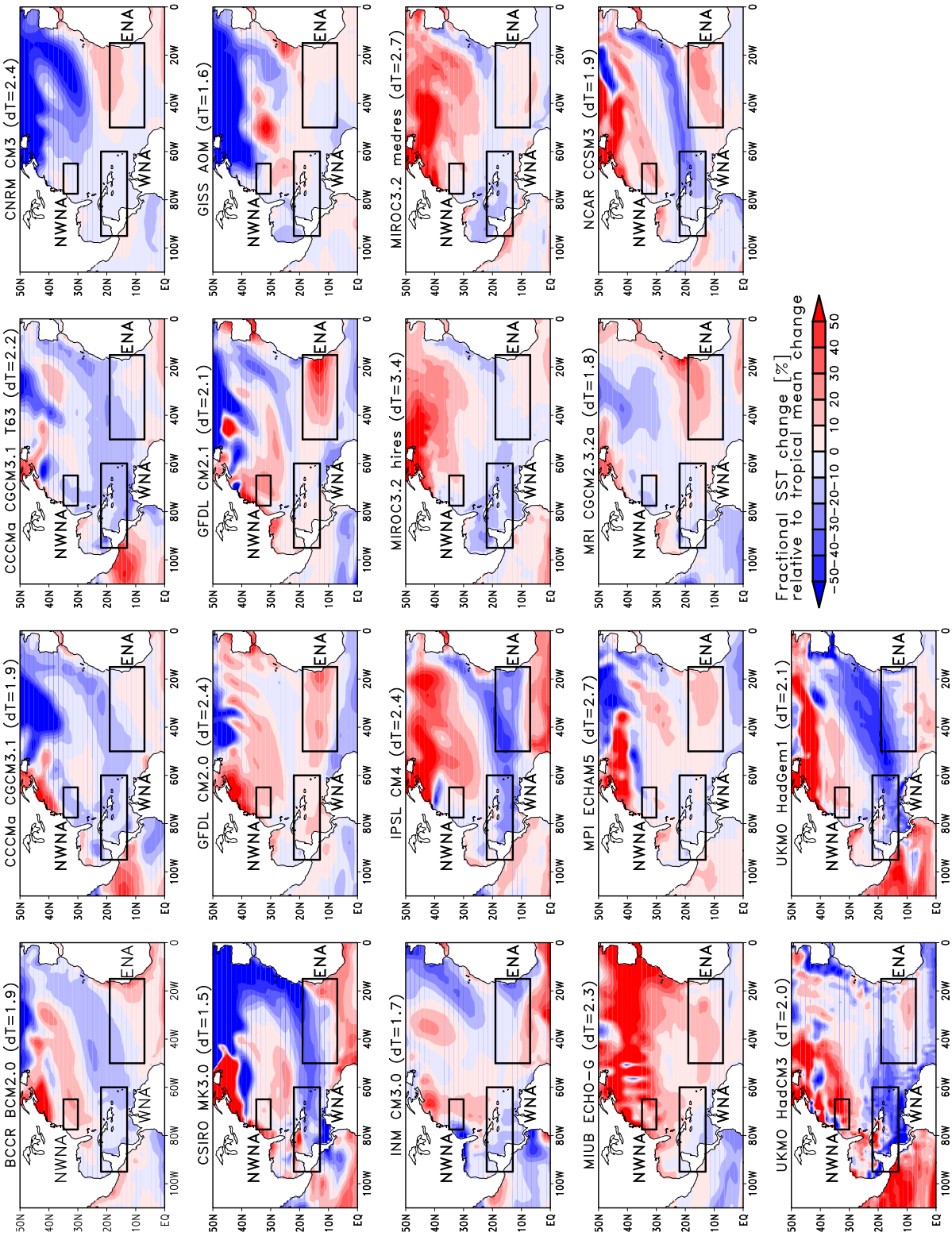

Figure 4.15: Seasonal mean of SST fractional change predicted by each CMIP3 model for the peak cyclone season of July–October (JASO). The distribution of fractional SST change [%] is shown in each panel by subtracting the tropical global (20 ℃N–20 ℃S) averaged SST increase [℃] (indicated in parentheses next to the model name). Rectangles show regions (Eastern North Atlantic (ENA), Western North Atlantic (WNA), and Northwestern North Atlantic (NWNA)) with pronounced changes in TC genesis (see text).

Chapter 5

Projected future change in western North Pacific tropical cyclone tracks

This chapter investigates future changes in TC activity, especially changes in TC tracks using a 20-km-mesh AGCM. The geographic focus is western North Pacific (WNP).

The model, simulation settings, and observational datasets used in this section are exactly same as those described in Chapter 4. The observed SST was prescribed in the present-day run (1979–2003), while the ensemble mean of 18 IPCC-AR4 models under the IPCC SRES A1B was prescribed in the future run (2075–2099) (See Fig. 3.2c for the future changes in the climatological mean SST).

The remainder of this chapter is organised as follows. Section 5.1 and 5.2 provide a brief description of the analytical methods. Section 5.3 assesses the model performance in the present-day simulation against observed best tracks. Section 5.4 presents the projected future changes in TC genesis number, TC tracks, and TC frequency of occurrence (TCF). In Section 5.5, the causes of future changes in TC tracks and TCF are investigated in terms of changes in steering flows, TC translation vectors, TC genesis locations, and TC genesis frequency (TGF). It was found that the change in TC genesis is a critical factor in understanding the changes in TCF and TC tracks. In Section 5.6, the mechanisms responsible for the changes in TC genesis locations are further elucidated with reference to the modified Genesis Potential Index (GPI). Finally, a summary of the results is provided in Section 5.7. Details are also available in Murakami et al. (2010).

5.1 Detection method for tropical cyclones

The globally uniform TC-detection method proposed by Oouchi et al. (2006) results in a marked underestimate of TC genesis number in the WNP (by about 35%) in the present-day (PD) simulation. To better match the simulated annual number and duration of TCs with observed counterparts in the WNP, a set of modified TC detection criteria was developed for the WNP (see below). To facilitate comparison, the threshold values used in Section 4.1.1 (for the NA) are listed in parentheses.

1. Across the 45 °S–45 °N latitudinal belt, candidate grid points for TC centers are defined as those for which the minimum surface pressure is at least 2.0 hPa lower than the average surface pressure over the surrounding 7° × 7° grid box.

2. The magnitude of the maximum relative vorticity at the 850 hPa vertical level exceeds $2.0 \times 10^{-5} s^{-1}$ ($3.0 \times 10^{-5} s^{-1}$ in NA).

3. The maximum wind speed at the 850 hPa vertical level exceeds 10.0 ms^{-1} (14.0 ms^{-1} in NA).

4. The temperature structure aloft has a marked warm core, such that the sum of the temperature deviations at 300, 500, and 700 hPa exceeds 1.0 K (1.2 K in NA). The temperature deviation for each level is computed by subtracting the maximum temperature from the mean temperature over the surrounding 10° × 10° grid box.

5. The maximum wind speed at the 850 hPa vertical level (WS850) is higher than that at the 300 hPa (WS300) at the first detection time. After the first detection, this criterion is no longer applied (in NA, WS850 plus 2.5 ms^{-1} was required to be greater than WS300 following generation).

6. The duration exceeds 36 hours.

Note that the threshold values (2), (3), and (4) are lower than those used in Section 4.1.1. This is necessary because modeled convective activity in the WNP is less intense than that in other basins (Oouchi et al., 2006).

The TC positions were counted for each 2.5° × 2.5° grid area over the WNP region (0–45 °N, 100–180 °E) at 6-hour intervals. The total count for each grid area was defined as the TCF. The first detected position was defined as the location of TC genesis, and the TGF at each grid was counted in the same way as that for TCF. Because the computed TGF fields are noisy, TGF is smoothed using 9-point moving average weighted by the distance from the center of the grid. Because TCs in the WNP are generated mainly during the peak season in the boreal summer (July–October; JASO), this study focuses on changes in TC tracks, TCF, and TGF during these months.

5.2 Statistical significance tests

Tests of statistical significance, for evaluating the difference (i.e., increase or decrease) between mean values, were conducted using Welch's t-test, which assumes two samples with possibly unequal variances. This study also considers adjustments of sample sizes (or freedom) by autocorrelations in time series. A standard statistical test depends on the assumption of random samples. However, if a time series of length N is autocorrelated, the number of independent samples (i.e., the effective sample size) is fewer than N. Here, an effective sample size is derived by the following equation (WMO, 1966):

$$N' = N\frac{1 - r_1}{1 + r_1}, \tag{5.1}$$

where N' is the effective sample size, N is the sample size, and r_1 is the lag-1 (i.e., 1-year) autocorrelation coefficient. For example, if the sample size is 25 years and the lag-1 autocorrelation is 0.5, the adjusted sample size is reduced to 8 years.

5.3 Evaluation of the present-day simulation

5.3.1 TC tracks and frequency of occurrence

The observed and simulated TC tracks and TCF during the peak season of July–October are compared in Fig. 5.1. Overall, TCF is reasonably well simulated in the PD run (Fig. 5.1c and d), showing a maximum northeast of the Philippines (20 °N, 125 °E). However, biases are apparent in Fig. 5.1e. For example, TCF is severely underestimated in the southern Philippine Sea (10–17 °N, 122–150 °E) and in the northeast South China Sea (15–25 °N, 115–122 °E), implying that fewer TCs move westward and penetrate into the South China Sea. In addition, TCF is overestimated in the southwest South China Sea (7–17 °N, 112–115 °E). These biases indicate that some of the westward-moving TCs were erroneously recurved northward before they penetrate into the South China Sea. The low TCF in the southern Philippine Sea is mainly (partly) due to the biases in July (August) (data not shown). The biases were associated with the biases in the mean large-scale flow; specifically, due to the monsoon trough being located farther eastward in July, resulting in strong low-level westerly winds over the South China Sea. The overestimated TCF in the southwestern South China Sea is mainly (partly) apparent in October (September), reflecting overestimated TC genesis in autumn (data not shown). A marked positive bias in TCF is also seen in the eastern quadrant of the WNP (10–27 °N, 152–180 °E), again reflecting an overestimation of TC genesis.

5.3.2 Interannual and seasonal variability in TC genesis

Figure 5.2a compares the observed and simulated TC genesis numbers counted for each calendar year. The observed and simulated annual (peak-season) basin averaged TC numbers are 26.6 (18.4) and 25.0 (17.2), respectively. Figure 5.2a shows that some of the

local maxima and minima are in good agreement between the PD run (solid black line) and observations (histogram). The correlation coefficient of interannual variations between the two is 0.55 (0.71) for the annual (peak-season) TC number, which is statistically significant at the 99% confidence level (based on the significant test for Pearson's product-moment correlation).

Figure 5.2b shows seasonal variations in TC genesis number. This annual variation is reasonably well simulated in the PD run, except that the simulated distribution of TC number is higher later in the season.

5.3.3 Variations in TC genesis influenced by ENSO

ENSO is one of the primary drivers of interannual variations in TCs. Figure 5.3 shows anomalies of TGF along with the modified GPI anomalies in the peak season for contrasting warm and cold phases of ENSO. Here, we computed the observed JASO mean Niño-3.4 (5 °S–5 °N, 120–170 °W) SST for each year from 1965 and 2003. Following Wang and Chan (2002), an El Niño (La Niña) year is defined as a year in which the SST anomaly exceeds (is less than) 0.4 (–0.4) of the standard deviation computed during the period. According to this criterion, El Niño (La Niña) years occurred in 1982, 1986, 1987, 1991, 1994, 1997, and 2002 (1983, 1984, 1985, 1988, 1995, 1998, 1999, and 2000).

The observations (Fig. 5.3a) reveal a marked southeast-northwest contrast in both TGF and GPI, as respectively reported in Wang and Chan (2002) and Camargo et al. (2007a). In the PD run (Fig. 5.3b), the contrasting features are faithfully reproduced. The spatial correlation between observations and the PD run is 0.67 (0.36) for GPI (TGF), indicating that the variance in TC genesis locations induced by ENSO is reasonably well reproduced. The spatial correlation between the GPI and TGF anomalies is 0.46 (0.47) for observations (the PD run). Moreover, the correlation coefficient between the annual mean TC

number (solid line in Fig. 5.2a) and the annual mean basin GPI (data not shown) is 0.44, indicating that the modified version of GPI performs reasonably well in capturing interannual variations in TC genesis (the correlation coefficient obtained for the original version of GPI (i.e., GPI defined by Eq. 4.1) is 0.30). The reasonable agreement obtained between observations and the PD simulation adds confidence to the reliability of the model's future projections.

5.4 Projected future changes

5.4.1 Tropical cyclone genesis number

The dotted lines in Fig. 5.2a and b show interannual and seasonal variability in total TC number in the WNP basin for the GW run, respectively. The annual total number of TCs is 19.3 for the GW run, which represents a reduction of 22.7% compared with the PD run. This difference is statistically significant at the 99% level. Note however, that this reduction occurs only in the late TC season (September–December; Fig. 5.2b). Recall also that the model simulation of the PD climate is less realistic in the later part of the season. This decrease is in contrast to the result for the NA, as reported in Section 4.3, for which the TC number shows a slight increase in the GW run (although not statistically significant). The interannual variation in TC genesis number in the GW run is slightly different from that in the PD run (the correlation coefficient between the two runs is 0.20, which is not statistically significant), although the two runs share the same interannual variation in SST forcing.

5.4.2 Frequency and tracks

Figure 5.4 compares TC tracks and TCF between the PD and GW runs for the peak season of July–October, revealing marked differences (Fig. 5.4e), including a region of decrease (outlined by the blue dashed line in Fig. 5.4e) and a region of increase (dashed red line) immediately east of the belt of decrease. This finding indicates that a larger number of northward recurving TCs would tend to travel along a path farther to the east than they do in the present day, resulting in a decrease in the number of TCs making landfall over or passing close to Korea and Japan. There also exists a region of increased TCF in eastern China (dashed green line) and region of decreased TCF (dashed orange line) in the South China Sea, although there exists a TCF bias in the South China Sea (Fig. 5.1e). TCF also shows a decrease in the far-eastern WNP (dashed yellow line), which is marked by a positive TCF bias (Fig. 5.1e).

The basin-scale total frequency of TC occurrence is predicted to decrease in the future for every month except August. The percentage decrease for the peak season (all seasons) is 7.7% (22.6%) The decrease in total frequency is smaller than the 13.2% decrease in the total TC genesis number during the peak season. This finding indicates that the mean TC life-span will increase in the future, apparently because more TCs will tend to travel over the warm open ocean of the far-east WNP, thereby reducing their chance of making landfall and enhancing their chance of intensifying (Chan and Liu, 2004).

5.4.3 TCs approaching land

The evaluation of future change in the frequency of TC landfall is important for estimating storm-related socioeconomic losses in the future. Figure 5.5 shows observed TCs within the coastal regions of East Asia (within 200 km of the outer edge of the model's land-

surface grid) for nine sub-regions (East Japan, West Japan, Korea, North China, Central China, South China, Southeast Asia, Taiwan, and the Philippines). Note that overlaps exist among these regions. The same results as those described below were also obtained using 300 km of the outer edge (data not shown). Table 5.1 lists the statistics regarding projected accumulated storm days (i.e., the TC frequency derived from 6-hourly data divided by four) for periods when TCs are located in the coastal domains during the peak season of July–October. Most coastal regions show reasonable agreement between the PD run and observations, although considerable discrepancies exist in Southeast Asia and the Philippines, consistent with the error map of TCF (Fig. 5.1e). In terms of future changes, the largest significant reduction (by 44%) is seen over Southeast Asia. The numbers of storm days also decrease (by 9–25%) in East Japan, West Japan, Korea, South China, and the Philippines, although the future changes are not statistically significant. Increases (by 34–58%, although not statistically significant) are seen in North and Central China, consistent with the spatial pattern of future change in TCF (Fig. 5.4e).

When the instantaneous maximum surface wind velocities for TCs are averaged (Table 5.2), all coastal regions show an increasing intensity (by 1–8%), indicating that TC events become increasingly severe in the future, regardless of any change in TC frequency. Because the model underestimates the intensity compared with observations (Murakami and Sugi, 2010), the degree of intensification remains uncertain.

Table 5.3 lists the future change in mean TC number of landfalls for the peak season, which differs from the frequency of TCs (Table 5.1). For the future changes, all regions show somewhat similar changes to those in Table 5.1, except that these changes are statistically insignificant.

5.5 Reasons for future change in TC frequency

5.5.1 Changes in large-scale flows and TC genesis frequency

The changes in TCF can be explained largely in terms of the TC genesis locations and motions, The latter is in turn affected by changes in large-scale steering flows. Here, this study compares the climatological mean of TC translation vectors between the PD and GW runs. The mean TC translation vectors are computed at every 2.5° × 2.5° grid point based on all TCs that passed across each point. July–October mean motion vectors and future change are shown in Fig. 5.6. Note that more than 15 storms are required to draw a motion vector in a grid. The mean vector norm is respectively 3.67 and 3.42 ms^{-1} for the PD run (Fig. 5.6a) and GW run (Fig. 5.6b), indicating, on average, a slightly reduced TC motion speed in the future. Moreover, the future change (Fig. 5.6c) in the mean zonal (meridional) component is respectively 0.36 (–0.06) ms^{-1} and 0.65 (–0.11) ms^{-1} for the entire basin and regions south of 20 °N, indicating a significant future "slow-down" in the westward translation speed. This reduced speed is especially pronounced in tropical regions around 135 °E and east of 150 °E.

The vectors in Fig. 5.7 show future changes in simulated mass-weighted large-scale steering flows between the 850 and 300 hPa vertical levels. Overall, the projected future changes in large-scale steering flows are markedly different from those reported by Wu and Wang (2004), who reported that easterly (westerly) anomalies dominated in the tropics (mid-latitudes). In the future projection, the easterly flows are significantly weakened south of 20 °N and east of 130 °E, which is consistent with the changes in TC translation vectors shown in Fig. 5.6. The red (blue) contours in Fig. 5.7 show departures of seasonal mean geopotential height at 500 hPa from the global mean for the GW (PD) run. The western Pacific subtropical high retreats eastward in the GW run compared with the PD run, causing anomalous cyclonic steering flows over the WNP. Interestingly, the projected

westerly changes in steering flows in the lower latitudes are similar to observed changes between periods 1951–1979 and 1980–2001 (Ho et al., 2004), despite a difference in the shift of subtropical high. However, an observed period of 50 years may be too short to distinguish global-warming trend and natural variability.

Figure 5.8a shows projected future changes in TGF during the peak season. Overall, the spatial distributions of seasonal mean changes in TGF (Fig. 5.8) show a strong connection with those in TCF (Fig. 5.4e), especially over the South China Sea and Philippine Sea, suggesting a close linkage between TGF and TCF.

5.5.2 TCF changes projected by a trajectory model

Changes in steering flows and TC genesis locations affect future changes in TCF pattern. To clarify the relative roles of these factors in determining TCF changes, this study applied a simple trajectory model proposed by Wu and Wang (2004). In this model, a TC is treated as a point vortex that moves according to climatological mean TC translation vectors, given its genesis location. TC tracking is performed every 6 hour. The search for movement direction and speed is halted over the grid point of an undefined TC translation vector in the case that the number of TCs sampled is less than 15. Figure 5.9a shows TCF changes projected by the trajectory model. Overall, the spatial patterns of the TCF changes are similar to those yielded by direct TC detection (Fig. 5.4e).

Based on the above result, this study performed two parametric experiments. The first was designed to access the impact of TC translation vectors on TCF changes, in which the same TC genesis locations were used but TC translation vectors south of 20 °N were different between the present and future runs (Fig. 5.9b). Overall, the experiment shows a considerable east-west contrast in the TCF. The second experiment was designed to assess the impact of TC genesis locations on TCF changes, in which different TC genesis

locations were used but the TC translation vectors were the same between the present and future runs (Fig. 5.9c). An east-west contrast in TCF changes is apparent, especially at lower latitudes south of 25 ℕ. Overall, it can be concluded that basin-wide TCF changes were affected by both changes in steering flows and TC genesis locations. Steering-flow changes at lower latitudes appear to hinder westward TC motions, resulting indirectly in TCF changes north of 25 ℕ. In contrast, the changes in TC genesis locations had a strong, direct affect on TCF spatial patterns. In the following section, the mechanisms of changes in TC genesis are focused.

5.6 Mechanisms of the future changes in TC genesis

This section investigates the mechanisms of future changes in TC genesis, based on a modified version of the GPI. As discussed in Section 4.1.2 that the existence of TCs may directly affect the seasonal mean of vertical velocity and other terms in the GPI in case of a TC-resolving model. The vertical velocity term in the GPI is associated with existence of deep convection in the model; therefore, when there are many TCs on a grid in a month, there will be a signal in the vertical velocity. In this case, the GPI is more a diagnostic of existing TCs than a predictor of TC genesis potential. In the NA study, the author assumed that the impact of TC existence on mean state may be small given the fact that on average only 9 TCs occurring during the 4-month peak season. However, in the WNP, given the fact that on average 20 TCs occurring during the 4-month peak season, it is possible that the computed GPI reflects the existing TCs. In this study, the monthly mean fields were reconstructed by filtering out the grid where there are some TCs in a month. Because the conclusions described below are not much different between the non-filtered and filtered GPI (data not shown) so that the discussions below are based on the results obtained by the non-filtered GPI.

Figure 5.8b shows future changes in GPI. A comparison with the future changes in TGF (Fig. 5.8a) indicates that the GPI performs well in reflecting the changes (the spatial correlation is 0.55); however, the GPI changes do not perfectly agree with the TGF changes at north of 22.5 °N. Although there is room for further improvement in GPI analysis, the GPI can be used to identify those GPI elements that make the greatest contribution to future change.

Figure 5.10 shows the total future change in the GPI during the peak season of July–October (Fig. 5.10a), as well as GPI changes obtained by varying each individual GPI element (Fig. 5.10b–f). Note that the summation of changes in the variational GPIs is generally equivalent to the total GPI change (Murakami and Wang, 2010).

The MPI (Fig. 5.10d) is one of the factors causing an increase in GPI for the entire WNP. Here, this study investigates which elements in Eq.4.2, defined in Section 4.1.2, were responsible for the future increase in MPI, and found that among the MPI elements, $CAPE^*$ was the largest contributor to the increase in MPI (data not shown). The $CAPE^*$ is determined mainly by SST, indicating that an increase in SST is primarily responsible for the increase in MPI. In general, the effects of relative humidity (Fig. 5.10c) and MPI (Fig. 5.10d) tend to cancel each other out, meaning that thermodynamic changes have less influence on TGF changes. Similarly, Chan and Liu (2004) and Chan (2009) reported that because thermo-dynamical conditions for TC genesis are largely satisfied in the tropical WNP, dynamical variations are more important in explaining variations in TC genesis. The sign of GPI contribution is different among the GPI elements, e.g., vertical shear and potential intensity act to increase GPI, whereas relative humidity and vertical motion work to decrease it. The reduction in the basin-scale TC genesis number seems to reflect a reduction in large-scale ascending motion accompanied by a reduction in relative humidity. The changes in mid-tropospheric relative humidity and vertical motions seem to be related each other, with regions of anomalous descent (ascent) showing relative

drying (moistening)-a relationship consistent with anomalous advection of drier (moister) air from above (below) (Vecchi and Soden, 2007c).

Vecchi and Soden (2007b) reported that in most IPCC AR4 models, tropical overturning circulation decreases as the climate warms. Furthermore, the authors noted that the weakening is more dominant in the zonally asymmetric (i.e., Walker) component than in the zonal-mean (i.e., Hadley) component of the tropical circulation. The projections in this study are consistent with these findings, as the author found a weakening in overturning circulation (by about 10–12%) toward the end of the 21st century and a more pronounced weakening in the zonally asymmetric component. The decrease in ascending branch of tropical overturning circulation, accompanied by the decrease in relative humidity, appears to be the main reason for a reduction in total TC formations in the WNP, despite local increases in SST (Sugi and Yoshimura, 2004).

For western WNP (WWNP; as outlined in Fig. 5.10), the genesis potential shows a marked decrease, due mainly to decrease in vorticity and vertical motions accompanied by reduced relative humidity. In contrast, an increase in genesis potential occurs in southeastern WNP (SEWNP; as outlined in Fig. 5.10) despite the unfavorable environment for the entire WNP, due to increased low-level vorticity (Fig. 5.10b) and reduced vertical wind shear (Fig. 5.10e).

This study examined the causes of these dynamical changes in this region. Figure 5.11a–b shows the July–October mean spatial distributions of the streamline at 850 hPa (red lines) and vertical motion at the 500 hPa (blue shading), as well as future changes (Fig. 5.11c). Figure 5.11d also shows future changes in relative vorticity at 850 hPa (shading) and vertical wind shear (contours) between 850 and 200 hPa. Future changes in vertical motions (Fig. 5.11c) involve enhanced upward motion north of the equator in the central and eastern Pacific (region E in Fig. 5.11c). West of the enhanced upward

motion, low-level cross-equatorial flows are intensified in the western Pacific (region F). Moreover, low-level cyclonic vorticity (vertical wind shear) is increased (reduced) in the southeastern quadrant of the WNP (region G in Fig. 5.11d). These dynamical changes appear to result from a Rossby wave response induced by equatorially antisymmetric heating (as indicated by upward motion) (Gill, 1980); i.e., anomalous cyclonic circulation and northward cross-equatorial flows occur west of the heated regions. The Rossby wave response generates anomalous lower-level positive vorticity, extending the monsoon trough eastward. As evidence of this process, the monsoon trough in the WNP in the GW run (C–D in Fig. 5.11b) extends farther east than that in the PD run (A–B in Fig. 5.11a). Because the monsoon trough generally accompanied by weak vertical wind shear (region G in Fig. 5.11d; Gray, 1968; Chia and Ropelewski, 2002; Sun and Ding, 2002), eastward extension of the monsoon trough affects the southeastern quadrant of the WNP basin by providing a favorable dynamical environment for TC generation. In the western WNP, a negative tendency in relative vorticity can be also seen (Fig. 5.11d), although this makes a minor contribution to the decrease in genesis potential (Fig. 5.10c). This anomalous negative vorticity may also result from a dynamical response induced by a reduction in diabatic heating in southeastern Philippine Sea (region F, Fig. 5.11c).

The response of the heating over the equatorial central Pacific appears to be strongly related to the prescribed future anomaly in SST (Fig. 5.12a). Over the Pacific, future changes in SST show strong warming in the equatorial central Pacific and subtropical North Pacific, whereas relatively weak warming occurs in the subtropical South Pacific. The resulting thermal contrast between the South and North Pacific results in enhanced cross-equatorial flows in the western Pacific. In addition, the distribution of tropical precipitation changes (Fig. 5.12b) is strongly correlated with the distribution of tropical SST changes (Fig. 5.12a). This conclusion has also been reported by Vecchi and Soden (2007a), Sugi et al. (2009), Xie et al. (2010), and Murakami and Wang (2010), indicating that the spatial distribution of tropical SST changes may be a key factor in

determining future changes in TGF.

5.7 Summary

The present-day (PD) simulation demonstrates that the 20-km-mesh MRI/JMA AGCM performed reasonably well in simulating the climatological mean, seasonal cycle and interannual variations of TC activity over the western North Pacific (WNP). Variations in the spatial distribution of TC genesis between El Niño years and La Niña years were well simulated in the southeastern quadrant of the WNP, revealing an increase (decrease) in Genesis Potential Index (GPI) and detected TC generation during El Niño (La Niña) years.

Concerning future change, the basin-wide TC genesis number (total frequency of occurrence) shows a 13.2% (7.7%) decrease in the GW simulation for the peak season (July–October) and a 22.7% (22.6%) decrease for all seasons (statistically significant at the 95% level). Seasonal variation in TC genesis number showed no significant future change except for a decrease in autumn and early winter.

Future changes in TC frequency of occurrence (TCF) showed spatial variations. An overall belt of decrease extends from the central WNP (15 °N, 140 °E) to the east of Taiwan (25 °N, 125 °E). An belt of substantial increase is seen immediately east of the decreasing belt. These changes indicate that most future TCs will tend to travel along a more eastward course than that of the present day. Consequently, the frequency of TCs decreased in coastal regions, showing a significant reduction in Southeast Asia (by 44%), and reductions (by 9%–25%) in the Philippines, East Japan, West Japan, Korea, and South China. However, the frequency of TCs increased (by 34–58%) in Central-North Chinese coastal region due to a local increase in TC genesis. Future changes in the number of TC

landfalls were not statistically significant.

The cause of the changes in the TCF is investigated in terms of changes in steering flows and genesis locations. A comparison of steering flows between the PD and GW simulations revealed no significant change north of 20 °N; but significant westerly flow anomalies were found in the southeastern quadrant of the WNP. Experiments using a trajectory model revealed that significant changes in the steering flows south of 20 °N may directly restrict westward motion of TCs, resulting in changes in TCF. The inhibition of westward TC motion in the tropical WNP also had an indirect effect on TCF north of 25 °N. The author found a marked change in the locations of TC genesis between the PD and GW simulations: TC genesis decreases in the western WNP but increases in the southeastern WNP, consistent with the future change in TCF.

The physical causes of the basin-wide decrease in TC genesis frequency (TGF) and change in genesis locations were further elucidated with reference to the modified version of GPI. The main reason for the decrease in the basin-wide TGF appeared to be weakening of the ascending branch of tropical overturning circulation and reduced tropospheric relative humidity. In turn, these changes are linked to a weakening of the Walker circulation, which is more evident in autumn and early winter. The main factors contributing to the more localized projected future increase in TC genesis in the southeastern WNP are increased lower-level vorticity and reduced vertical wind shear.

The dynamical effects favorable for the increase in TGF in the southeastern WNP appear to have resulted from heating responses in the tropical central Pacific, which act to enhance lower-level vorticity, reduce vertical wind shear, and induce northward cross-equatorial flows. The increased heating over the equatorial central Pacific generally overlaps with the relative SST increase in the future. The enhancement of cross-equatorial flows is also due to inter-hemispheric contrast in the future SST relative changes. These

findings suggest that the mean rising motion tends to decrease throughout the entire WNP in the future global-warmed environment, resulting in a reduced basin-wide frequency of TC genesis. However, even under such unfavorable conditions of the background vertical motions, favorable conditions for TC genesis may arise via the dynamic effects of changes in large-scale flow in the southeastern quadrant of the WNP. Regions of relatively high SST are important not only in terms of their effect on local TC genesis, but also in their effect on large-scale flows , which in turn has a dynamic effect on the environment of TC genesis and TC motions in the WNP.

The projected results are somewhat different from the observed trend in the past decade and the result of past numerical studies when compared with future changes in large-scale flows and TC tracks. For more reliable future projections, multi-decadal ensemble realizations are recommended. The present results suggest that future changes in TC climatology are relatively sensitive to the spatial pattern of relative SST change. This finding indicates that it would be worthwhile to explore the degree of uncertainty in future TC projections by prescribing an SST pattern based on both multi-model ensembles and on results obtained using a range of individual models.

Table 5.1: Accumulated tropical cyclone storm days in nine coastal regions during the July–October season. The off-shore edges of the coastal regions are defined as being 200 km from the coast line. (a) Observations (1979–2003), (b) present-day run (PD, 1979–2003), (c) global-warming run (GW, 2075–2099), (d) future change, and (e) level of statistical significance of the future change (levels less than 90% are not shown).

	(a) Obs (1979–2003)	(b) PD (1979–2003)	(c) GW (2075–2099)	(d) GW – PD	(e) Level of statistical significance of the future change
East Japan	44.0	65.5	53.8	–1.3 (–17.3%)	–
West Japan	124.0	119.0	95.5	–23.5 (–19.7%)	–
Korea	31.3	34.3	25.8	–8.5 (–24.8%)	–
North China	15.0	18.5	24.8	+6.3 (+33.8%)	–
Central China	53.0	32.5	51.3	+18.8 (+57.7%)	–
South China	194.0	147.3	134.0	–13.3 (–9.0%)	–
Taiwan	70.0	55.5	59.5	+4.0 (+7.2%)	–
Southeast Asia	40.5	94.8	53.5	–41.3 (–43.5%)	99%
Philippines	145.0	66.8	51.3	–15.5 (–23.2%)	–

Table 5.2: As for Table 5.1, but for the average instantaneous maximum wind velocity (ms^{-1})

	(a) Obs (1979–2003)	(b) PD (1979–2003)	(c) GW (2075–2099)	(d) GW – PD	(e) Level of statistical significance of the future change
East Japan	27.9	20.9	22.4	+1.5 (+7.4%)	95%
West Japan	35.9	23.4	25.1	+1.7 (+7.2%)	95%
Korea	28.0	20.0	20.4	+0.4 (+1.8%)	–
North China	24.8	15.2	15.8	+0.7 (+4.4%)	–
Central China	29.0	17.4	17.6	+0.2 (+1.1%)	–
South China	28.8	16.5	17.8	+1.2 (+7.4%)	99%
Taiwan	35.6	20.1	20.3	+0.2 (+1.0%)	–
Southeast Asia	27.5	16.6	17.5	+1.0 (+5.8%)	90%
Philippines	24.5	17.7	19.2	+1.5 (+8.7%)	95%

Table 5.3: As for Table 5.1, but for July–October mean number of landfalling tropical cyclones.

	(a) Obs (1979–2003)	(b) PD (1979–2003)	(c) GW (2075–2099)	(d) GW – PD	(e) Level of statistical significance of the future change
East Japan	0.60	0.44	0.44	+0.00 (0.0%)	–
West Japan	1.24	0.64	0.60	–0.04 (–6.3%)	–
Korea	0.76	0.32	0.28	–0.04 (–12.5%)	–
North China	0.12	0.12	0.12	+0.00 (0.0%)	–
Central China	0.72	0.36	0.44	+0.08 (+22.2%)	–
South China	4.40	1.64	1.68	+0.04 (+2.4%)	–
Taiwan	1.16	0.36	0.48	+0.12 (+33.3%)	–
Southeast Asia	0.52	0.80	0.52	–0.28 (–35.0%)	–
Philippines	1.96	0.40	0.36	–0.04 (–10.0%)	–

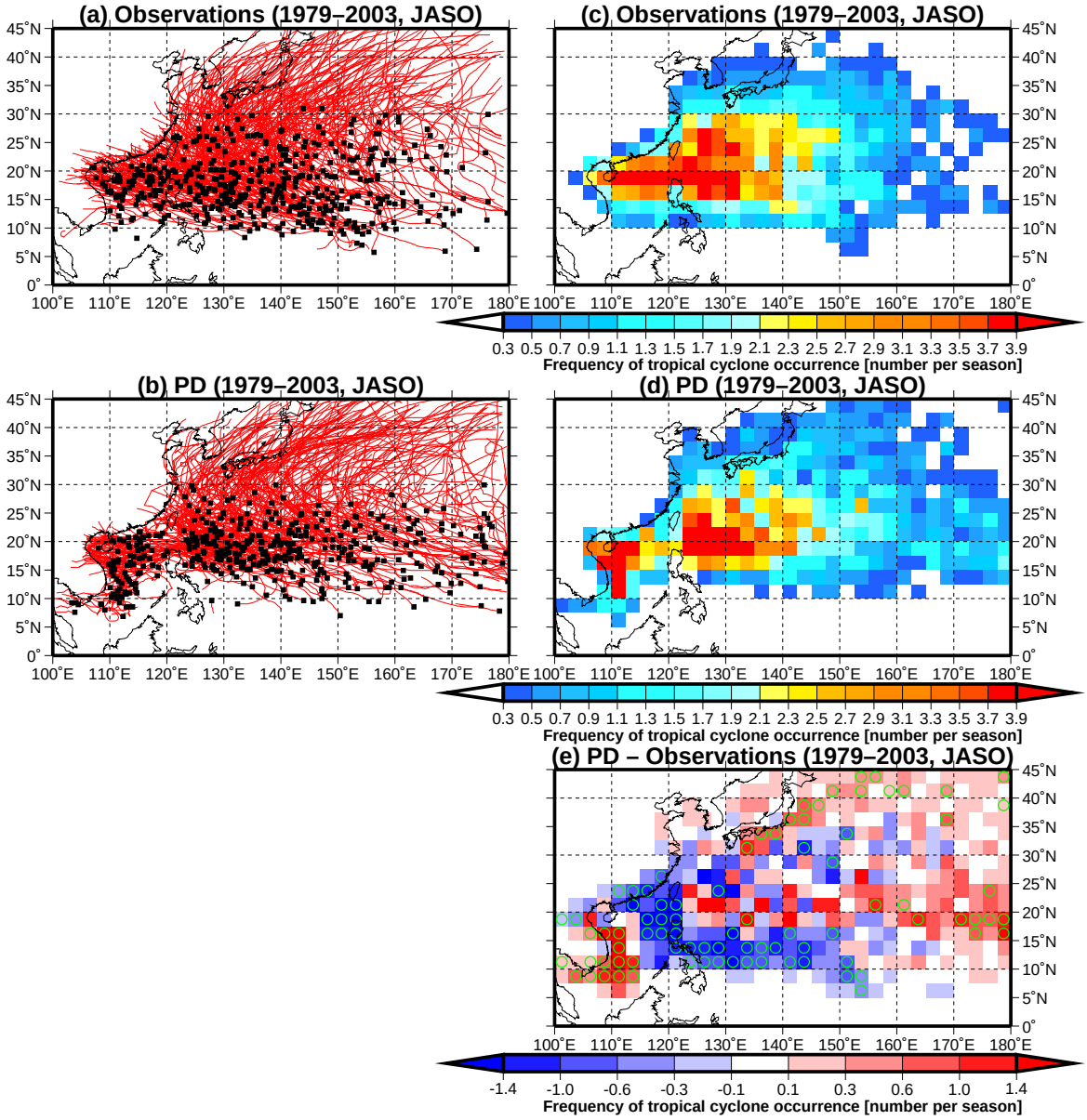

Figure 5.1: Total tropical cyclone (TC) tracks (a–b) and TC frequency of occurrence (c–e) during July–October (JASO) from 1979 to 2003 in the western North Pacific. (a) and (c) show observed data, while (b) and (d) show data from the present-day run (PD). The difference in frequency of TC occurrence between the PD run and observations is shown in (e). Black dots in (a) and (b) show TC-genesis locations. Green circles in (e) indicate that the difference is statistically significant at the 90% level.

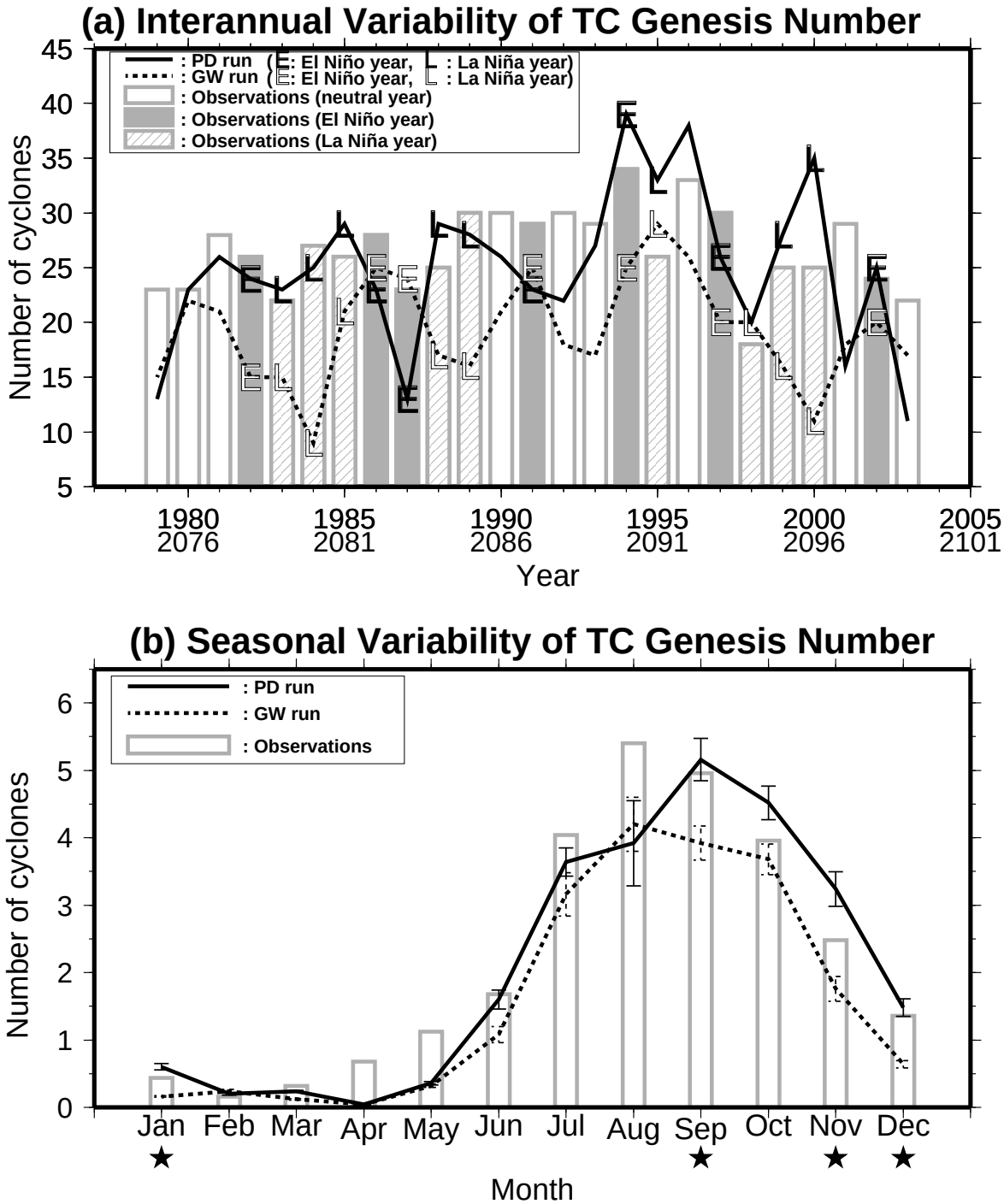

Figure 5.2: (a) Yearly and (b) seasonal variability in the number of generated tropical cyclones, based on observations (1979–2003; histogram), the present-day run (PD; 1979–2003; solid black line), and the global-warming run (GW; 2075–2099; dotted black line). The correlation coefficient for yearly TC number between the PD run and observations is 0.55, which is statistically significant at the 95% level. The average TC frequencies are 26.6 (observed), 25.0 (PD run), and 19.3 (GW run). The letter "E" ("L") in (a) indicates an El Niño (La Niña) year, and stars at the base of (b) indicate a statistically significant difference between the GW and PD runs at the 95% level. The error bars in (b) show two-sided 95% confidence interval for each GW (dashed) and PD (solid) run.

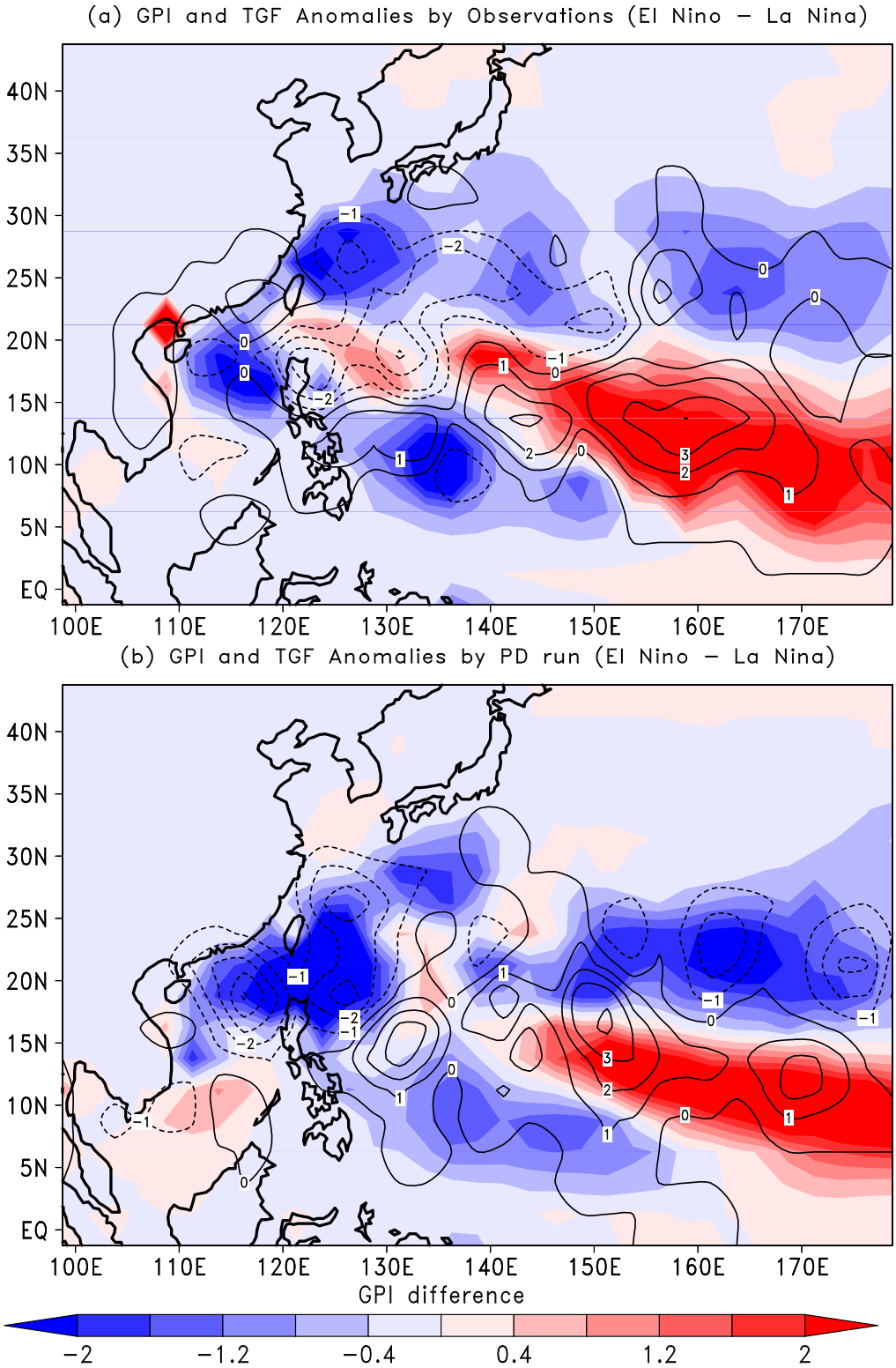

Figure 5.3: Mean differences in TC genesis frequency (TGF; contours) and Genesis Potential Index (GPI; hatching) between El Niño and La Niña years during the period of July–October (JASO) obtained from (a) the best-track data and (b) the present-day run. Unit is one standard deviation normalized by spatial variation. The observed GPI was computed from JRA-25 reanalysis dataset (Onogi et al., 2007). El Niño (La Niña) years are defined as 1982, 1986, 1987, 1991, 1994, 1997, and 2002 (1983, 1984, 1985, 1988, 1989, 1995, 1998, 1999, and 2000)

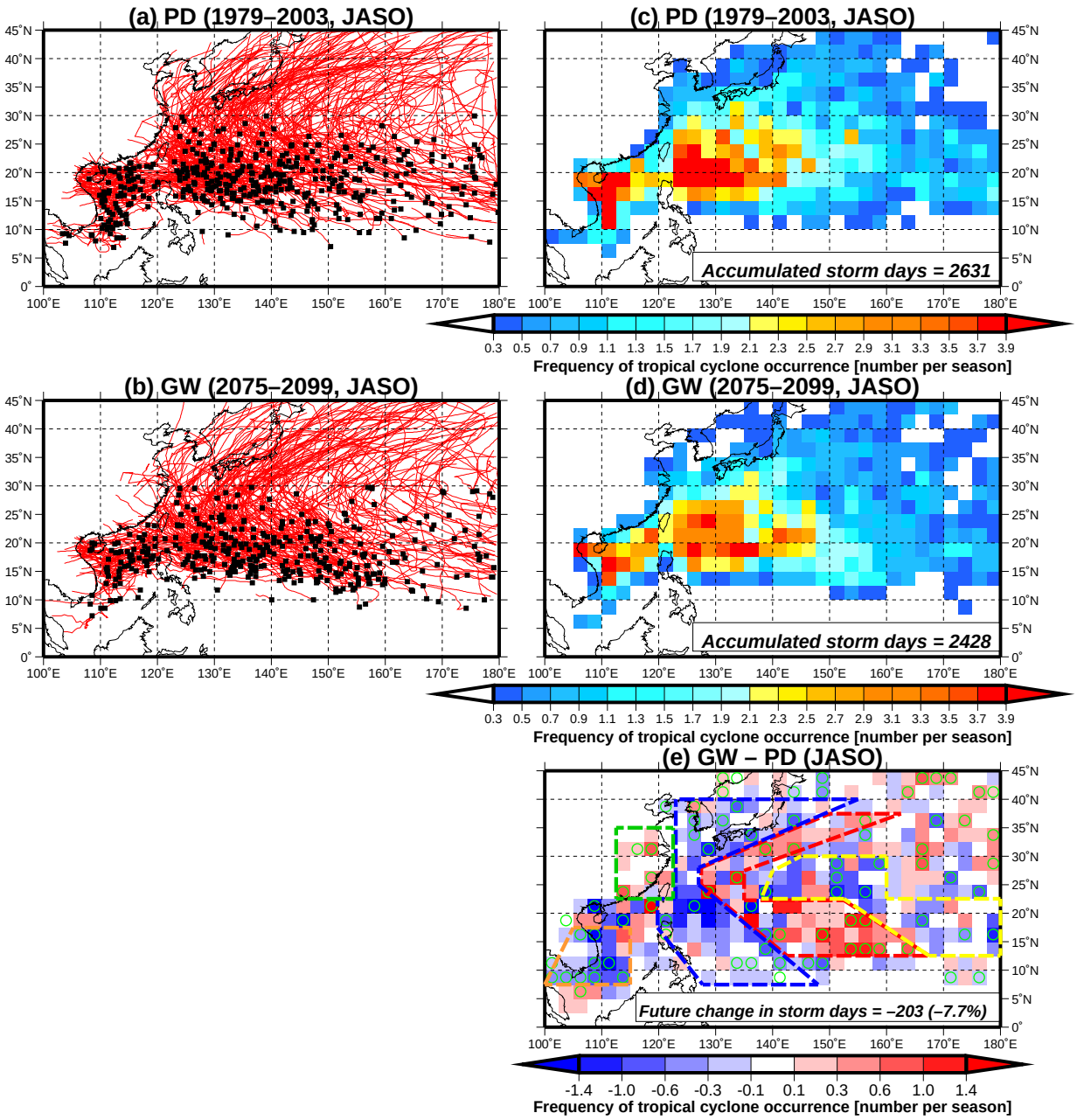

Figure 5.4: As for Fig. 5.1, but for (a, c) the present-day run (PD), (b, d) the global-warming run (GW), and (e) the difference between the runs (GW minus PD). The dashed regions in (e) are explained in the text. Accumulated storm days and their future change are noted at the bottom of (c)–(e).

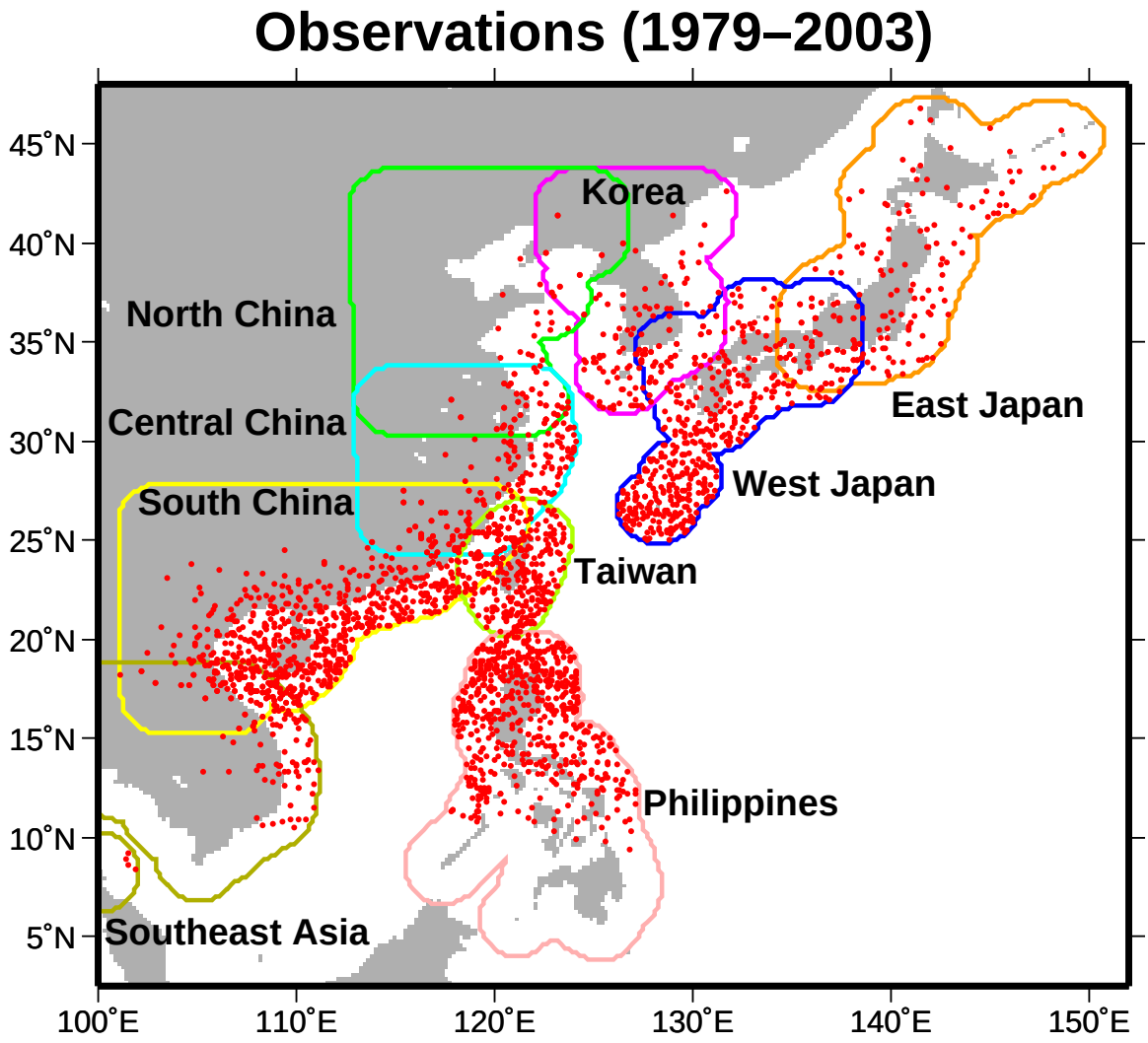

Figure 5.5: Observed TCs in the nine coastal regions during July–October (JASO) of 1979–2003, as derived from 6-hourly data. Red dots show the locations of TCs.

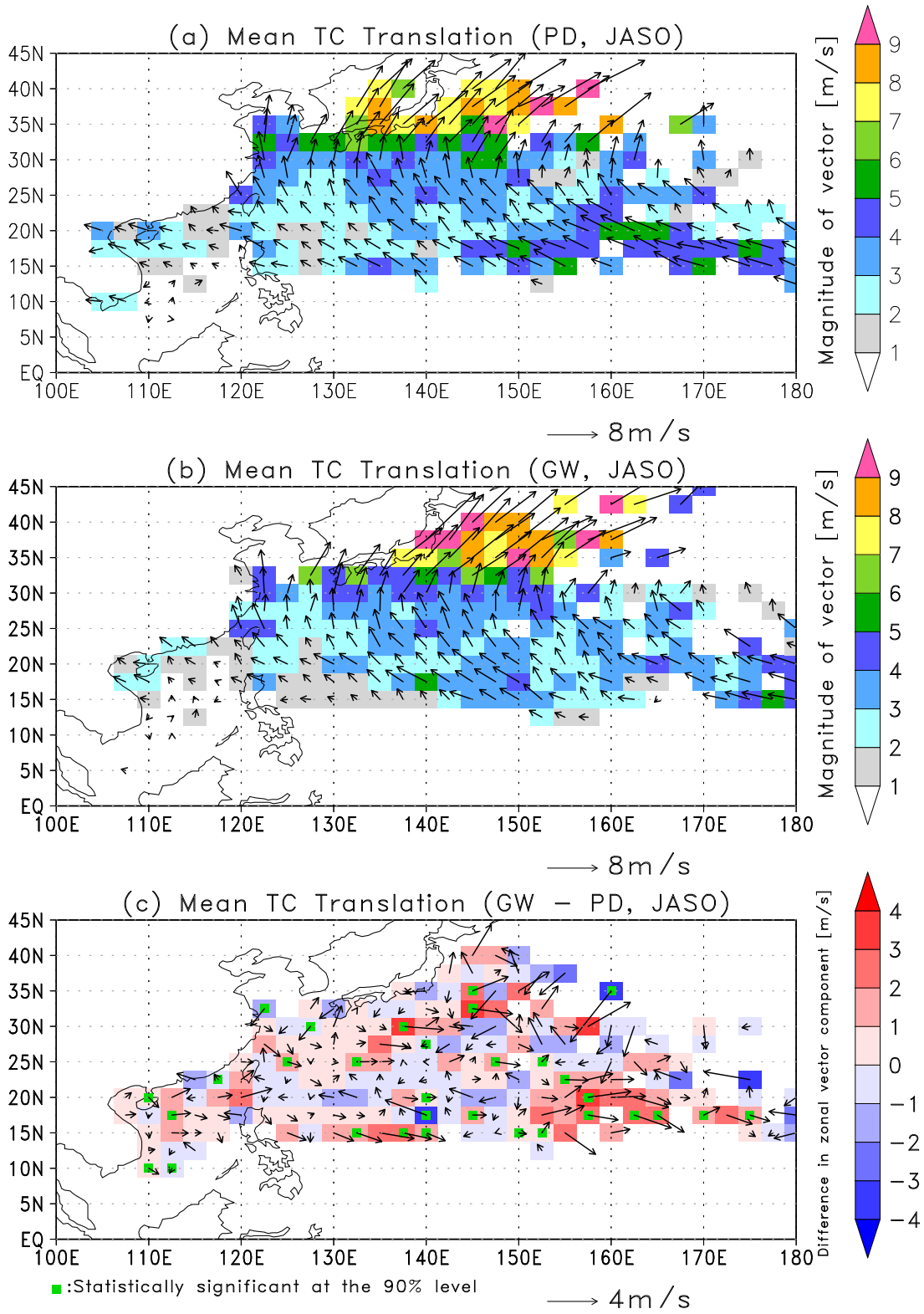

Figure 5.6: Simulated mean TC translation vectors and magnitudes (ms^{-1}) for the peak TC season of July–October (JASO) for (a) the present-day run (PD), (b) the global-warming run (GW), and (c) the difference between the GW and PD runs. Data are only shown for grid with more than 15 storms. Green dots in (c) indicate that the vector difference of either the zonal or meridional component is statistically significant at the 90% level. Color shading in (c) indicates difference in the zonal vector component.

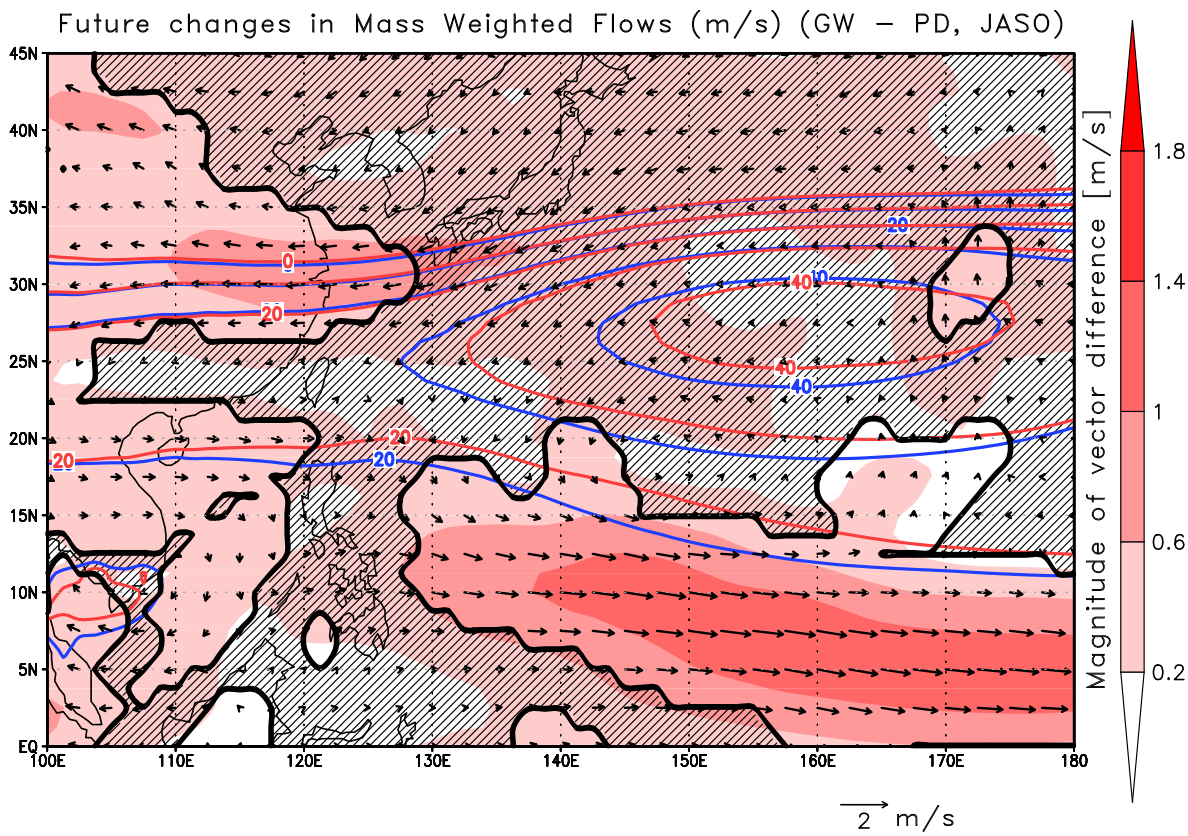

Figure 5.7: Simulated future changes in mass-weighted flows (vectors, ms^{-1}) and departures of mean geopotential height at 500 hPa (colored contours, *gpm*) for the peak season of July–October (JASO) in the western North Pacific. Black hatching indicates that the vector differences of both the zonal and meridional component are not statistically significant at the 90% level. The departure of geopotential height is computed as the difference from global mean for the PD (blue contours) and GW (red contours) runs. Only positive departures are shown, with interval of 10 *gpm*. The global mean of geopotential height is 5,852 (5,916) *gpm* for the PD (GW) run.

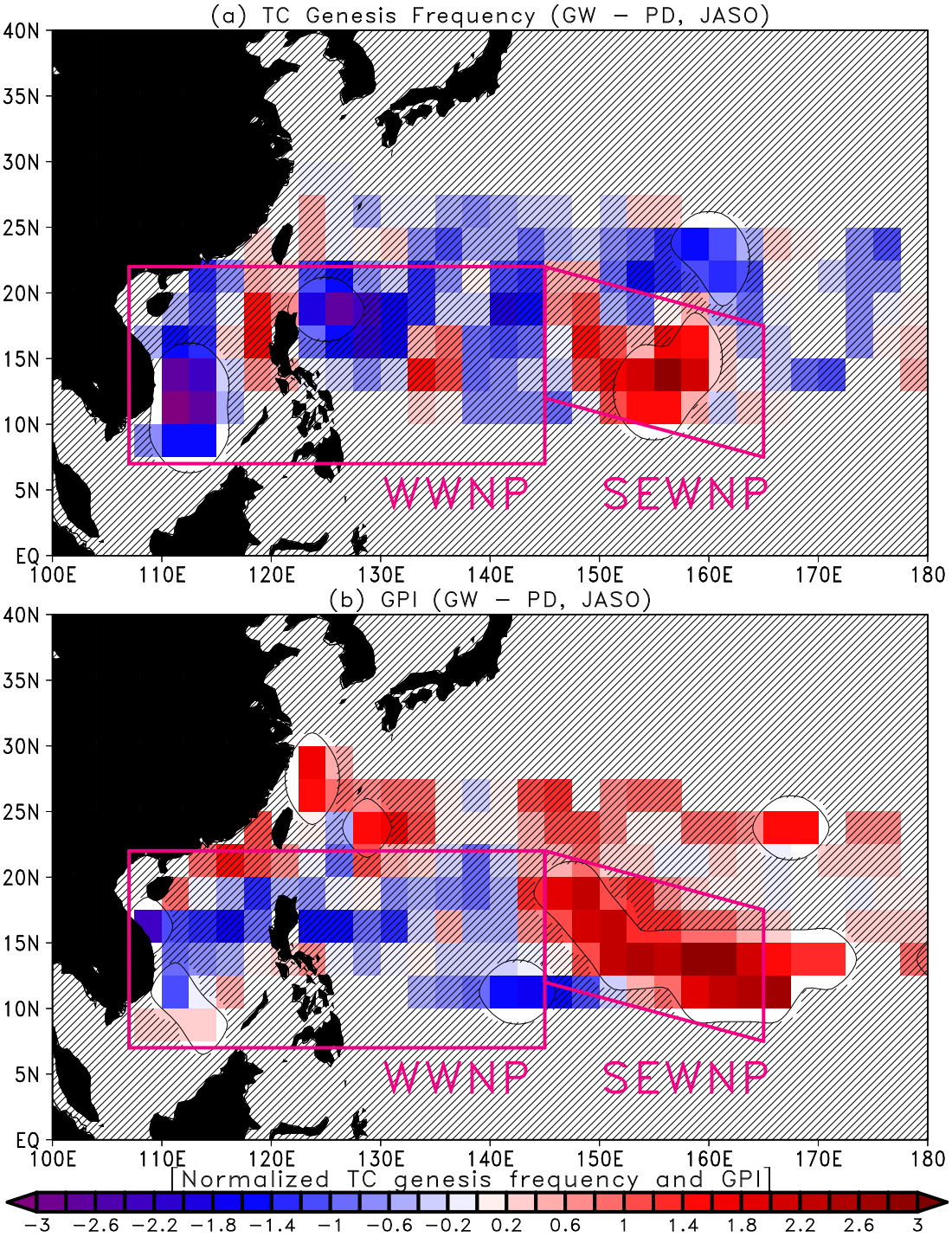

Figure 5.8: (a) Future change in the averaged genesis frequency of tropical cyclones for July–October (JASO) in the western North Pacific (WNP). (b) As for (a), but for future change in Genesis Potential Index (GPI). The GPI is filtered out where both present and future climatological mean TGFs are zero. Unit is one standard deviation normalized by spatial variations. Black hatching indicates that the decrease or increase is not statistically significant at the 90% level. Outlined regions are western WNP (WWNP) and southeastern WNP (SEWNP) which show marked future changes.

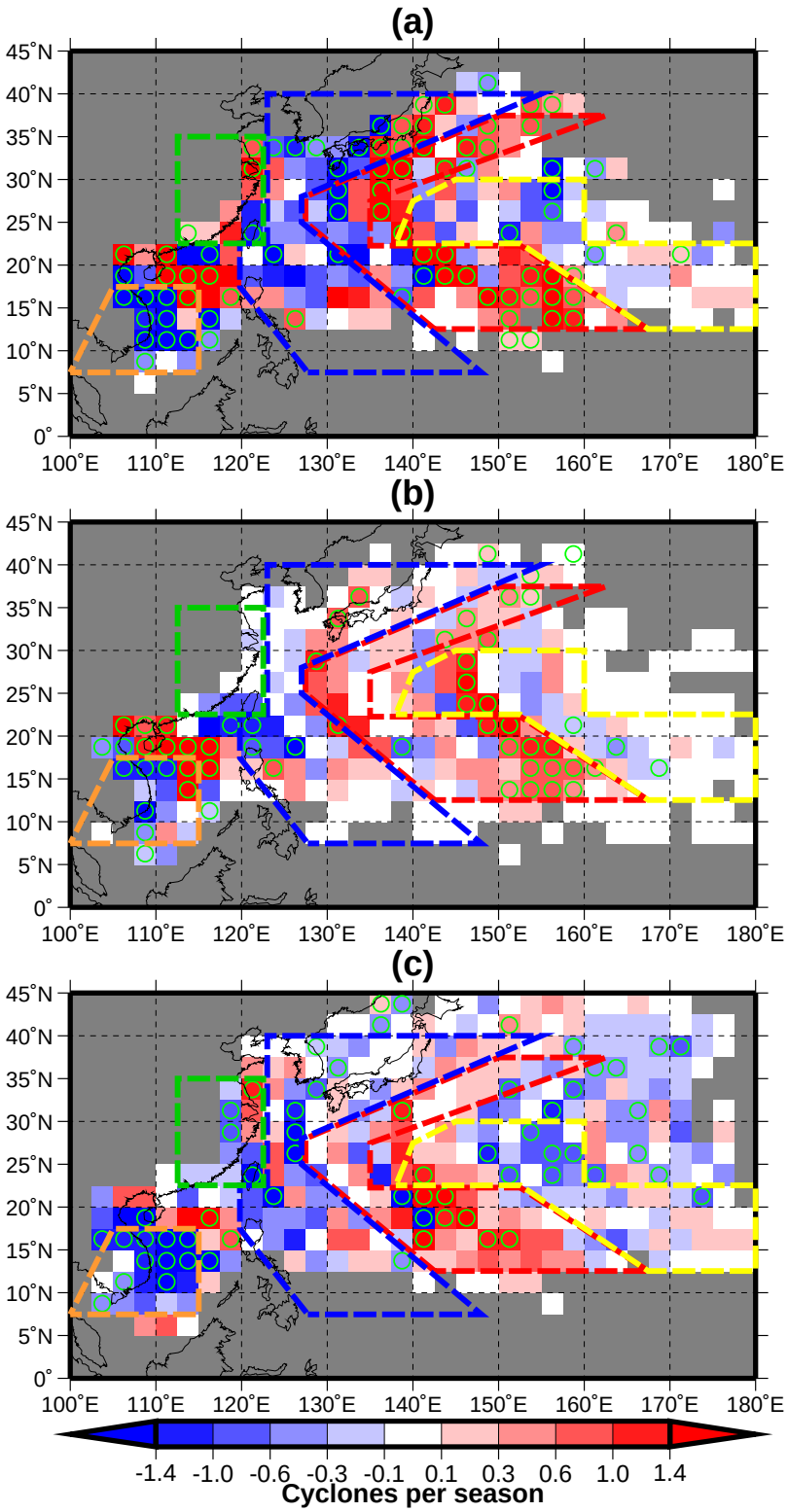

Figure 5.9: (a) Future change in tropical cyclone frequency (TCF) projected by the trajectory model which used different TC translation vectors and genesis locations obtained from the PD and GW runs. (b) the same as in (a) but only different TC translation vectors south of 20 ℕ were used to assess the impact of the translation vectors; and (c) the same as in (a) but only different TC genesis locations were used to assess the impact of TC genesis location. The dashed areas indicate significant changes in TCF shown in Fig. 5.4.

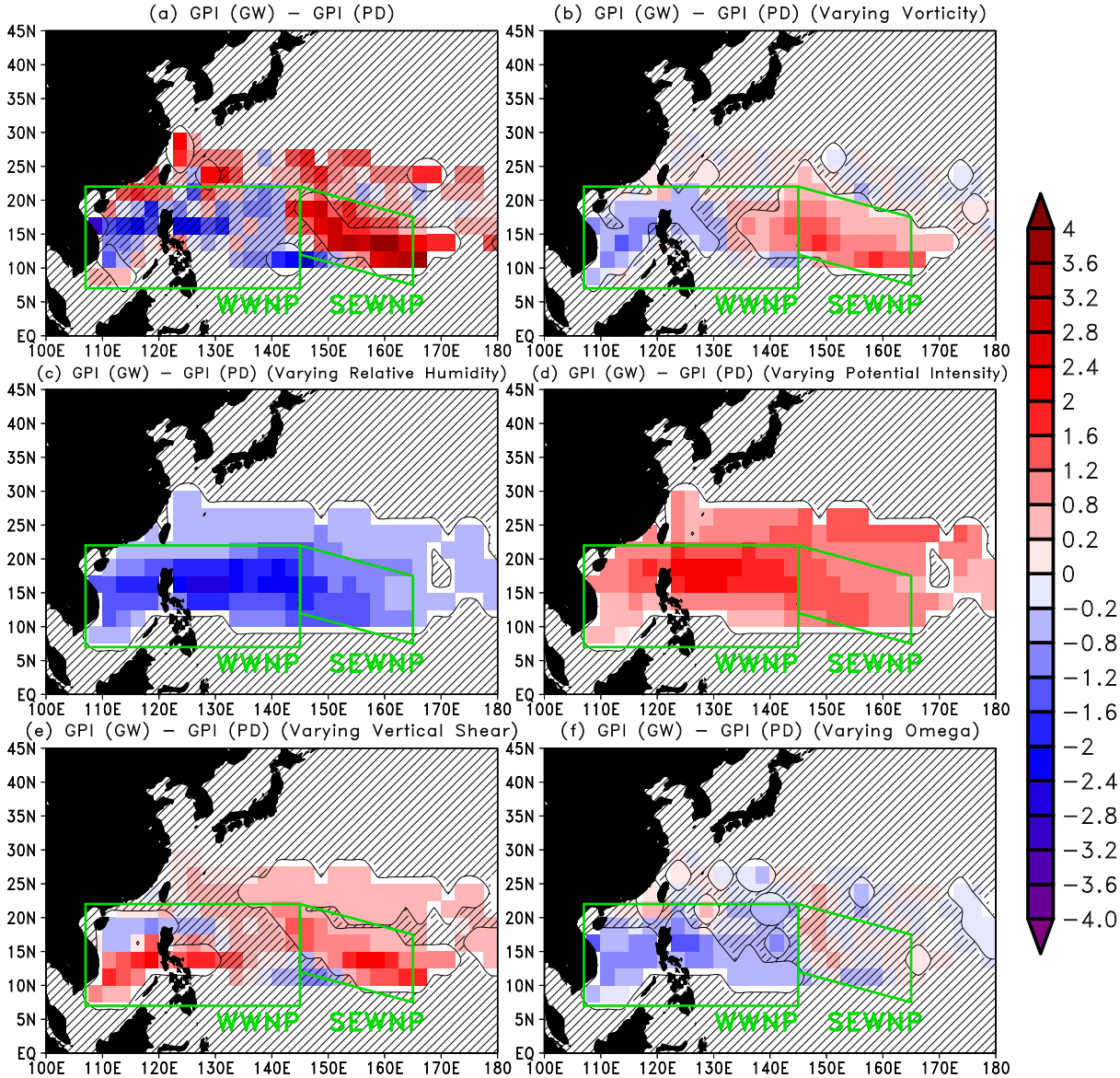

Figure 5.10: Future change in the Genesis Potential Index (GPI) during July–October (JASO) over the western North Pacific (WNP) for (a) the difference in GPI between the global-warming (GW) and present-day (PD) runs, and for GPI changes induced by each individual factor: (b) vorticity, (c) relative humidity, (d) maximum potential intensity, (e) vertical wind shear, and (f) vertical motion. Black hatching indicates that the decrease or increase is not statistically significant at the 90% level. Outlined regions are western WNP (WWNP) and southeastern WNP (SEWNP) which show marked future changes.

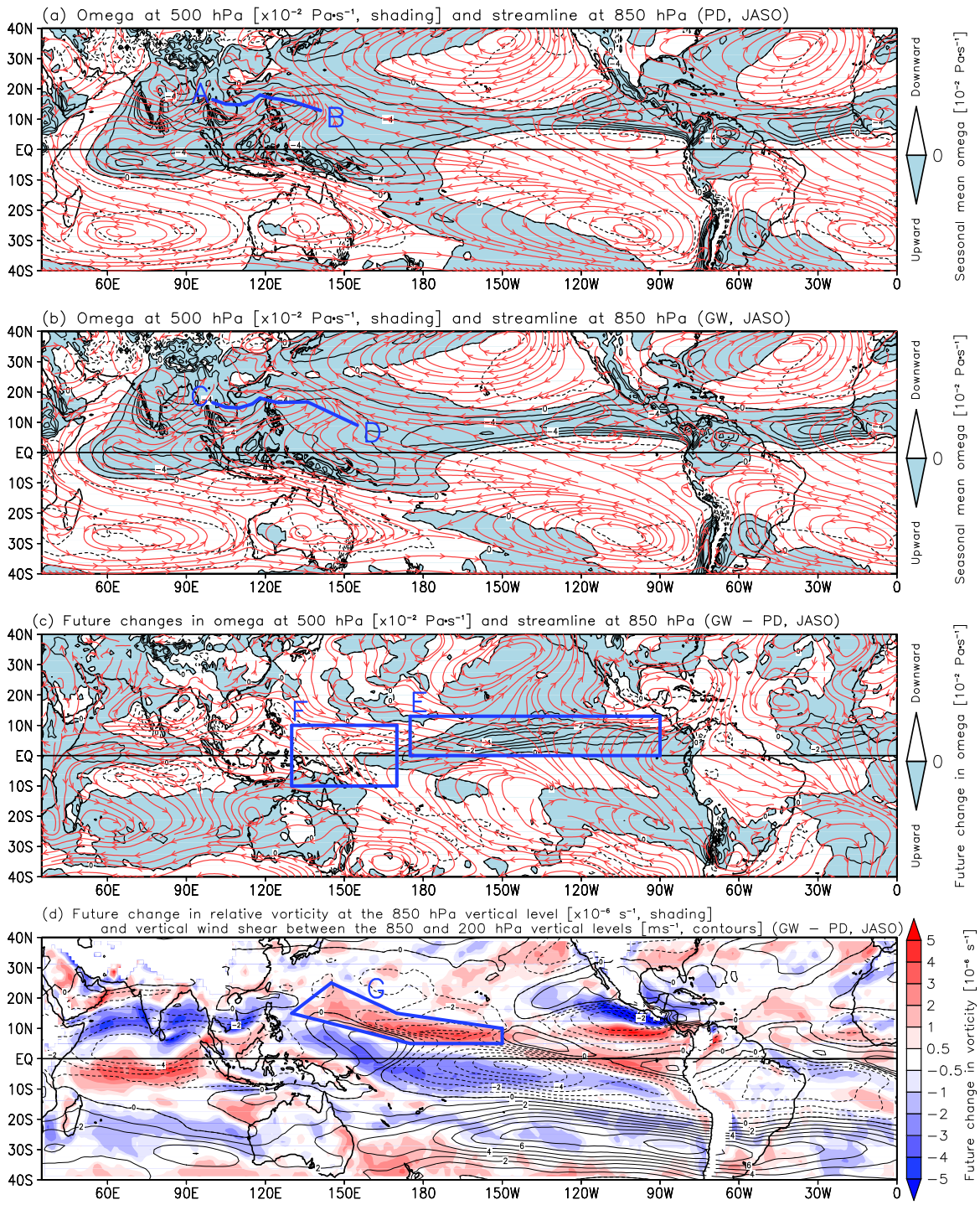

Figure 5.11: July–October (JASO) mean of omega (i.e., vertical wind velocity) at 500 hPa [$10^{-2} Pa \cdot s^{-1}$, contours] and streamline at the 850 hPa for (a) the present-day run (PD), (b) the global warming run (GW), and (c) the difference between the GW and PD runs. Dashed contours show positive omega (i.e., descending motion), whereas solid contours with blue shading show negative omega (i.e., ascending motion). (d) shows future changes in relative vorticity at the 850 hPa [$10^{-6} s^{-1}$, shading] and vertical wind shear between the 850 and 200 hPa [ms^{-1}, contours]. Dashed (Solid) contours in (d) indicate reducing (increasing) vertical wind shear. Regions outlines by blue lines with symbols are described in the text.

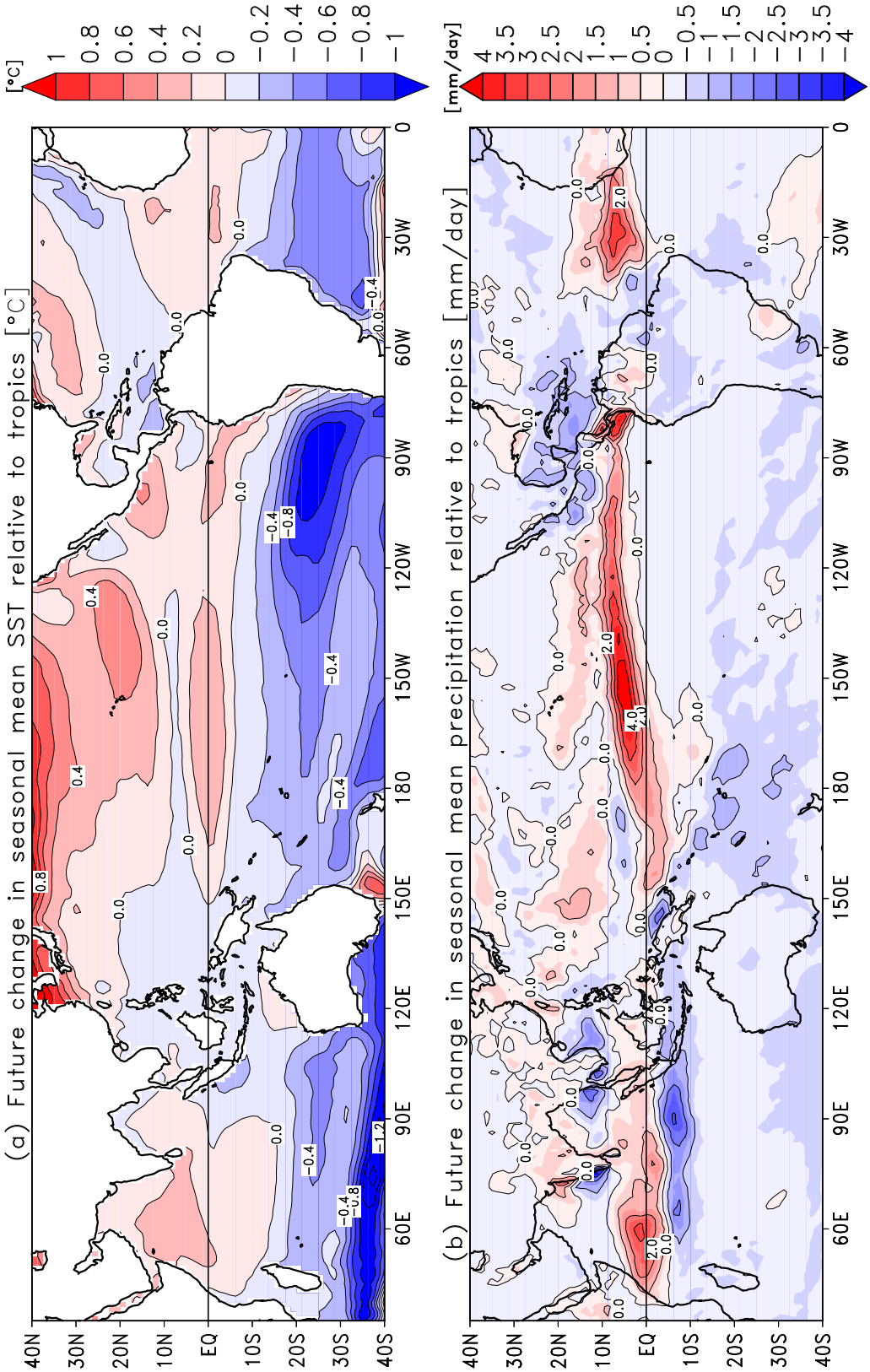

Figure 5.12: (a) Future change in seasonal mean prescribed SST [℃] relative to global tropics (20 ℃S–20 ℃N) for the peak cyclone season of July–October (JASO). (b) As for (a), but for precipitation [mm/day]. The tropical mean of SST is 26.9 (29.0) ℃ for the present-day (global-warming) run, whereas that of precipitation is 4.61 (4.95) mm/day.

Chapter 6

Conclusions

This study investigated performance of medium-range predictions, present-day climate projections, and possible future changes regarding tropical cyclones (TCs) using the Meteorological Research Institute (MRI)/Japan Meteorological Agency (JMA) 20-km mesh super high-resolution Atmospheric General Circulation Model (MRI/JMA-AGCM), whose horizontal resolution is so far the highest among state-of-the-art climate models in the world.

Comparisons with coarser resolution models revealed marked superiority for the 20-km mesh AGCM. Twelve tropical storms between 2002 and 2005 over the western North Pacific (WNP), namely, typhoons, were simulated through medium-range forecast experiments with the 20-km mesh AGCM. These simulations were compared with the 60-km mesh JMA Global Spectral Model (GSM) to evaluate differences in resolution. They are verified with the best-track data as observations. The verification was conducted in terms of estimating error of position, intensifying tendency, radius of 50 knot, 30 knot, and composite wind profile. As a result, the 20-km mesh AGCM showed slightly smaller position error than the GSM. Moreover, much improvement was seen in the intensity prediction. The 20-km mesh AGCM outstandingly can both decrease the central sea level pressure and increase maximum wind velocity, while the GSM can not simulate them because of low resolution. The 20-km mesh AGCM also shows better intensifying and decaying tendency than the GSM. The verifications of 50 knot and 30 knot radii, and the composite wind profile indicate that the typhoon structure by the 20-km mesh AGCM is quite realistic. Moreover, the 20-km mesh AGCM expresses the drastic transformation of inner-core wind profile within 100 km from the typhoon center more realistically than the

GSM. These results indicate that a high resolution global model, such as 20-km mesh, is vital when discussing the intensity and wind profile of tropical storms.

The effect of model resolution on projected climatological features of TCs was also investigated via 25-year present-day and future global warming projections using the MRI/JMA-AGCM with four resolutions ranging from TL95 (180-km mesh) to TL959 (20-km mesh). The finest resolution (TL959) showed the highest skills in terms of TC intensity and interannual and seasonal variations in TC genesis number. Resolutions of TL319 (60-km mesh) and finer showed a significant future increase in the frequency of intense TCs, whereas resolutions coarser than TL319 showed no such change, indicating that TL319 is the critical resolution in projecting future change in the frequency of intense TCs. Overall, high model resolution is preferable for realistic and reliable climate projections. Resolutions of TL159 (120-km mesh) and finer showed similar skills, biases, and future changes in the spatial pattern of TC genesis frequency (TGF) and TC genesis number, indicating the potential use of lower model resolutions for minimizing uncertainties in future changes in the mean state of TGF and TC genesis number.

Based on above promising results yielded by the 20-km mesh AGCM, possible future changes in TC activity over the North Atlantic (NA) and WNP were investigated by comparison of simulations of the present-day climate and future change under the A1B emission scenario using the 20-km mesh AGCM. Two suites of 25-year simulations were conducted for the present-day (1979–2003) and future (2075–2099) climate. For the future projection, the model is driven by the sea surface temperature (SST) that includes a trend projected by most recent Intergovernmental Panel for Climate Change (IPCC) multi-model ensemble and a year-to-year variation derived from the present-day climate.

As to NA projections, the present-day simulation reproduces many essential features of observed climatology and inter-annual variability in TC frequency of occurrence and

tracks. A major finding is that the future change of total TC counts in the NA is statistically insignificant, but the frequency of TC occurrence will decrease in the tropical western NA (WNA) and increase in the tropical eastern NA (ENA) and northwestern NA (NWNA). The projected change in TC tracks suggests a reduced probability of TC landfall over southeast US and an increased influence of TCs on northeast US. The track changes are not due to changes of large-scale steering flows; instead, they are due to changes in TC genesis locations. The increase in TC genesis in ENA arises from increasing background ascending motion and convective available potential energy. In contrast, the reduced TC genesis in the WNA is attributed to decreases in midtropospheric relative humidity and ascending motion caused by remotely forced anomalous descent. This finding indicates that the impact of remote dynamical forcing is greater than that of local thermo-dynamical forcing in the WNA. The increased frequency of TC occurrence in the NWNA is attributed to reduced vertical wind shear and the pronounced local warming of the ocean surface. These TC changes appear to be most sensitive to future change in the spatial distribution of rising SST. Given that most IPCC models project a larger increase in SST in the ENA than in the WNA, the projected eastward shift in TC genesis is likely to be robust.

Regarding WNP projections, the present-day simulation yielded reasonable climatology and interannual variability regarding TC genesis frequency and tracks. The future projection indicates (a) a significant reduction (by about 23%) in both TC genesis number and frequency of occurrence, which occurs primarily during the late part of the year (September to December); (b) an eastward shift in the positions of the two prevailing northward recurving TC tracks during the peak TC season (July–October); and (c) a significant reduction (by 44%) in TC frequency approaching coastal regions of Southeast Asia. The changes of TC tracks and occurrence frequency in the coastal regions are partially due to changes in large-scale steering flows which hinder westward TC motion at lower latitudes, but mainly due to changes in TC-genesis locations: Fewer TCs will

form in the western portion of the basin (west of 145 °E), whereas more storms will form in the southeastern quadrant of the WNP (10–20 °N, 145–160 °E). Analysis of a Genesis Potential Index reveals that the reduced TC genesis in the western WNP is mainly due to *in situ* weakening of large-scale ascent and decreasing mid-tropospheric relative humidity, which are associated with enhanced descent of the tropical overturning circulation, especially the Walker circulation. The analysis also indicates that enhanced TC genesis in the southeastern WNP is due to increased low-level cyclonic vorticity and reduced vertical wind shear. These favorable dynamical conditions are associated with the reinforced cross-equatorial flows in the western Pacific that are induced by differential warming rates in the two hemispheres (the Northern Hemisphere warms faster than the Southern Hemisphere). These changes appear to be critically dependent on the spatial pattern of future sea surface temperature.

Although above results seem to be considerably reliable because of the high resolution, it must be cautious that they are just one example of future projections using one model and one lower boundary condition. The author recently investigated that the different cumulus parameterizations yielded the different future changes in TC number in some ocean basins. Resent studies reported by Sugi et al. (2009) and Zhao et al. (2009) also suggest that the different SST forcings resulted in the different future changes in TC genesis number in some ocean basins. These results suggest that there still remains uncertainty regarding future changes in TC climatology in an ocean basin. In order to reduce the uncertainties, it is necessary to conduct multi-physics and multi-SST ensemble projections using high resolution models. In case of different results among the projections, it is important to interpret what causes the differences. This leads to new insight of physical mechanisms of TC genesis and the future changes which are so far considered as challenging tasks.

Acknowledgements

The author would like to express special gratitude to Prof. Hiroshi L. Tanaka of the University of Tsukuba, for advising this dissertation. The author is deeply grateful to Prof. Bin Wang (University of Hawaii), Prof. Fujio Kimura (JAMSTEC), Prof. Akio Kitoh (MRI), Prof. Hiroaki Ueda (University of Tsukuba), Prof. Hiroyuki Kusaka (University of Tsukuba), Dr. Masato Sugi (JAMSTEC), Dr. Takayuki Matsumura (JMA), and Dr. Ryota Sakai (JMA) for their helpful suggestions, comments, and encouragements.

My deepest appreciation also goes to Prof. Kevin Hamilton (University of Hawaii) for his support of my short stay in Hawaii for our collaborations for this study.

Discussions with Prof. Yuqing Wang (University of Hawaii), Prof. Raghavan Krishnan (Indian Institute of Tropical Meteorology), Prof. Tianjun Zhou (LASG/IAP, Chinese Academy of Sciences), Prof. In-Sik Kang (Seoul National University), Prof. Tim Li (University of Hawaii), and Dr. H. Annamalai (University of Hawaii), have been illuminating. I also appreciate the feedback offered by Dr. Yuxing Yang (University of Hawaii).

The author wishes to express his gratitude to Dr. Ryo Mizuta (MRI), Dr. Mio Matsueda (JAMSTEC), Dr. Noriko Ishizaki (MRI), Dr. Osamu Arakawa (MRI), Dr. Yoshiro Matsuo (JAMSTEC), Dr. Yoshiyuki Kajikawa (University of Nagoya), Dr. Kazuyoshi Kikuchi (International Pacific Research Center), Dr. Kazuyo Fukuda (JAMSTEC), Dr. Tadashi Tsuyuki (MRI), Prof. Kevin Walsh (University of Melbourne), and Dr. Sally Lavender (University of Melbourne) for helpful discussions, advises, and supports.

I especially wish to thank the late Dr. Hajime Nakamura for his encouragements when I started to work as a researcher at JMA. Also, I wish to thank Dr. Yousuke Yamazaki, my best friend, for his advises and encouragements.

The author would also like to acknowledge the assistance and support of members of the Kyosei and Kakushin projects, the Numerical Prediction Division of JMA, and Climate Research Department of MRI.

Thanks also go to the Earth Simulator Center for providing computational environments. This study was conducted under the framework of the "Projection of the Change in Future Weather Extremes Using Super-High-Resolution Atmospheric Models" project supported by the KAKUSHIN program of the Ministry of Education, Culture, Sports, Science, and Technology (MEXT) of Japan.

Special thanks to the supports by my parents, Saburo and Yumiko, and my sister, Mayumi.

References

Anthes, R. A., R. W. Corell, G. Holland, J. W. Hurrel, M. C. MacCracken, and K. E. Trenberth, 2006: Hurricanes and global warming -Potential linkages and consequences. *Bull. Amer. Meteor. Soc.*, **87,** 623–628.

Arakawa, A., and W. H. Schubert, 1974: Interaction of a cumulus cloud ensemble with the large-scale environment, Part I. *J. Atmos. Sci.*, **31,** 674–701.

Atkinson, G. D., and C. R. Holiday, 1977: Tropical cyclone minimum sea level pressure/maximum sustained wind relationship for the western North Pacific. *Mon. Wea. Rev.*, **105,** 421–427.

Ballish, B., X. Cao, E. Kalnay, and M. Kanamitsu, 1992: Incremental nonlinear normal-mode initialization. *Mon. Wea. Rev.*, **120,** 1723–1734.

Bell, G. D., and M. Chelliah, 2006: Leading tropical modes associated with interannual and multidecadal fluctuations in North Atlantic hurricane activity. *J. Climate*, **19,** 590–612.

Bender, M. A., R. J. Ross, R. E. Tuleya, and Y. Kurihara, 1993: Improvements in tropical cyclone track and intensity forecasts using the GFDL initialization system. *Mon. Wea. Rev.*, **121,** 2046–2061.

——, T. R. Knutson, R. E. Tuleya, J. J. Sirutis, G. A. Vecchi, S. T. Garner, and I. Held, 2010: Modeled impact of anthropogenic warming on the frequency of intense Atlantic hurricanes. *Science*, **327,** 454–458.

Bengtsson, L., M. Botzet, and M. Esch, 1996: Will greenhouse gas-induced warming over the next 50 years lead to higher frequency and greater intensity of hurricanes? *Tellus*, **48A,** 57–73.

——, K. I. Hodges, M. Esch, N. Keenlyside, L. Kornblueh, J. J. Luo, and T. Yamagata, 2007: How may tropical cyclones change in a warmer climate? *Tellus*, **59A,** 539–561.

Bister, M., and K. A. Emanuel, 1998: Dissipative heating and hurricane intensity. *Meteorol. Atmos. Phys.*, **52,** 233–240.

Blackadar, A. K., 1962: The vertical distribution of wind and turbulent exchange in a neutral atmosphere. *J. Geophys. Res.*, **67,** 3095–3102.

Briegleb, B. P., 1992: Delta-Eddington approximation for solar radiation in the NCAR community climate model. *J. Geophys. Res.*, **97,** 7603–7612.

Broccoli, A. K., and S. Manabe, 1990: Can existing climate models be used to study anthropogenic changes in tropical cyclone climate? *Geophys. Res. Lett.*, **17,** 1917–1920.

Camargo, S. J., and A. H. Sobel, 2005: Western North Pacific tropical cyclone intensity and ENSO. *J. Climate*, **18,** 2996–3006.

——, K. A. Emanuel, and A. H. Sobel, 2007a: Use of a genesis potential index to diagnose ENSO effects on tropical cyclone genesis. *J. Climate*, **20,** 4819–4834.

——, ——, A. G. Barnston, and K. A. Emanuel, 2007b: Tropical cyclone genesis potential index in climate models. *Tellus*, **59A,** 428–443.

——, M. C. Wheeler, and A. H. Sobel, 2009: Diagnosis of the MJO modulation of tropical cyclogenesis using an empirical index. *J. Atmos. Sci.*, **66,** 3061–3074.

Chan, J. C. L., 1985: Tropical cyclone activity in the northwest Pacific in relation to the El Niño/Southern Oscillation phenomenon. *Mon. Wea. Rev.*, **113,** 599–606.

——, 1995: Tropical cyclone activity in the western North Pacific in relation to the stratospheric quasi-biennial oscillation. *Mon. Wea. Rev.*, **123,** 2567–2571.

——, 2000: Tropical cyclone activity over the western North Pacific associated with El Niño and La Nińa events. *J. Climate*, **13,** 2960–2972.

——, 2009: Thermodynamic control on the climate of intense tropical cyclones. *Proc. R. Soc. A.*, **465,** 3011–3022.

——, and K. S. Liu, 2004: Global warming and western North Pacific typhoon activity from an observational perspective. *J. Climate*, **17,** 4590–4602.

Chauvin, F., J. F. Royer, and M. Déqué, 2006: Response of hurricane-type vortices to global warming as simulated by ARPEGE-Climat at high resolution. *Clim. Dyn.*, **27,** 377–399.

Chen, T.-C., S.-P. Weng, N. Yamazaki, and S. Kiehne, 1998: Interannual variation in the tropical cyclone formation over the Western North Pacific. *Mon. Wea. Rev.*, **126,** 1080–1090.

Chia, H. H., and C. F. Ropelewski, 2002: The interannual variability in the genesis location of tropical cyclones in the Northwest Pacific. *J. Climate*, **15,** 2934–2944.

Coakley, J. A., R. D. Cess, and F. B. Yurevich, 1983: The effect of tropospheric aerosols on the earth's radiation budget: A parameterization for climate models. *J. Atmos. Sci.*, **40,** 116–138.

Elsner, J. B., A. B. Kara, and M. A. Owens, 1999: Fluctuations in North Atlantic hurricane frequency. *J. Climate*, **12,** 427–437.

Emanuel, K. A., 1995: Sensitivity of tropical cyclones to surface exchange coefficients and a revised steady-state model incorporating eye dynamics. *J. Atmos. Sci.*, **52,** 3969–3976.

Emanuel, K., 2005: Increasing destructiveness of tropical cyclones over the past 30 years. *Nature*, **436,** 686–688.

Emanuel, K. A., and D. S. Nolan, 2004: Tropical cyclone activity and global climate. in *26th Conf. on Hurricanes and Tropical Meteorology, Miami, FL*, 240–241, Amer. Meteor. Soc.

Emanuel, K., R. Sundararajan, and J. Williams, 2008: Hurricanes and global warming: results from downscaling IPCC AR4 simulations. *Bull. Amer. Meteor. Soc.*, **89,** 347–367.

Freidenreich, S. M., and V. Ramaswamy, 1999: A new multiple-band solar radiative parameterization for general circulation models. *J. Geophys. Res.*, **97,** 31389–31409.

Gill, A. E., 1980: Some simple solutions for heat-induced tropical circulation. *Quart. J. Roy. Meteor. Soc.*, **106,** 447–462.

Goldenberg, S. B., C. W. Landsea, A. M. Mestas-Nuñez, and W. M. Gray, 2001: The recent increase in Atlantic hurricane activity: Causes and implications. *Science*, **293,** 474–479.

Gray, W. M., 1968: Global view of the origin of tropical disturbances and storms. *Mon. Wea. Rev.*, **96,** 669–700.

——, 1979: Hurricanes: Their formation, structure and likely role in the tropical circulation. in Shaw, D. B. ed., *Meteorology over the Tropical Oceans*, Royal Meteorological Society, 155–218.

Gray, W. M., 1984: Atlantic seasonal hurricane frequency. Part I: El Niño and 30-mb quasibiennial oscillation influences. *Mon. Wea. Rev.*, **112,** 1649–1688.

Gualdi, S., E. Scoccimarro, and A. Navarra, 2008: Changes in tropical cyclone activity due to global warming: Results from a high-resolution coupled general circulation model. *J. Climate*, **21,** 5204–5228.

Haarsma, R. J., J. F. B. Mitchell, and C. A. Senior, 1993: Tropical disturbances in a GCM. *Clim. Dyn.*, **8,** 247–257.

Habata, S., K. Umezawa, M. Yokokawa, and S. Kitawaki, 2004: Hardware system of the Earth Simulator. *Parallel Computing*, **30,** 1287–1313.

Hatsushika, H., J. Tsutsui, M. Fiorino, and K. Onogi, 2006: Impact of wind profile retrievals on the analysis of tropical cyclones in the JRA-25 reanalysis. *J. Meteor. Soc. Japan*, **84,** 891–905.

Hirai, M., T. Sakashita, H. Kitagawa, T. Tsuyuki, M. Hosaka, and M. Oh'izumi, 2007: Development and validation of a new land surface model for JMA's operational global model using the CEOP observation dataset. *J. Meteor. Soc. Japan*, **85A,** 1–24.

Ho, C.-J., J.-J. Baik, J.-H. Kim, D.-Y. Gong, and C.-H. Sui, 2004: Interdecadal changes in summertime typhoon tracks. *J. Climate*, **17,** 1767–1776.

Ho, C.-H., H.-S. Kim, J.-H. Jeong, and S.-W. Son, 2009: Influence of stratospheric quasi-biennial oscillation on tropical cyclone tracks in the western North Pacific. *Geophys. Res. Lett.*, **36,** L06702.

Holland, G. J., 1993: Tropical cyclone motion. Global Guide to Tropical Cyclone Forecasting. *World Meteorological Organization Tech. Doc.*, **560,** 337.

——, and P. J. Webster, 2007: Heightened tropical cyclone activity in the North Atlantic: natural variability or climate trend? *Phil. Trans. Roy. Soc.*, **365A,** 2695–2716.

Hoyos, C. D., P. A. Agudelo, P. J. Webster, and J. Acurry, 2006: Deconvolution of the factors contributing to the increase in global hurricane intensity. *Science*, **312,** 94–97.

IPCC, 2007: *Climate Change 2007: The Physical Science Basis. Working Group I Contribution to the Fourth Assessment Report of the Intergovernmental Panel on Climate Change.* Cambridge University Press, United Kingdom and New York, 996pp.

Iwasaki, T., H. Nakano, and M. Sugi, 1987: The performance of a typhoon track prediction model with cumulus parameterization. *J. Meteor. Soc. Japan*, **65,** 555–570.

——, S. Yamada, and K. Tada, 1989: A parameterization scheme of orographic gravity wave drag with two different vertical partitionings, part I: Impacts on medium-range forecasts. *J. Meteor. Soc. Japan*, **67,** 11–27.

JMA, 2001-2005: *JMA Weather Charts*. Monthly CD-ROM.

——, 2002: *Outline of the operational numerical weather prediction at the Japan Meteorological Agency*. 157 pp.

——, 2007: *Outline of the operational numerical weather prediction at the Japan Meteorological Agency*. 194 pp.

Joseph, J. H., W. J. Wiscombe, and J. A. Weinman, 1976: The delta-Eddington approximation for radiative flux transfer. *J. Atmos. Sci.*, **33,** 2452–2459.

Kamahori, H., N. Yamazaki, N. Mannoji, and K. Takahashi, 2006: Variability in intense tropical cyclone days in the Western North Pacific. *SOLA*, **2,** 104–107.

Kamiguchi, K., A. Kitoh, T. Uchiyama, R. Mizuta, and A. Noda, 2006: Changes in precipitation-based extremes indices due to global warming projected by a global 20-km-mesh atmospheric model. *SOLA*, **2,** 064–067.

Katayama, K., H. Yoshimura, and T. Matsumura, 2003: Development of a 20 km mesh global NWP model on the Earth Simulator. *CAS/JSC WGNE Research Activities in Atmospheric and Oceanic Modeling*, **33,** 0311–0312.

——, ——, and ——, 2004: Development of a 20 km mesh global NWP model on the Earth Simulator. *CAS/JSC WGNE Research Activities in Atmospheric and Oceanic Modeling*, **34,** 0311–0312.

Kawai, H., 2003: Impact of a cloud ice fall scheme based on an analytically integrated solution. *CAS/JSC WGNE Research Activities in Atmospheric and Oceanic Modeling*, **33,** 0411–0412.

——, and T. Inoue, 2006: A simple parameterization scheme for subtropical marine stratocumulus. *SOLA*, **2,** 17–20.

Knutson, T. R., and R. E. Tuleya, 1999: Increased hurricane intensities with CO_2-induced warming as simulated using the GFDL hurricane prediction system. *Clim. Dyn.*, **15,** 503–519.

——, and ——, 2004: Impact of CO_2-induced warming on simulated hurricane intensity and precipitation: Sensitivity to the choice of climate model and convective parameterization. *J. Climate*, **17,** 3477–3495.

——, ——, and Y. Kurihara, 1998: Simulated increase of hurricane intensities in a CO_2-warmed climate. *Science*, **279,** 1018–1020.

——, J. J. Sirutis, S. T. Garner, G. A. Vecchi, and I. M. Held, 2008: Simulated reduction in Atlantic hurricane frequency under twenty-first-century warming conditions. *Nat. Geosci.*, **1,** 359–364.

——, J. L. McBride, J. Chan, K. Emanuel, G. Holland, C. Landsea, I. Held, J. P. Kossin, A. K. Srivastava, and M. Sugi, 2010: Tropical cyclone and climate change. *Nat. Geosci.*, **3,** 157–163.

Krishnamurti, T. N., R. Correa-Torres, and N. Dignon, 1998: The impact of current and possibly future sea surface temperature anomalies on the frequency of Atlantic hurricanes. *Tellus*, **50A,** 186–210.

Kurihara, Y., M. A. Bender, and R. J. Ross, 1993: An initialization scheme of hurricane models by vortex specification. *Mon. Wea. Rev.*, **121,** 2030–2045.

Kusunoki, S., J. Yoshimura, H. Yoshimura, A. Noda, K. Oouchi, and R. Mizuta, 2006: Change of Baiu rain band in global warming projection by an atmospheric general circulation model with a 20-km grid size. *J. Meteor. Soc. Japan*, **84,** 581–611.

Lander, M. A., 1994: An exploratory analysis of the relationship between tropical storm formation in the western North Pacific and ENSO. *Mon. Wea. Rev.*, **122,** 636–651.

Landsea, C. W., 2007: Counting Atlantic tropical cyclones back to 1900. *EOS, Trans. Amer. Geophys. Union*, **88(18),** 197–202.

——, W. M. Gray, P. W. Mielke Jr., and K. J. Berry, 1992: Long-term variations of western Sahelian monsoon rainfall and intense U.S. landfalling hurricanes. *J. Climate*, **5,** 1528–1534.

——, R. A. Pielke Jr., and A. M. Mestas-Nuñez, 1999: Atlantic basin hurricanes: indices of climatic changes. *J. Climate*, **5,** 1528–1534.

——, B. A. Harper, K. Hoarau, and J. A. Knaff, 2006: Can we detect trends in extreme tropical cyclones? *Science*, **313,** 452–454.

LaRow, T. E., Y. K. Lim, D. W. Shin, E. P. Chassignet, and S. Cocke, 2008: Atlantic basin seasonal hurricane simulations. *J. Climate*, **21,** 3191–3206.

Levinson, D. H., 2005: State of the climate in 2004. *Bull. Amer. Meteor. Soc.*, **86,** S1–S86.

Madden, R. A., and P. R. Julian, 1972: Description of global-scale circulation cells in the tropics with a 40-50 day period. *J. Atmos. Sci.*, **29,** 1109–1123.

——, and ——, 1994: Observations of the 40-50-day tropical oscillation -A review. *Mon. Wea. Rev.*, **122,** 814–837.

Mann, M. E., and K. A. Emanuel, 2006: Atlantic hurricane trends linked to climate change. *EOS, Trans. Amer. Geophys. Union*, **87(24),** 233–241.

——, G. J. Holland, and P. J. Webster, 2007a: Atlantic tropical cyclones revisited. *EOS, Trans. Amer. Geophys. Union*, **88(36),** 349–350.

——, T. A. Sabbatelli, and U. Neu, 2007b: Evidence for a modest undercount bias in early historical Atlantic tropical cyclone counts. *Geophys. Res. Lett.*, **34,** L22707.

McDonald, R. E., D. G. Bleaken, D. R. Cresswell, V. D. Pope, and C. A. Senior, 2005: Tropical storms: representation and diagnosis in climate models and the impacts of climate change. *Clim. Dyn.*, **25,** 19–36.

Mellor, G. L., and T. Yamada, 1974: A hierarchy of turbulence closure models for planetary boundary layers. *J. Atmos. Sci.*, **31,** 1791–1806.

——, and ——, 1982: A hierarchy of turbulence closure models for planetary boundary layers. *Rev. Geophys.*, **20,** 851–875.

Mizuta, R., K. Oouchi, H. Yoshimura, A. Noda, K. Katayama, S. Yukimoto, M. Hosaka, S. Kusunoki, H. Kawai, and M. Nakagawa, 2006: 20-km-mesh global climate simulations using JMA-GSM model -mean climate states-. *J. Meteor. Soc. Japan*, **84,** 165–185.

——, Y. Adachi, S. Yukimoto, and S. Kusunoki, 2008: Estimation of future distribution of sea surface temperature and sea ice using CMIP3 multi-model ensemble mean. *Tech. Reports of the MRI*, **56,** 28pp.

Moorthi, S., and M. J. Suarez, 1992: Relaxed Arakawa-Schubert. A parameterization of moist convection for general circulation models. *Mon. Wea. Rev.*, **120,** 978–1002.

Murai, S., and S. Yabu, 2005: Introduction of a new radiation scheme to the operational global NWP model at JMA. *CAS/JSC WGNE Research Activities in Atmospheric and Oceanic Modeling*, **35,** 0419–0420.

Murakami, H., and T. Matsumura, 2007: Development of an effective non-linear normal mode initialization method for a high resolution global model. *J. Meteor. Soc. Japan*, **85,** 187–208.

——, and M. Sugi, 2010: Effect of model resolution on tropical cyclone climate projections. *SOLA*, **6,** 073–076.

——, and B. Wang, 2010: Future change of North Atlantic tropical cyclone tracks: Projection by a 20-km-mesh global atmospheric model. *J. Climate*, **23,** 2699–2721.

——, ——, R. Sakai, A. Noda, and S. Kusunoki, 2008: Verification of typhoon forecasts for a 20km-mesh high-resolution global model. *J. Meteor. Soc. Japan*, **86,** 669–698.

——, B. Wang, and A. Kitoh, 2010: Future change of western North Pacific typhoons: Projections by a 20-km-mesh global atmospheric model. *J. Climate*, accepted.

Nakagawa, M., 2003: Development of a cumulus parameterization scheme of the operational global model at JMA. *CAS/JSC WGNE Research Activities in Atmospheric and Oceanic Modeling*, **33,** 0417–0418.

Nguyen, K. C., and K. J. E. Walsh, 2001: Interannual, decadal, and transient greenhouse simulation of tropical cyclone-like vortices in a regional climate model of the South Pacific. *J. Climate*, **14,** 3043–3054.

Ohfuchi, W., H. Nakamura, M. K. Yoshioka, T. Enomoto, K. Takaya, X. Peng, S. Yamane, T. Nishimura, Y. Kurihara, and K. Ninomiya, 2004: 10-km mesh meso-scale resolving simulations of the global atmosphere on the Earth Simulator -preliminary outcomes of AFES (AGCM for the Earth Simulator)-. *J. Earth Simulator*, **1,** 8–34.

Onogi, K., J. Tsutsui, H. Koide, M. Sakamoto, S. Kobayashi, H. Hatsushika, T. Matsumoto, N. Yamazaki, H. Kamahori, K. Takahashi, S. Kadokura, K. Wada, K. Kato, R. Oyama, T. Ose, N. Mannoji, and R. Taira, 2007: The JRA-25 reanalysis. *J. Meteor. Soc. Japan*, **85,** 369–432.

Oouchi, K., J. Yoshimura, H. Yoshimura, R. Mizuta, S. Kusunoki, and A. Noda, 2006: Tropical cyclone climatology in a global-warming climate as simulated in a 20km-mesh global atmospheric model: Frequency and wind intensity analyses. *J. Meteor. Soc. Japan*, **84,** 259–276.

Oowada, H., 2006: Satellite forecasted image. *Meteor. Res. Note*, **212,** 140, (in Japanese).

Palmer, T. N., G. J. Schutts, and R. Swinbank, 1986: Alleviation of a systematic westerly bias in general circulation and numerical weather prediction models through an orographic gravity wave drag parameterization. *Quart. J. Roy. Meteor. Soc.*, **112,** 1001–1039.

Peterson, T. C., D. M. Anderson, S. J. Cohen, M. Cortez-Vzquez, R. J. Murnane, C. Parmesan, D. Phillips, R. S. Pulwarty, and J. M. R. Stone, 2008 in *Weather and Climate Extremes in a Changing Climate*, National Climatic Data Center, [Available online at http://www.climatescience.gov/Library/sap/sap3-3/finalreport/default.htm].

Pielke, R. A., C. Landsea, M. Mayfield, J. Laver, and R. Pasch, 2005: Hurricanes and global warming. *Bull. Amer. Meteor. Soc.*, **86,** 1571–1575.

Randall, D. A., and D. M. Pan, 1993: Implementation of the Arakawa-Schubert cumulus parameterization with a prognostic closure. The representation of cumulus convection in numerical models. *Meteor. Monogr., Amer. Meteor. Soc.*, **46,** 137–144.

Royer, J.-F., F. Chauvin, B. Timbal, P. Araspin, and D. Grimal, 1998: A GCM study of the impact of greenhouse gas increase on the frequency of occurrence of tropical cyclones. *Clim. Change*, **38,** 307–343.

Sakai, R., and M. Yamaguchi, 2005: The WGNE intercomparison of tropical cyclone track forecasts by operational global models. *CAS/JSC WGNE Research Activities in Atmospheric and Oceanic Modeling*, **35,** 0207–0208.

Sato, N., P. J. Sellers, D. A. Randall, E. K. Schneider, J. Shukla, J. L. Kinter III, Y.-T. Hou, and E. Albertazzi, 1989: Effects of implementing the simple biosphere model (SiB) in a general circulation model. *J. Atmos. Sci.*, **46,** 2257–2282.

Schmidlin, T. W., 2006: On evacuation and deaths from Hurricane Katrina. *Bull. Amer. Meteor. Soc.*, **87,** 754–756.

Sellers, P. J., Y. Mintz, Y. C. Sud, and A. Dalcher, 1986: A simple biosphere model (SiB) for use within general circulation models. *J. Atmos. Sci.*, **43,** 505–531.

Shen, B.-W., R. Atlas, O. Reale, S.-J. Lin, J.-D. Chern, J. Chang, C. Henze, and J.-L. Li, 2006: Hurricane forecasts with a global mesoscale-resolving model: Preliminary results with Hurricane Katrina(2005). *Geophys. Res. Lett.*, **33,** L13813.

Shibata, K., and T. Aoki, 1989: An infrared radiative scheme for the numerical models of weather and climate. *J. Geophys. Res.*, **94,** 14923–14943.

——, and A. Uchiyama, 1992: Accuracy of the delta-four-stream approximation in inhomogeneous scattering atmospheres. *J. Meteor. Soc. Japan*, **70,** 1097–1109.

Simmons, A. J., and D. M. Burridge, 1981: An energy and angular-momentum conserving vertical finite-difference scheme and hybrid vertical coordinates. *Mon. Wea. Rev.*, **109,** 758–766.

Smith, R. N. B., 1990: A scheme for predicting layer clouds and their water content in a general circulation model. *Quart. J. Roy. Meteor. Soc.*, **116,** 435–460.

Sommeria, G., and J. W. Deardorff, 1977: Subgrid-scale condensation in models of non-precipitating clouds. *J. Atmos. Sci.*, **34,** 344–355.

Stowasser, M., Y. Wang, and K. Hamilton, 2007: Tropical cyclone changes in the western North Pacific in a global warming scenario. *J. Climate*, **20,** 2378–2396.

Sugi, M., and J. Yoshimura, 2004: A mechanism of tropical precipitation change due to CO2 increase. *J. Climate*, **17,** 238–243.

——, K. Kuma, K. Tada, K. Tamiya, N. Hasegawa, T. Iwasaki, S. Yamada, and T. Kitade, 1990: Description and performance of the JMA operational global spectral model (JMA-GSM88). *Geophys. Mag.*, **43,** 105–130.

——, A. Noda, and N. Sato, 2002: Influence of the global warming on tropical cyclone climatology: An experiment with the JMA global model. *J. Meteor. Soc. Japan*, **80,** 249–272.

——, H. Muarakami, and J. Yoshimura, 2009: A reduction in global tropical cyclone frequency due to global warming. *SOLA*, **5,** 164–167.

Sun, Y., and Y. H. Ding, 2002: Anomalous activities of tropical cyclones over the western North Pacific and related large-scale circulation features during 1998 and 1999. *Acta Meteorol. Sinica*, **60,** 527–537.

Tanaka, T. Y., K. Orito, T. Sekiyama, K. Shibata, M. Chiba, and H. Tanaka, 2003: MASINGAR, a global tropospheric aerosol chemical transport model coupled with MRI/JMA98 GCM: model description. *Pap. Meteor. Geophys.*, **53,** 119–138.

Taylor, K. E., 2001: Summarizing multiple aspects of model performance in a singlediagram. *J. Geophys. Res.*, **106, D7,** 7183–7192.

Tokuno, M., and Y. Ohhashi, 2003: Assimilation of QuikSCAT/SeaWinds ocean surface wind data into the global data assimilation system at JMA. *CAS/JSC WGNE Research Activities in Atmospheric and Oceanic Modeling*, **33,** 0137–0138.

Trenberth, K. E., and D. J. Shea, 2006: Atlantic hurricanes and natural variability in 2005. *Geophys. Res. Lett.*, **33,** L12704.

Tsutsui, J., 2002: Implications of anthropogenic climate change for tropical cyclone activity: A case study with the NCAR CCM2. *J. Meteor. Soc. Japan*, **80,** 45–65.

Uchiyama, T., R. Mizuta, K. Kamiguchi, A. Kitoh, and A. Noda, 2006: Changes in temperature-based extremes indices due to global warming projected by a global 20-km-mesh atmospheric model.

Ueno, M., 1995: A study on the impact of asymmetric components around tropical cyclone center on the accuracy of bogus data and the track forecast. *Meteorol. Atmos. Phys.*, **56,** 125–134.

Unisys, 2010: *Unisys weather hurricane tropical data.* [Available online at http://weather.unisys.com/hurricane/].

Vecchi, G. A., and T. R. Knutson, 2008: On estimates of historical North Atlantic tropical cyclone activity. *J. Climate*, **21,** 3580–3600.

——, and B. J. Soden, 2007a: Effect of remote sea surface temperature change on tropical cyclone potential intensity. *Nature*, **450,** 1066–1070.

——, and B. J. Soden, 2007b: Global warming and the weakening of the tropical circulation. *J. Climate*, **20,** 4316–4340.

——, and B. J. Soden, 2007c: Increased tropical Atlantic wind shear in model projections of global warming. *Geophys. Res. Lett.*, **34,** L08702.

Walsh, K. J. E., K. C. Nguyen, and J. L. McGregor, 2004: Fine-resolution regional climate model simulations of the impact of climate change on tropical cyclones near Australia. *Clim. Dyn.*, **22,** 47–56.

——, M. Fiorino, C. W. WLandsea, and K. L. McInnes, 2007: Objectively determined resolution-dependent threshold criteria for the detection of tropical cyclones in climate models and reanalyses. *J. Climate*, **20,** 2307–2314.

Wang, B., and J. C. L. Chan, 2002: How does ENSO regulate tropical storm activity over the Western North Pacific? *J. Climate*, **15,** 1643–1658.

——, R. Elsberry, Y. Wang, and L. Wu, 1998: Dynamics in tropical cyclone motion: A review. *Chinese J. Atmos. Sci.*, **22,** 535–547.

——, Y. Yang, Q.-H. Ding, H. Murakami, and F. Huang, 2010: Climate control of the global tropical storm days (1965-2008). *Geophys. Res. Lett.*, **37,** LL07704.

Webster, P. J., G. J. Holland, J. A. Curry, and H.-R. Chang, 2005: Changes in tropical cyclone number, duration, and intensity in a warming environment. *Science*, **309,** 1844–1846.

WMO, 1966: Climatic change. WMO/TD 79, World Meteorological Organization.

——, 2005: Typhoon committee operational manual -meteorological component-. WMO/TD 196, World Meteorological Organization.

Wu, L., and B. Wang, 2004: Assessing impact of global warming on tropical cyclone tracks. *J. Climate*, **17,** 1686–1698.

Wu, C.-C., M. A. Bender, and Y. Kurihara, 2000: Typhoon forecast with the GFDL hurricane model: Forecast skill and comparison of predictions using AVN and NOGAPS global analyses. *J. Meteor. Soc. Japan*, **78,** 777–788.

Wu, M. C., W. L. Chang, and W. M. Leung, 2004: Impacts of El Niño-Southern Oscillation events on tropical cyclone land falling activity in the western North Pacific. *J. Climate*, **17,** 1419–1428.

Wu, L., B. Wang, and S. Geng, 2005: Growing typhoon influence on East Asia. *Geophys. Res. Lett.*, **32,** L18703.

Xie, S.-P., C. Deser, G. A. Vecchi, J. Ma, H. Teng, and A. T. Wittenberg, 2010: Global warming pattern formation: sea surface temperature and rainfall. *J. Climate*, **23,** 966–986.

Yokoi, S., and Y. N. Takayabu, 2009: Multi-model projection of global warming impact on tropical cyclone genesis frequency over the western North Pacific. *J. Meteor. Soc. Japan*, **87,** 525–538.

Yoshimura, H., and T. Matsumura, 2003: A semi-Lagrangian scheme conservative in the vertical direction. *CAS/JSC WGNE Research Activities in Atmospheric and Oceanic Modeling*, **33,** 0319–0320.

Yoshimura, J., M. Sugi, and A. Noda, 2006: Influence of greenhouse warming on tropical cyclone frequency. *J. Meteor. Soc. Japan*, **84,** 405–428.

Yumoto, M., and T. Matsuura, 2001: Interdecadal variability of tropical cyclone activity in the western North Pacific. *J. Meteor. Soc. Japan*, **79,** 23–35.

Zhao, M., I. M. Held, S.-J. Lin, and G. A. Vecchi, 2009: Simulations of global hurricane climatology, interannual variability, and response to global warming using a 50-km resolution GCM. *J. Climate*, **22,** 6653–6678.

Zhou, T., R. Yu, J. Zhang, H. Drange, C. Cassou, C. Deser, D. L. R. Hodson, E. Sanchez-Gomez, J. Li, N. Keenlyside, X. Xin, and Y. Okumura, 2009: Why the western Pacific subtropical high has extended westward since the Late 1970s. *J. Climate*, **22,** 2199–2215.